



DOCTORAL THESIS No. 2023:98  
FACULTY OF FOREST SCIENCES

# Estimation of change in forest variables using synthetic aperture radar

IVAN HUUVA

# Estimation of change in forest variables using synthetic aperture radar

**Ivan Huuva**

Faculty of Forest Sciences

Department of Forest Resource Management

Umeå



SWEDISH UNIVERSITY  
OF AGRICULTURAL  
SCIENCES

DOCTORAL THESIS

Umeå 2023

Acta Universitatis Agriculturae Sueciae  
2023:98

ISSN 1652-6880

ISBN (print version) 978-91-8046-248-8

ISBN (electronic version) 978-91-8046-249-5

<https://doi.org/10.54612/a.cab83c7kc3>

© 2023 Ivan Huuva, <https://orcid.org/0000-0002-8664-4872>

Swedish University of Agricultural Sciences, Department of Forest Resource Management,  
Umeå, Sweden

The summary chapter of this thesis is licensed under CC BY NC 4.0, other licenses or  
copyright may apply to illustrations and attached articles.

Print: SLU Grafisk service, Uppsala 2023

# Estimation of change in forest variables using synthetic aperture radar

## Abstract

Large scale mapping of changes in forest variables is needed for both environmental monitoring, planning of climate actions and sustainable forest management. Remote sensing can be used in conjunction with field data to produce wall-to-wall estimates that are practically impossible to produce using traditional field surveys.

Synthetic aperture radar (SAR) can observe the forest independent of sunlight, clouds, snow, or rain, providing reliable high frequency coverage. Its wavelength determines the interaction with the forest, where longer wavelengths interact with larger structures of the trees, and shorter wavelengths interact mainly with the top part of the canopy, meaning that it can be chosen to fit specific applications.

This thesis contains five studies conducted on the Remningstorp test site in southern Sweden. Studies I – III predicted above ground biomass (AGB) change using long wavelength polarimetric P- (in I) and L-band (in I – III) SAR data. The differences between the bands were small in terms of prediction quality, and the HV polarization, just as for AGB state prediction, was the polarization channel most correlated with AGB change. A moisture correction for L-band data was proposed and evaluated, and it was found that certain polarimetric measures were better for predicting AGB change than all of the polarization channels together.

Study IV assessed the detectability of silvicultural treatments in short wavelength TanDEM-X interferometric phase heights. In line with earlier studies, only clear cuts were unambiguously distinguishable. Study V predicted site index and stand age by fitting height development curves to time series of TanDEM-X data. Site index and age were unbiasedly predicted for untreated plots, and the RMSE would likely decrease with longer time series. When stand age was known, SI was predicted with an RMSE comparable to that of the field based measurements.

In conclusion, this thesis underscores SAR data's potential for generalizable methods for estimation of forest variable changes.

Keywords: forest, SAR, biomass, interferometry, polarimetry, change estimation



# Skattning av förändring i skogliga variabler med syntetisk aperturradar

## Sammanfattning

Kartläggning av förändringar i skogliga variabler kan stödja miljöövervakning, rapportering, planering av klimatåtgärder, och ett hållbart skogsbruk. Fjärranalys kan i kombination med fältinventering användas för att skapa frekventa heltäckande skattningar som är praktiskt omöjliga att åstadkomma med endast fältinventering.

Syntetisk aperturradar (SAR) avbildar skogen oberoende av solljus, moln, snöfall, eller regn, och kan därför ge tillförlitliga och frekventa observationer. Eftersom interaktionen med skogen är beroende av våglängden, där långa våglängder främst interagerar med de större strukturerna, som stammar och grova grenar, och korta våglängder främst reflekteras från den övre delen av trädkronorna, kan radarns våglängd väljas för att passa specifika tillämpningar.

Denna avhandling består av fem studier utförda på Remningstorps försöksområde. Studierna I – III predikterade förändringar i biomassa ovan mark från polarimetriska SAR-data i P- och L-band. Studierna konstaterade att skillnaderna mellan banden i termer av prediktionskvalitet är små och att HV-polarisationen är den polarisation som är starkast korrelerad med förändringar i biomassa. En metod för fuktkorrigerad av bakåtspridningen i L-bandsdata presenterades och utvärderades, och det konstaterades att modeller byggda på vissa polarimetriska mått predikterade förändringar i biomassa bättre än de olika polarisationskanalerna tillsammans.

Studie IV utvärderade detekterbarheten hos skogliga åtgärder i interferometriska TanDEM-X-fashöjder. I linje med tidigare studier var endast slutavverkningar otvetydigt urskiljbara. Studie V predikterade ståndortsindex och ålder hos övrehöjdsträd genom att anpassa höjdtvecklingskurvor till tidsserier av TanDEM-X-data. Ståndortsindex och ålder predikterades obiaserat för orörda provytor, och RMSE skulle sannolikt minska med utökade tidsserier. Med känd ålder predikterades SI med ett RMSE i liknande storleksordning som hos fältmätta värden.

Sammanfattningsvis understryker avhandlingen potentialen hos SAR-data för generaliserbara metoder för skattning av förändringar i skogliga variabler.

Till Jenny, Zappa, och Ärvi

# Contents

List of publications .....	9
1. Introduction .....	15
1.1 Why map changes in forest variables? .....	15
1.2 Radar remote sensing .....	16
1.3 Radar principles .....	18
1.3.1 Electromagnetic waves .....	18
1.3.2 Radar cross section .....	21
1.3.3 Radar equation .....	21
1.3.4 Wavelength .....	22
1.4 Synthetic Aperture Radar .....	24
1.4.1 Imaging geometry .....	24
1.5 Polarization .....	27
1.5.1 The scattering matrix, the covariance matrix, and the coherency matrix .....	27
1.5.2 Polarimetric decompositions .....	28
1.6 Interferometry .....	29
1.6.1 Phase measurement in across-track interferometry .....	29
1.6.2 The complex coherence .....	32
1.6.3 Precision of height measurements .....	33
1.7 SAR in forest remote sensing .....	34
1.7.1 Change estimation .....	35
2. Objectives .....	37
3. Materials and methods .....	39
3.1 Materials .....	39
3.1.1 Remningstorp .....	39
3.1.2 Field data .....	40
3.1.3 ALS data .....	41
3.1.4 SAR data .....	41
3.2 Methods .....	42
3.2.1 Studies I – III .....	42



3.2.2	Studies IV and V .....	43
3.2.3	Prediction quality .....	45
4.	Study summaries .....	47
4.1	Study I .....	47
4.2	Study II .....	49
4.3	Study III .....	50
4.4	Study IV .....	51
4.5	Study V .....	52
5.	Conclusions .....	55
6.	Outlook .....	57
	References .....	59
	Popular science summary .....	65
	Populärvetenskaplig sammanfattning .....	67

## List of publications

This thesis is based on the work contained in the following papers, referred to by Roman numerals in the text:

- I. I. Huuva, H. J. Persson, M. J. Soja, J. Wallerman, L. M. H. Ulander, and J. E. S. Fransson (2020). Predictions of Biomass Change in a Hemi-Boreal Forest Based on Multi-Polarization L- and P-Band SAR Backscatter. *Canadian Journal of Remote Sensing*, 46 (6), pp. 661 – 680
- II. I. Huuva, H. J. Persson, J. Wallerman, L. M. H. Ulander, and J. E. S. Fransson (2023). Prediction of Hemi-Boreal Forest Biomass Change Using ALOS-2 PALSAR-2 L-Band SAR Backscatter. In *Proceedings of the 2023 IEEE International Geoscience and Remote Sensing Symposium, Pasadena, CA, USA, 16 – 21 July 2023*, pp. 3326-3329
- III. H. J. Persson and I. Huuva, (2023). Polarizations and Polarimetric Measures in Biomass Change Prediction using ALOS-2 PALSAR-2 data. (manuscript)
- IV. I. Huuva, H. J. Persson, J. Wallerman, and J. E. S. Fransson (2022). Detectability of Silvicultural Treatments in Time Series of Penetration Depth Corrected Tandem-X Phase Heights. In *Proceedings of the 2022 IEEE International Geoscience and Remote Sensing Symposium, Kuala Lumpur, Malaysia, 17 – 22 July 2022*, pp. 5909-5912

V. I. Huuva, J. Wallerman, J. E. S. Fransson, and H. J. Persson  
(2023). Prediction of Site Index and Age Using Time Series of  
TanDEM-X Phase Heights. *Remote Sensing*, 15 (17), 4195

Papers I, II, IV and V are reproduced with the permission of the publishers.

The contributions of Ivan Huuva to the papers included in this thesis were as follows:

- I. Planned the study with the co-authors. Carried out all remote sensing data processing. Carried out reference AGB change modeling and SAR – AGB modeling, formal analysis, and visualization. Wrote the major part of the manuscript.
- II. Planned the study with the co-authors. Carried out all remote sensing data processing, modeling, formal analysis and visualization. Wrote the major part of the manuscript.
- III. Planned the study with the co-author. Carried out preliminary data processing and analysis. Co-authored the manuscript.
- IV. Planned the study with the co-authors. Carried out formal analysis, visualization, and some of the remote sensing data processing. Wrote the major part of the manuscript.
- V. Planned the study with the co-authors. Carried out formal analysis, visualization, and some of the remote sensing data processing. Wrote the major part of the manuscript.



## Related publications

Apart from the appended studies, the author has contributed to the following relevant publications:

I. Huuva et al. (2017). Measurements of Forest Biomass Change Using L- and P-band SAR Backscatter, In Proceedings of the 2017 IEEE International Geoscience and Remote Sensing Symposium, Fort Worth, TX, USA, 23 – 28 July 2017, pp. 5818–5821.

I. Huuva, H. J. Persson, J. Wallerman, and J. E. S. Fransson (2021). Impact of Plot Size and Extended Extraction Regions of Tandem-X Phase Height in Relation to Forest Variables. In Proceedings of the 2021 IEEE International Geoscience and Remote Sensing Symposium, Brussels, Belgium, 11 – 16 July 2021, pp. 6720–6723.

H. J. Persson, R. Mukhopadhyay, I. Huuva, and J. E. S. Fransson (2022). Comparison of Boreal Biomass Estimations Using C- and X-Band PolSAR, In Proceeding of the 2022 IEEE International Geoscience and Remote Sensing Symposium, Kuala Lumpur, Malaysia, 17 – 21 July 2022, pp. 5555–5558.



# 1. Introduction

## 1.1 Why map changes in forest variables?

The focus of this dissertation is on estimating changes in forest variables using Synthetic Aperture Radar (SAR). The use of remote sensing for the task of estimating forest variables, or changes in them, is motivated by the desire for frequently updated wall-to-wall mapping on a scale that makes reliance solely on manual field surveys impractical and prohibitively costly. Before delving into the specifics of *how*, which the thesis provides some suggestions to, I will provide some answers to the question of *why* by describing some of the reasons that the mapping of changes in forest variables is a worthwhile pursuit.

Forests are critical components of the ecosystem, and changes in forests can be indicative of broader environmental trends. Mapping changes allows us to monitor the health of ecosystems, including biodiversity and carbon sequestration. Forests are habitats for diverse plant and animal species. Mapping changes helps identify areas threatened by habitat loss, aiding in conservation planning and protected area management. The biosphere acts as a net carbon sink, and changes in its efficiency in storing carbon need to be better understood (Canadell et al. 2007). Forests constitute a large part of the terrestrial biosphere and their carbon storage is proportional to the biomass they contain. Monitoring changes in forest biomass helps assess their effectiveness in sequestering carbon.

In addition, forests provide essential resources such as timber, non-timber forest products, and water. Mapping changes helps in sustainable resource management, ensuring that these resources are available for future generations (Ernst et al. 2004; Hohner et al. 2019).



Accurate data on forest changes are also essential for policymakers to formulate effective environmental, conservation, and climate change policies, and to monitor the compliance to such policies and international agreements.

In summary, mapping forest changes provides vital information for environmental conservation, climate change mitigation, and sustainable resource management. It supports decision-making at local, national, and global levels to ensure the well-being of forest owners, ecosystems, societies, and the planet. These goals are not always necessarily in harmony, but this is luckily not a problem that this thesis needs to address.

## 1.2 Radar remote sensing

While manual field surveys remain the source of the most reliable form of information about forest variables and changes in them, such inventories are costly and time consuming. Because of this, remote sensing methods, which can be used to estimate forest variables or changes in them over large areas have become widespread. Forest remote sensing generally is the science or practice of relating signatures in data collected using some remote sensor, carried for example by a satellite, an airplane, or an unmanned aerial vehicle (UAV), to physical properties of the remotely probed forest.

Remote sensing not only makes it possible to monitor forests in a wall-to-wall manner, which is practically impossible using manual inventory methods for any large area, but also allow for frequently updated estimates. Assuming that the processing time is negligible in the context, which is reasonable for an established algorithm, the update time is limited by the revisit time of the sensor in question.

Radar signals are distinct in remote sensing applications due to their ability to penetrate the atmosphere under virtually all conditions. Depending on the wavelength, the microwave energy of the signal is able to probe the surface of the earth unhindered by clouds, rain, snow and smoke, i.e. conditions that greatly challenge for example optical sensors, making it impossible for them to image some regions with nearly perpetual cloud cover (Ulaby et al. 1981; Lillesand and Kiefer 2000).

Radar sensors are also active, meaning that they generate the energy used for the measurement, making them able to operate independently of sunlight,

thereby further increasing their coverage advantage over passive optical sensors.

Further, radar reflections have little similarity with the signals measured by optical sensors; a microwave signal can penetrate significantly into a canopy and even reflect from the ground where the canopy would be opaque in the optical spectrum, and a surface that appears rough to optical radiation can be smooth to microwave radiation (Ulaby et al. 1981; Lillesand and Kiefer 2000). The distinct character of the radar measurement provides unique and complementary information about the objects of study.

While widespread aerial photography began after World War I, the first large scale mapping using airborne radar was a survey of the Darien province of Panama in 1967. Due to persistent cloud cover, the whole region had never been fully covered due to near perpetual cloud cover in parts of the region. The success of the survey led to many more similar campaigns (Lillesand and Kiefer 2000).

Radar remote sensing from space began with the launch of Seasat in 1978, followed by the Soviet Cosmos experiments and Shuttle Radar Imaging (SIR) in the 1980s, and broad scale availability started in the early 90s with a number of radar satellite launches, beginning with the launches of Almaz-1, ERS-1 and JERS-1 in 1991 and 1992 (Lillesand and Kiefer 2000).

Since then, a number of missions have launched, and currently there a number of radar satellites continuously providing radar images of the earth in a number of wavelengths and modes. These include the current Sentinel-1 (~6 cm wavelength) and the planned ROSE-L (~24 cm wavelength), from the European Space Agency (ESA), the current ALOS-2 and upcoming ALOS-4 (24 cm wavelength) satellites from the Japan Aerospace Exploration Agency, (JAXA), the TanDEM-X (~3 cm wavelength) mission from the German aerospace center (DLR), the Cosmo-Skymed (~3 cm wavelength) constellation from the Italian Space Agency (ASI), the RADARSAT constellation mission (RCM, ~6 cm wavelength) from the Canadian Space Agency (CSA), the SAOCOM mission (24 cm wavelength) by the Argentinian National Space Activities Commission (CONAE), and the upcoming NISAR (10 cm and 24 cm wavelength) by NASA and the Indian Space Research Organization (ISRO) in collaboration. This list is far from exhaustive, and these and other current and planned SAR missions provide ample opportunities for efficient monitoring of changes in the Earth's forests.

## 1.3 Radar principles

Radars are devices that transmit radio frequency (RF) electromagnetic (EM) signals from an antenna, and measure the distance to objects from the time it takes for radiation to reflect off objects and return to the device. While the general idea was conceived shortly after the discovery of radio waves in the late nineteenth century, the development of radar was greatly accelerated by its usefulness in military surveillance applications during the world wars of the first half of the twentieth century (Sullivan 2004). This chapter will briefly describe the properties of EM waves, before summarizing some important properties of radars in general. After this, some key concepts of SAR, InSAR and PolSAR are reviewed. The last part of the chapter summarizes some previous studies especially relevant to the studies included in this thesis.

### 1.3.1 Electromagnetic waves

EM waves are a propagation of oscillations in the electromagnetic field emanating from accelerating electrical charges, as predicted by Maxwell's equations. Figure 1 shows an electromagnetic wave in free space propagating from left to right. The vectors indicate the instantaneous direction and magnitude of the electromagnetic fields at each point in space. Blue vectors show the electric field  $\mathbf{E}$ , and red vectors the magnetic field  $\mathbf{B}$  (bold variable names indicate vector quantities). The two fields are always orthogonal (perpendicular) to each other and the direction of propagation of the wave. The direction of propagation is given by the vector  $\mathbf{E} \times \mathbf{B}$  where  $\times$  denotes the cross product.

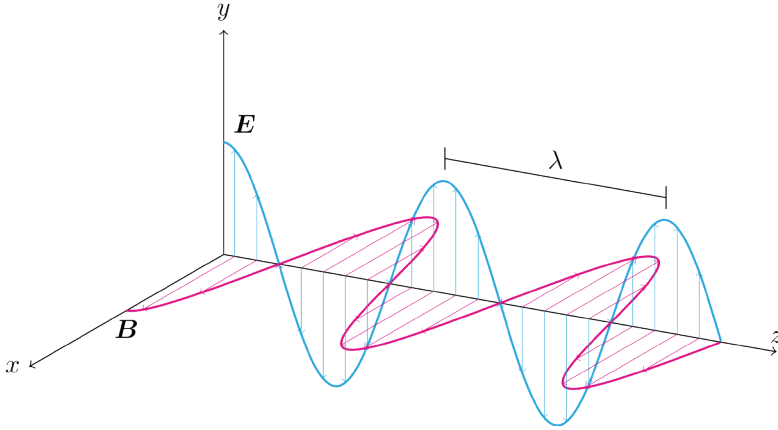


Figure 1. An electromagnetic wave, with the electric field  $\mathbf{E}$  oscillating in the  $y$  direction, and the magnetic field  $\mathbf{B}$  oscillating in the  $x$  direction.

The magnitudes of the two fields are related by  $E = cB$ , where the proportionality constant  $c$  is the wave propagation speed, the speed of light. Note that since the magnitude is a scalar, the font is non bold. As the two fields are fully determined by each other, a simple EM wave is fully described by defining only one of them. A mathematical representation of such a wave, with frequency  $f$ , in three dimensional Cartesian coordinates and time  $t$  is given by

$$\mathbf{E}(z, t) = \mathbf{E}_0 \cos(kz - 2\pi ft), \quad (1)$$

which describes a monochromatic plane wave travelling along the  $z$  direction and oscillating along a line in the transverse  $x - y$  plane defined by the amplitude vector  $\mathbf{E}_0$  (Griffiths 2013). In addition to defining the direction of oscillation,  $\mathbf{E}_0$  defines the amplitude of the oscillation via its magnitude  $E_0$ . The so called wave number,  $k$ , is related to the wavelength,  $\lambda$ , of the wave by

$$k = \frac{2\pi}{\lambda}. \quad (2)$$

The full argument to the cosine function in (1),  $kz - 2\pi ft$ , is called the phase, and is often denoted by  $\phi$ . The wave function is periodic and obtains the same value for  $\phi$  and  $\phi + n2\pi$ , where  $n$  is an integer, and because of this, the phase is ambiguous beyond a range of 0 to  $2\pi$ .

The electric field of the electromagnetic wave can oscillate in any direction in the plane transverse to the propagation direction, but any such oscillation can be represented as a linear combination of two orthogonal component fields in this plane. A common choice of such polarization

components (bases) are the vertically (V) and horizontally (H) linearly polarized waves. When a V and H wave of equal amplitude are *in phase*, i.e. their maxima occur simultaneously, their combination adds up to another linearly polarized state, at  $45^\circ$  to both the H and V directions. If the amplitudes of the two in phase waves differ, the orientation angle in the transverse plane will deviate from  $45^\circ$ , but the polarization will still be linear.

If there is a difference in phase,  $\Delta\phi = \phi_V - \phi_H$ , between the H and V components, the resulting wave will no longer be linear, and the resulting electric field will instead of a line, trace out an ellipse in the transverse plane, or in the case of  $\Delta\phi = \pm\pi/2$ , a circle. Figure 2 illustrates such a combination. In this case, the H polarization field  $\mathbf{E}_H$  lags the V polarization field  $\mathbf{E}_V$  ( $\Delta\phi = -\pi/2$ ). The sign of the phase difference determines the so called *handedness* of the polarization.

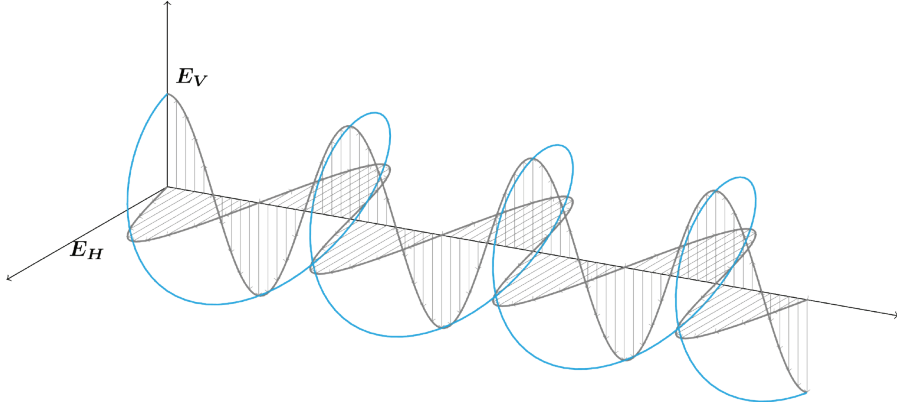


Figure 2. Circularly polarized electromagnetic wave.

The EM-wave carries energy in the direction of propagation. The energy flux density per unit area and unit time is given by the Poynting vector:

$$\mathbf{S} = \frac{1}{\mu_0} (\mathbf{E} \times \mathbf{B}), \quad (3)$$

which is a vector quantity, pointing in the direction of propagation. The average energy over a cycle (or a number of cycles) is given by

$$\langle \mathbf{S} \rangle = \frac{1}{2} \epsilon_0 E^2 \hat{\mathbf{z}}, \quad (4)$$

Where  $\hat{\mathbf{z}}$  is a unit vector in the z direction (Griffiths 2013).

### 1.3.2 Radar cross section

When EM-radiation is transmitted from an antenna, it scatters from objects in the path of its beam. The radiation scattered from an object is in general scattered in all directions, but some of the radiation is scattered back toward the transmitting radar antenna. The power received at the radar from a specific object depends both on the object but also on the distance (and angle, due to the gain pattern of the antenna) to the object, since the power emitted from the radar will be spread out over a larger area with increasing distance from the antenna.

The radar cross-section (RCS) of an object is a measure of how much of this incident energy on an object is scattered in a specific direction, and is defined as

$$\sigma \equiv \lim_{R \rightarrow \infty} 4\pi r^2 \frac{E_s^2}{E_i^2}, \quad (5)$$

where  $r$  is the distance to the object, and  $E_i$  and  $E_s$  are the magnitudes of the incident and scattered fields, respectively. The radar cross-section  $\sigma$  has the dimension of an area. The RCS of a general object can vary considerably with its orientation, and the scattering direction. When the energy is reflected back in the direction of the source, which is (at least approximately) the case in the applications in this thesis, the scattering is referred to as *backscatter*.

### 1.3.3 Radar equation

The signal power received in a radar from scattering off a target with radar cross-section  $\sigma$  at a distance  $r$  is related to the peak transmitted power  $P_t$  by

$$P_r = \frac{P_t G_t G_r \lambda^2 \sigma}{(4\pi)^3 r^4}, \quad (6)$$

where  $G_t$  and  $G_r$  are the transmit- and receive gain of the antenna, respectively (Richards et al. 2010). This received signal usually has a very low amplitude, and a radar system always has a certain background level of interfering signal with random amplitude and phase, referred to as noise. The sources of the noise are many, such as antenna noise from the sun, cosmic radiation, the ground, and thermal noise in receiver circuits. Assuming that the noise in the receiver is dominated by thermal noise, it is uniformly distributed in frequency, and the noise power can be expressed in terms of the receiver bandwidth  $B_r$  and a system noise temperature  $T_s$

$$P_n = k_B T_s B_r, \quad (7)$$

where  $k_B$  is Boltzmann's constant (Richards et al. 2010). So far, the treatment has been ideal in the sense that we have not accounted for any losses in the power transfer processes involved. A system loss term is commonly used to characterize the fraction of power lost due to imperfect power transfers. The total system loss is separated into constituent losses as

$$L_s = L_t L_a L_r L_{sp}, \quad (8)$$

where  $L_t$ ,  $L_a$ ,  $L_r$ , and  $L_{sp}$ , are transmit loss, atmospheric loss, receiver loss, and signal processing loss, respectively. By dividing (6) by (7) and (8), we arrive at an expression for the relative strength of the received signal from a target, when compared to the system noise, and taking into account losses. This quantity is called the signal-to-noise ratio, and is given by (Richards et al. 2010)

$$SNR = \frac{P_t G_t G_r \lambda^2 \sigma}{(4\pi)^3 r^4 k_B T_s B_r L_s}. \quad (9)$$

This expression is the general case assuming one pulse is transmitted. In the case of SAR imaging, the returns from a target are collected by multiple pulses using an average power  $P_{tavg}$  during an aperture time  $t_A$  and summed coherently, which makes the following form more appropriate (Sullivan 2004):

$$SNR = \frac{P_{tavg} G_t G_r \lambda^2 \sigma t_A}{(4\pi)^3 r^4 k_B T_s L_s}. \quad (10)$$

### 1.3.4 Wavelength

Electromagnetic radiation in a wide range of frequencies from the microwave spectrum are used in radar applications. These frequencies can be grouped into bands. Table 1 presents the band designations that this dissertation adheres to. The studies contained in this thesis made use of P-, L- and X-band data.

Table 1. Radar band designations.<sup>1</sup>

Band	Frequency	Wavelength
HF	3 – 30 MHz	10-100 m
VHF	30 – 300 MHz	1-10 m
P	216 – 450 MHz	0.7 – 1.4 m

<sup>1</sup> Designations follow the IEEE standard letter designations for radar-frequency bands, except for P-band, which is however a commonly used designation.

<b>Band</b>	<b>Frequency</b>	<b>Wavelength</b>
UHF	0.3 – 3 GHz	1 – 10 cm
L	1 – 2 GHz	15 – 30 cm
S	2 – 4 GHz	7.5 – 15 cm
C	4 – 8 MHz	3.7 – 7.5 cm
X	8 – 12 GHz	2.5 – 3.7 cm
Ku	12 – 18 GHz	1.7 – 2.5 cm
Ka	18 – 27 GHz	1.1 – 2.5 cm
K	20 – 40 GHz	0.75 – 1.5 cm
V	27 – 40 GHz	0.75 – 1.1 cm
W	75 – 110 GHz	2.7 – 4 mm
mm	110 – 300 GHz	1 – 4 mm

The wavelength of radiation greatly affects its interaction with objects. Objects much smaller than the wavelength will scatter the radiation much more weakly than objects whose dimensions are comparable to the wavelength, or larger. This is the reason that microwaves are able to penetrate clouds and rain much better than the shorter optical wavelengths (Ulaby et al. 1981; Lillesand and Kiefer 2000). The differences within the microwave spectrum are also significant in terms of how different band interact with natural targets such as forests. Because the forest with its ground, tree stems, branches, leaves, and needles is made up of structures ranging from mm to meters in size, different parts of the forest match different radar bands in size, producing different reflections depending on the frequency used. Furthermore, because the radiation interacts weakly with objects that are small compared to its wavelength, longer wavelengths, like the meter sized P-band radiation, penetrate further into the canopy, unhindered by the smaller structures like leaves, needles and thin branches, and can produce reflections from the larger structures below, and from the ground (Ulaby et al. 1981). This ability of long wavelengths to reflect from the larger structures of the trees has proven itself valuable in estimating biomass and stem volume. On the other hand, shorter wavelengths like X-band, around 3 cm, interact mainly with the top part of the canopy, if the canopy is closed, therefore allowing the estimation of forest heights using interferometry.



## 1.4 Synthetic Aperture Radar

### 1.4.1 Imaging geometry

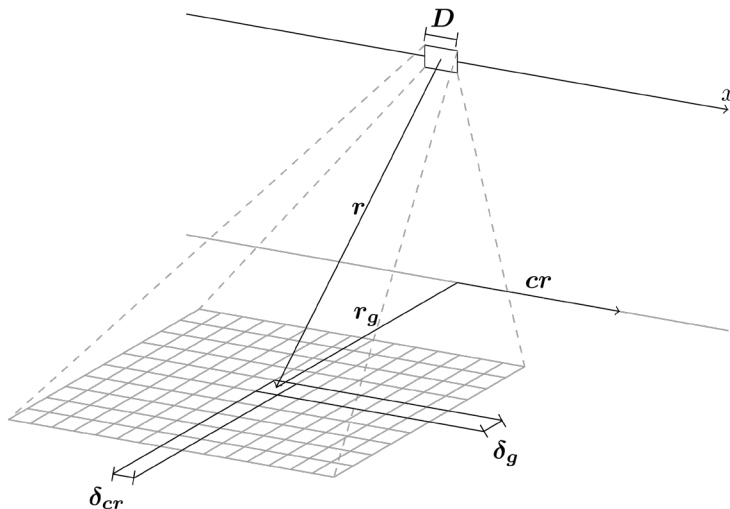


Figure 3. Simplified schematic of SAR acquisition geometry. The moving SAR platform captures a SAR image of the ground in a right-looking configuration.

A simplified schematic of SAR acquisition geometry is shown in Figure 3. The SAR with an antenna of length  $D$  travels to the right in the image and captures a SAR image of the ground in a right-looking configuration. The figure illustrates the acquisition geometry of a SAR. The distance  $r$  is the *slant range* and is the perpendicular (and also shortest) distance of a point to the SAR orbit.  $r_g$  is the perpendicular direction from the ground track (the projection of the sensor path on the ground), and the distance to a point along this direction is called *ground range*. The direction parallel to the flight direction,  $cr$ , is called *cross-range* or *azimuth*.

At each position  $x$  along the track, a pulse  $s_t(t)$  is transmitted which illuminates the area in the footprint of the beam. Some of the energy is backscattered and collected by the radar as  $s_r(x, t)$ . The recorded raw data,  $s_r(x, t)$ , containing amplitude and phase measurements of returned pulses are not in the form of an image, but the raw data from all positions  $x$  when an area was illuminated can be used to form an image of the area. The

position information inherent to the measurements (in addition to precise information about the position and velocity of the SAR platform) is found in the range as probed from the flight time of the pulses, and the Doppler shift caused by the relative speeds between the antenna and different points on the ground. The process of SAR image formation is non-trivial, and many approaches to it have been developed (Richards et al. 2010).

### *Resolution*

Whatever image formation algorithm is used the range resolution of SAR is inversely proportional to the bandwidth of its frequency modulated pulse. The slant range resolution is thus given by

$$\delta_r = \frac{c}{2B}, \quad (11)$$

where  $B$  is the bandwidth of the pulse (Richards et al. 2010). It is worth noting that this denotes the slant range resolution, not ground range. The ground range resolution depends on the slant range resolution, but also on the incidence angle  $\theta$ , and is given by (Sullivan 2004)

$$\delta_g = \frac{\delta_r}{\sin\theta} = \frac{c}{2B\sin\theta}. \quad (12)$$

The cross-range, or azimuth, resolution is given by

$$\delta_{cr} = \frac{\lambda}{2\theta_{int}} \approx \frac{D}{2}, \quad (13)$$

where  $\theta_{int}$  is the integration angle (the span of angles from which a fixed point on the ground is observed), and  $D$  is the along-track length of the antenna (Richards et al. 2010). The last approximation is valid in strip map mode when  $D \gg \lambda$ , and the look direction is orthogonal to the satellite track. The fact that the cross-range resolution is independent of range is a major advantage compared to real aperture radars, attributable to the formation of the synthetic aperture and using the movement of the radar to focus the measurement in the azimuth direction.

### *Different measures of backscatter*

In a radiometrically calibrated SAR image in slant range geometry, the pixel value  $\beta^0$  (pronounced beta-nought) reflects the average RCS per slant range image area  $A_{sr}$  (Ulander 1996),

$$\beta^0 = \frac{\sum \sigma}{A_{sr}}. \quad (14)$$

where the summation is over the values of the radar cross section corresponding to ground area  $A_{sr}$ .  $\beta^0$  however still contains slope induced variations over an image depending on local viewing geometry. If these are corrected for, one obtains the backscattering coefficient  $\sigma^0$  (sigma-nought), defined as the average RCS per unit ground area  $A_g$  (Ulaby et al. 1986),

$$\sigma^0 = \frac{\sum \sigma}{A_g}. \quad (15)$$

The two areas are related via the angle  $\psi$  between the slant range image plane normal, and the ground surface normal by

$$\frac{A_{sr}}{A_g} = \cos \psi, \quad (16)$$

and  $\sigma^0$  is obtained from  $\beta^0$  via (Ulander 1996)

$$\sigma^0 = \beta^0 \cos \psi. \quad (17)$$

When imaging volume scatterers, i.e. when the backscatter is not returned from a surface, but from contributions in a layer of distributed scatterers above ground the scattering coefficient  $\gamma^0$  (gamma-nought), which corrects for different penetration depths dependent on the local incidence angle  $\theta_i$  (Attema and Ulaby 1978),

$$\gamma^0 = \frac{\sigma^0}{\cos \theta_i}. \quad (18)$$

### *Speckle*

The phenomenon of speckle is a nuisance inherent to all coherent imaging. It arises from interference between wave fronts from separate scatterers in a resolution cell. Because of the different range distances to the individual scatterers inside a resolution cell, the scattering contributions add up either constructively or destructively. Speckle is not stochastic noise, as it is determined by the actual positions of scatterers. It is however so sensitive to the exact relative position of the individual scatterers as to appear random from pixel to pixel, and the process makes the phase measurements in a single SAR image appear spatially random, and also adds a noise-like component to the intensity (Richards et al. 2010; Goodman 2015). Speckle can be suppressed by an averaging across multiple pixels or *looks* in both range and azimuth. This so called multilooking process can be performed in either the spatial or the frequency domain. Regardless, the reduction in

speckle comes at the cost of a reduced spatial resolution compared to the original single look image.

## 1.5 Polarization

### 1.5.1 The scattering matrix, the covariance matrix, and the coherency matrix

A fully polarimetric SAR system generally transmits in H and V polarizations and receives the signal using both polarization modes. The measured effect of the backscattering process on the transmitted polarized signals is succinctly presented in a scattering matrix [S], sometimes called the Sinclair matrix. A fully polarimetric SAR measurement is equivalent to the measurement of the Sinclair matrix. When expressed in H and V bases, [S] completely describes the backscattering of these components of an incident wave  $\mathbf{E}^i$  into a scattered wave  $\mathbf{E}^s$  (Cloude 2010):

$$\begin{bmatrix} \mathbf{E}_H^s \\ \mathbf{E}_V^s \end{bmatrix} = \begin{bmatrix} S_{HH} & S_{HV} \\ S_{VH} & S_{VV} \end{bmatrix} \begin{bmatrix} \mathbf{E}_H^i \\ \mathbf{E}_V^i \end{bmatrix}. \quad (19)$$

The elements of the scattering matrix are complex, so that possible phase changes occurring during the scattering are also captured by [S].

Via vectorization of the Sinclair matrix, different scattering power matrices can be constructed. In the following, we will assume reciprocity, i.e.  $S_{HV} = S_{VH}$ , in which case the scattering power matrices are 3 by 3 hermitian matrices. The *covariance matrix* [C], is in its construction connected to system properties of the SAR (Cloude 2010):

$$[C] = \begin{bmatrix} |S_{HH}|^2 & \sqrt{2}S_{HH}S_{HV}^* & S_{HH}S_{VV}^* \\ \sqrt{2}S_{HH}^*S_{HV} & 2|S_{HV}|^2 & \sqrt{2}S_{VV}S_{HV}^* \\ S_{HH}^*S_{VV} & \sqrt{2}S_{VV}^*S_{HV} & |S_{VV}|^2 \end{bmatrix}. \quad (20)$$

Another commonly used scattering power matrix is the coherency matrix [T], which carries the same information, but where the components are more connected to physical scattering processes (Cloude 2010):

$$[T] = \frac{1}{2} \begin{bmatrix} |S_{HH} + S_{VV}|^2 & (S_{HH} + S_{VV})(S_{HH} - S_{VV})^* & 2(S_{HH} + S_{VV})S_{HV}^* \\ (S_{HH} + S_{VV})^*(S_{HH} + S_{VV}) & |S_{HH} - S_{VV}|^2 & 2(S_{HH} - S_{VV})S_{HV}^* \\ 2(S_{HH} + S_{VV})^*S_{HV} & 2(S_{HH} - S_{VV})^*S_{HV} & 4|S_{HV}|^2 \end{bmatrix}. \quad (21)$$

Unlike the Sinclair matrix [S], the covariance matrix [C] and the coherency matrix [T] are suited for the study of partially polarizing targets, i.e. partially incoherent targets. Complex natural targets such as vegetation are not perfectly polarizing and lead to partially polarized received signals and both [C] and [T] allow averaging of signals to make a statistical description of the scattering process.

### 1.5.2 Polarimetric decompositions

Polarimetric decompositions aim to characterize a target by separating different scattering mechanisms and their relative intensity. As the scattering mechanisms depend on the geometry and composition of the target, it can be an effective tool in identifying for example land cover classes or different types of vegetation.

Many types of decompositions have been developed. So called coherent decompositions, such as the Pauli decomposition, express the scattering matrix [S] as a sum of canonical constituent scatterers. Such a decomposition is generally described by

$$[S] = \sum_{i=1}^p c_i [S]_i, \quad (22)$$

where  $p$  is the number of components or scattering types,  $c_i$  are the weights of the components, and  $[S]_i$  are the component scattering matrices. Incoherent approaches are instead generally decompositions of the covariance matrix [C] or the coherency matrix [T]. These decompositions are generally given by

$$\langle [X] \rangle = \sum_{i=1}^p c_i [X]_i, \quad (23)$$

where [X] is either [C] or [T],  $p$  is the number of components,  $c_i$  are the component weights,  $[X]_i$  are the component covariance or coherency

matrices, and the averaging is generally spatial using some fixed window size.

## 1.6 Interferometry

Interference is the diffraction pattern arising from addition of waves from coherent radiation sources, and interferometry refers to the measurement of topography using this diffraction pattern. When applied to SAR, this process is referred to as interferometric SAR, or InSAR. In InSAR, two or more SAR observations of the same location with the same, or very similar sensors, are combined to form interferograms. The sensors involved can be separated in space and/or time by a baseline. Temporal baseline interferometry can reveal height changes in the imaged area. The precision of differential InSAR from multiple time points has led to it being widely used in mapping surface displacements due to earthquakes, glacial movements and land subsidence. Spatial baselines allow for very precise measurements of height differences in the scene, a fact that has been widely utilized for topographic mapping of the Earth, such as the shuttle radar topography mission (SRTM), which produced a global digital elevation model (DEM) using the first space borne single-pass InSAR system (van Zyl 2001). Single-pass (i.e. zero temporal baseline) refers to the fact that both acquisitions are made (approximately) simultaneously as opposed to constructing the interferogram using images from different passes over the same area.

### 1.6.1 Phase measurement in across-track interferometry

As the studies included in this thesis only used single-pass across-track interferometry, the geometry of the phase measurements in this case will be treated more closely here. Figure 4 illustrates the approximate geometry of across-track interferometry. In this exposition it is assumed that the range distances are much larger than the baseline  $b$ , which is true for satellite-based SARs. For example, the TanDEM-X system (used in the papers of this thesis) orbits the Earth at an altitude of around 514 km, while the baseline is on the order of a couple of hundred meters, or less. The acquisitions from the two satellite sensors  $SAR_1$  and  $SAR_2$  are separated by a spatial baseline  $b$ , leading to different range distances to a ground point.

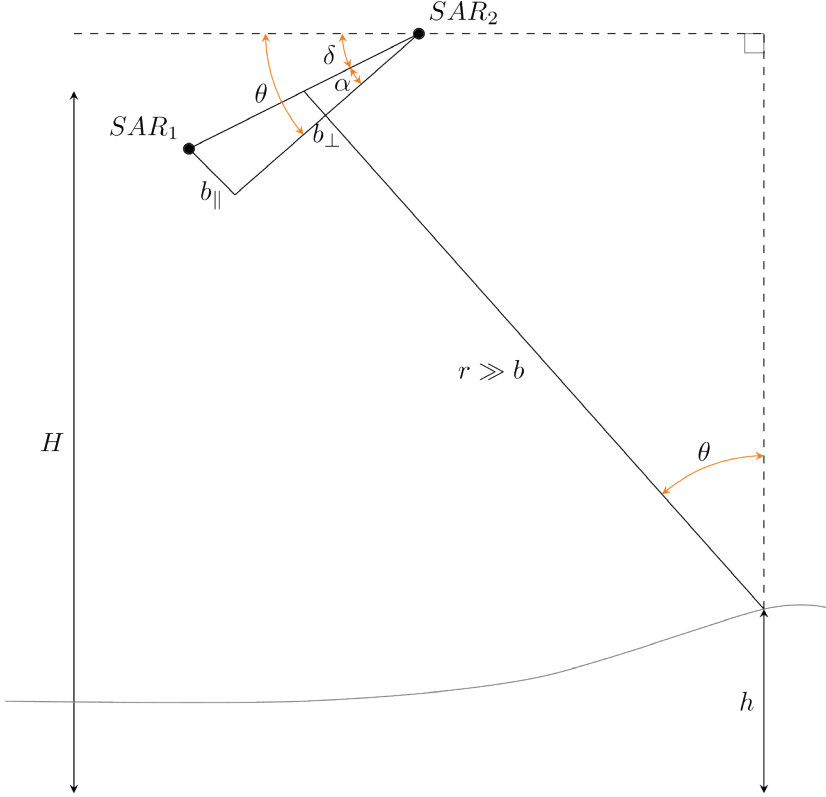


Figure 4. Illustration of single-pass InSAR geometry, using the fact that the range is much greater than the baseline.

The components of the baseline parallel to, and perpendicular to  $r$  are denoted  $b_{\parallel}$  and  $b_{\perp}$ , respectively. The incidence angle (the angle between  $r$  and the vertical direction) is denoted  $\theta$ . Assuming that one of the satellites transmits the signal, and that both satellites receive the scattering from a point on the ground, the phase difference due to the difference in range to the two sensors is given by the wave number  $k$  times the difference in distance, which is equal to the parallel baseline  $b_{\parallel}$ :

$$\phi = kb_{\parallel} = kb \sin \alpha = kb \sin(\theta - \delta) . \quad (24)$$

Differentiating this expression to form the total differential of  $\phi$  gives

$$d\phi = kb \cos(\theta - \delta)d\theta = kb_{\perp}d\theta , \quad (25)$$

if  $\delta$ , the baseline angle, is assumed constant. To get an expression for  $d\theta$ , we can express the ground elevation above some reference height as (see figure 4)

$$h = H - r \cos \theta , \quad (26)$$

where  $H$  is the height to the midpoint of the baseline above the same reference height. Differentiating this expression to form the total differential of  $h$ ,

$$dh = r \sin \theta d\theta - dr \cos \theta , \quad (27)$$

and solving for  $d\theta$  gives

$$d\theta = \frac{dr}{r \tan \theta} + \frac{dh}{r \sin \theta} . \quad (28)$$

Inserting this expression for  $d\theta$  in and rearranging we arrive at

$$d\phi = kb_{\perp} d\theta = \frac{kb_{\perp} dr}{r \tan \theta} + \frac{kb_{\perp} dh}{r \sin \theta} . \quad (29)$$

We can now formulate an expression that describes the dependence of the interferometric phase difference  $\Delta\phi$  observed in the interferogram on changes in range  $\Delta r$  and topography  $\Delta h$ :

$$\Delta\phi = \frac{kb_{\perp} \Delta r}{r \tan \theta} + \frac{kb_{\perp} \Delta h}{r \sin \theta} = \frac{2\pi b_{\perp} \Delta r}{r\lambda \tan \theta} + \frac{2\pi b_{\perp} \Delta h}{r\lambda \sin \theta} \pmod{2\pi} . \quad (30)$$

Here,  $\pmod{2\pi}$  signifies that the measurements of phase differences are measured modulo  $2\pi$ , i.e. that differences larger than  $2\pi$  are mapped back into the  $[0, 2\pi]$  interval. In the beginning of the derivation, we assumed that only one of the sensors transmitted the signal received by both sensors. If we had instead assumed that both sensors transmitted and received their own signal (a monostatic system), there would be a factor 2 in both terms on the right-hand side.

If we let  $\Delta h = 0$  in (30) only the first term contributes to the phase differences. This  $\Delta r$ -term is often referred to as the flat-earth phase. It describes the interferometric phase variation in a flat ( $\Delta h = 0$ ) plane, due to slant range differences to the interferometer. This component of the interferogram is usually removed to reveal the component dependent on local height differences. In interferograms over forested terrain, these height differences are due to both local topography and canopy height. To reveal the interferometric phase due to vegetation, the topographic phase is usually removed using a local digital terrain model (DTM), as was the case in the studies included in this thesis.



Since the measured interferometric phase is in the  $[0, 2\pi]$  interval it needs to be reconstructed to obtain absolute phase differences. This process is called *unwrapping*, and a number of algorithms for doing this have been developed, as the process is not a trivial one, especially in the presence of noise (low coherence), sudden jumps in topography, or shadow, which can make it hard to unambiguously reconstruct the absolute phase differences (Yu et al. 2019). Unwrapping errors can lead to height errors that are multiples of the height difference that, for the specific geometry and sensors corresponds to a  $2\pi$  phase difference. This height difference, given by (31), is referred to as the height of ambiguity since height differences larger than this cannot be unambiguously measured:

$$HoA = \frac{r\lambda\sin\theta}{b_{\perp}}. \quad (31)$$

The height differences that the unwrapped phase corresponds to are obtained by scaling with  $HoA/2\pi$ :

$$\Delta h = \frac{HoA}{2\pi} \Delta\phi. \quad (32)$$

### 1.6.2 The complex coherence

The interferogram is formed from a product of the two images; the signal  $S_1$  from  $SAR_1$ , is multiplied with the complex conjugate of the signal  $S_2$  from  $SAR_2$ ,

$$S_1 S_2^* = A_1 A_2 e^{i(\phi_1 - \phi_2)}. \quad (33)$$

Here, we use the complex representation of the EM-waves, suppress the time dependence of the field, and  $*$  denotes complex conjugation. For the interferogram formation to be meaningful, it requires co-registration of the two images, so that pixels represent scattering from the same location on the ground. The interferometric phase is given by the argument of the interferogram:

$$\phi = \arg(S_1 S_2^*) = \phi_1 - \phi_2. \quad (34)$$

The *complex coherence* is a vector quantity that conveniently carries information about both the interferometric phase, and information about the correlation between the two measurements called the coherence. The complex coherence is defined as

$$\gamma = \frac{\langle S_1 S_2^* \rangle}{\sqrt{\langle S_1 S_1^* \rangle \langle S_2 S_2^* \rangle}}, \quad (35)$$

Where  $\langle \cdot \rangle$  denotes an ensemble average, i.e. an average of multiple measurements of the same process. This is however not possible in practice, so the ensemble average is replaced by a spatial average of values inside a window around the pixel of interest. Just like for the interferogram above, the argument of the complex coherence is the interferometric phase,

$$\phi = \arg(\gamma), \quad (36)$$

but as the magnitude of the complex coherence,  $|\gamma|$ , by its construction is normalized to lie in the interval  $[0,1]$ , it is a generalizable measure of the correlation between the two measurements. This correlation is a measure of the quality of the corresponding phase measurement, as the measurement of interference between uncorrelated signals is not meaningful, and essentially just noise.

The coherence magnitude is typically high for stable targets like bare ground and man-made objects. Over forests, the coherence, even with simultaneous acquisitions is lower due to the complex nature of the volume scattering process in the canopy. In the case of a temporal baseline, such as in repeat-pass interferometry, the decorrelation is much more severe even over short times if there is movement in the canopy due to wind, or changes in moisture that change the dielectric properties of the canopy. Because of this, the retrieval of interferometric information over forests is challenging with other than single pass-interferometry, especially for short wavelengths, where even small movements can cause severe decorrelation.

### 1.6.3 Precision of height measurements

As seen from equation (30), the interferometric phase difference  $\Delta\phi$  corresponding to a height difference  $\Delta h$  is proportional to the perpendicular baseline  $b_{\perp}$ , and inversely proportional to the wavelength of the InSAR system. Since this means that height differences can essentially be magnified by increasing  $b_{\perp}$  and decreasing the wavelength, the precision of height measurements increases with increasing perpendicular baseline and decreasing wavelength. While very high precision can be achieved by tuning InSAR systems like this, there is a drawback to an increased baseline. As the baseline increases, the difference in observation angle to a fixed area on the ground from the two sensors increases, and the coherence between

measurements from the two viewing directions decreases, and finally at the so called *critical baseline*, the coherence becomes zero. While increasing the precision of height measurements, A larger  $b_{\perp}$  also decreases the height of ambiguity which in turn increases the probability of phase ambiguities. A low  $b_{\perp}$ , on the other hand, decreases the SNR of the interferometric phase so that height differences become harder to resolve.

## 1.7 SAR in forest remote sensing

SAR-based methods for forest variable estimation have some distinct advantages to existing methods based on optical measurements, which are limited by cloud cover as well as a low saturation levels for biomass and volume. Spaceborne laser instruments are also limited by cloud cover and atmospheric conditions and only provide data from sample areas. Multiple satellite systems utilizing various wavelength bands and polarizations, including TanDEM-X (X-band ~3 cm, DLR), Sentinel-1 (C-band ~6 cm, ESA), and ALOS-2/PALSAR-2 (L-band ~24 cm, JAXA), can be used to monitor forests. These systems provide frequent reliable measurements, and can complement one another by capturing forest information from different parts of the canopy. Because of this, satellite SAR data have significant potential to emerge as a crucial resource for semi-automated forest resource mapping, potentially revolutionizing forest planning. In this context, time series data will play a pivotal role in tracking changes, such as thinnings, clear-cuts, and growth, forming the foundation for recommending appropriate silvicultural interventions.

The relatively long wavelength of L- and P-band SAR is an advantage because of the signal penetration into the canopy, which facilitates estimation of above-ground biomass (AGB) (Kasischke et al. 1997). Many studies have used both L- and P-band SAR data to predict AGB, or stem volume, in both boreal and hemi-boreal forests (Rignot et al. 1994; Kurvonen et al. 1999; Saatchi and Moghaddam 2000; Rauste 2005; Sandberg et al. 2011; Neumann et al. 2012; Santoro et al. 2015; Schlund and Davidson 2018; Cartus et al. 2019; Santoro et al. 2019). Short wavelength InSAR systems like TanDEM-X on the other hand, have been used extensively to estimate canopy heights and densities, but also biomass (Soja et al. 2015; Chen et al. 2016; Persson and Fransson 2017; Persson et al. 2017) . In Santoro et al. (2019), repeated backscatter observations from TerraSAR-X, Sentinel-1 and ALOS-2

PALSAR-2 were analyzed in boreal and hemi-boreal forest, and used to estimate stem volume. The highest estimation accuracy was obtained at L-band. Stem volume estimates using data at two or three frequencies achieved an accuracy that was superior to using single frequency.

### 1.7.1 Change estimation

L-band data have been used in multiple studies in boreal forest to detect clear-cuts and storm damage (Fransson et al. 2007; Santoro et al. 2012). Other studies have used TanDEM-X data to detect thinnings and clear-cuts (Soja et al. 2017; Soja et al. 2018), but the treatments detected were relatively aggressive, with half or more of the forest volume harvested. These studies were concerned with detection of changes. Studies estimating changes in forest variables using SAR data are not as common, but a few examples are Solberg et al. (2014) who used differences in InSAR height models from SRTM and TanDEM-X to predict AGB change between 2000 and 2011. They reported an RMSE of 65 t/ha, corresponding to 50% of the mean AGB in the area. Askne et al. (2018) estimated AGB growth rates from time series of TanDEM-X data in boreal forest using the Interferometric Water Cloud Model. The maximum growth rate in terms of AGB was 4.0 t/ha/yr with a mean rate of 1.9 t/ha/yr for 27 stands.

Examples of L- or P-band data being used for estimation of changes in forest variables are few, but some exist. In Balzter et al. (2003), L-band images from Seasat and JERS-1, from 1978 and 1997, respectively, were used to estimate height changes, and estimation errors of 3 – 4 m were reported. In Rowland et al. (2008), L-band data from AIRSAR and E-SAR were used to measure changes in forest height and stem volume between 1991 and 2000. Estimation errors for stem volume change varied between 12.5 m<sup>3</sup>/ha and 18 m<sup>3</sup>/ha. For forest height changes, the errors were between 0.2 m and 0.64 m. Sandberg et al. (2014) predicted AGB change from bi-temporal airborne polarimetric P-band SAR data in hemi-boreal forest with an RMSE of 20 t/ha using a backscatter change offset correction based on the HH/VV polarization ratio.

Study I in this thesis took its starting point in the study by Sandberg et al. (2014). The study used P-band data from the BioSAR 2007 and BioSAR 2010 campaigns, but during the campaigns, polarimetric L-band data was also collected over the same area, providing an excellent opportunity for a comparison between L- and P-band for AGB change prediction. Whether the

L-band data would need to be backscatter offset corrected, and whether the HH/VV-based correction would work for the L-band data if needed, was however not known.

Three of the five papers included in this thesis focused on biomass change estimation using fully polarimetric, relatively long wavelength L- and P-band SAR data, while two of the papers used interferometric short wavelength X-band data to detect silvicultural treatments and estimate stand age and site index.

The remainder of this dissertation is structured as follows: In Chapter 2, the objectives of the thesis and the appended papers are listed. Chapter 3 briefly describes the materials and methods used in the studies. Chapter 4 summarizes the included papers, chapter 5 presents conclusions and Chapter 6 gives a brief outlook on future research.

## 2. Objectives

The overall objective of the dissertation was to investigate how SAR can be used for forest change estimation. The specific objectives of the included studies were:

I To develop and evaluate a backscatter offset correction method for L-band SAR data, and to validate an existing correction method for P-band data. In addition, to compare the potential of predicting AGB changes in a hemi-boreal forest using L- and P-band backscatter, assuming that a suitable offset correction method can be applied to both bands.

II To predict biomass change over seven growth seasons between 2015 and 2022 using regression models relating the biomass change to L-band SAR data from the spaceborne ALOS-2 PALSAR-2 sensor, using the HV-VV backscatter ratio developed in study I to correct the backscatter intensity.

III To 1) assess if the use of multiple polarizations could improve the AGB change estimates compared to a single polarization, 2) compare different polarimetric SAR approaches for estimating AGB change, 3) identify if saturation effects can be reduced or overcome by using multiple polarizations, and 4) investigate the impact of forest structure.

IV To assess the detectability of silvicultural treatments in time series of phase heights from TanDEM-X data and to assess the usefulness of applying an InSAR elevation bias correction for the purpose.

V To assess the potential for predicting site index and tree age using time series of TanDEM-X data without the need for phase height calibration using field data. Furthermore, to evaluate the effects of treatments on the predictions.

## 3. Materials and methods

### 3.1 Materials

All studies relied on a combination of field observations, SAR data, and to a varying extent, ALS data. All studies were conducted on the Remningstorp estate, and the chapter starts with a brief description of the site, after which the field data used in the studies are briefly described. After this, the ALS data, and then the SAR data are briefly described. All descriptions here are only intended to give an overview of the studies. The details are described more extensively in the papers.

#### 3.1.1 Remningstorp

Remningstorp is a forest test site situated in southern Sweden (Latitude 58°30'N, Longitude 13°40'E). The estate spans approximately 1,200 hectares and consists primarily of commercially managed hemi-boreal forest. Nearly two-thirds of the forest is situated on till, a mixture of glacial debris, and is characterized by a ground layer of herbs, blueberries (*Vaccinium myrtillus* L.), and narrow-leaf grasses like *Deschampsia flexuosa* (L.) Trin. In older spruce stands the field layer is absent. The main tree species are Norway spruce (*Picea abies* (L.) H. Karst.), Scots pine (*Pinus sylvestris* L.), and various birch species. The remaining forest is located on peatland, dominated by Scots pine. The landscape is mostly flat with gentle slopes and is positioned at elevations ranging from 120 m to 145 m above sea level.



Table 2. Field data sets used in included papers.

<b>Dataset</b>	<b>Year of inventory</b>	<b>Plot area [m<sup>2</sup>]</b>	<b>No. of plots</b>	<b>Used in study</b>
F1	2004-2005	314	763	I
F2	2010	314	208	I
F3	2007	6400	10	I
F4	2010	6400	7	I
F5	2014-2015	314	263	II
F6	2021	314	263	II
F7	2014	5027	48	III
F8	2021	5027	48	III
F9	2011	5027	25	IV
F10	2012-2013	5027	20	IV
F11	2014	5027	27	IV
F12	2014	314	51	V
F13	2021	314	91	V

### 3.1.2 Field data

Several field data sets from Remningstorp were used in the included papers (Table 2). The data sets consisted of 10 m radius circular plots, 40 m radius circular plots, and 80 m × 80 m square plots. The 10 m circular plots were systematically distributed across the estate, while the 40 m circular plots and the square plots were subjectively placed within homogenous stands. The general inventory procedure was similar for all field datasets, although some of the surveys differed in some details. Generally, the species, diameter at breast height (dbh) and geographic position was recorded for all trees with a dbh  $\geq 4$  cm. For a subset of trees, selected with an inclusion probability proportional to the basal area, the height was measured with a hypsometer. In data set F12 and F13, the site index was determined based on the properties of two dominant trees per plot. The height of these trees was measured using a hypsometer, and the age was determined by extracting stem cores and counting growth rings. In addition to field surveys, a forest management plan and silvicultural treatment records were used in the studies to delineate forest stands, and to identify treatments and treatment dates.

### 3.1.3 ALS data

#### *Studies I and II*

ALS acquisitions over Remningstorp were made in 2007 and 2010 using helicopter-mounted TopEye systems (Mk II in 2007, Mk III in 2010). The 2007 scanning had pulse densities of 30 – 40 pulses/m<sup>2</sup>. In 2010, the scanning had an average density of 69 pulses/m<sup>2</sup>. Further details can be found in the BioSAR reports (Hajnsek et al. 2008; Ulander et al. 2011). The generated point clouds were used in study I to create AGB maps over the test site. A digital terrain model (DTMs) from ground classified points of the 2010 ALS data set was used in studies I and II for radiometric terrain correction and geocoding of SAR data.

#### *Studies III – V*

Studies III, IV and V used national terrain models provided by the Swedish National Land Survey, based on ground classified ALS data, for radiometric terrain correction, geocoding, and removal of topographic phase.

### 3.1.4 SAR data

Table 3 summarizes information about the SAR data sets used in the included papers. The studies I – III used P- and L-band data with relatively long wavelengths and polarization-based processing and change estimation algorithms, while the studies IV and V used shorter wavelength X-band data, with algorithms based on interferometry. The L- and P-band data in study I were collected in the airborne campaigns BioSAR 2007 and BioSAR 2010. The remaining studies relied on satellite data, studies II and III on L-band data from the ALOS-2 PALSAR-2 system operated by JAXA, and studies IV and V on X-band single-pass InSAR data from the two-satellite constellation TanDEM-X operated by DLR.

Table 3. SAR data sets used in included studies

System	Acquisition years	Band	Resolution Range × azimuth [m]	No. of Scenes	Study
E-SAR	2007	P	2.1 × 0.9	3	I
E-SAR	2007	L	2.1 × 1.6	3	I
SETHI	2010	P	0.9 × 0.9	2	I
SETHI	2010	L	0.8 × 0.8	2	I

System	Acquisition years	Band	Resolution Range $\times$ azimuth [m]	No. of Scenes	Study
PALSAR-2	2015, 2020, 2021	L	$5.1 \times 4.3$	5	II, III
TanDEM-X	2011-2014	X	$1.2 - 1.8 \times 3.3$	24	IV
TanDEM-X	2013-2018	X	$1.2 - 1.8 \times 3.3$	30	V

## 3.2 Methods

### 3.2.1 Studies I – III

These studies were all concerned with biomass change estimation using relatively long wavelength SAR data. They exploited the correlation between long wavelength microwave backscatter and forest biomass. The SAR data used in all three studies were fully polarimetric, and the studies assessed the benefit of using multiple polarizations in biomass change estimation, compared to using only the cross-polarized channel, and the benefit of using polarimetric measures compared to the polarization channels.

In study I, the SAR data were processed to  $\gamma^0$ , and AGB change was modeled using L- and P-band data separately using multiple linear regression. The explanatory variables were based on the backscatter change in each polarization channel separately, and the modeling and analysis explored the utility of using more than one polarization channel among the explanatory variables. Because of a lack of direct change measurements, ALS based AGB maps for each year were created, and the SAR based AGB change models were trained on the difference between the AGB maps. An existing correction procedure to remove backscatter changes external to biomass was applied to the P-band data, and a new correction was proposed for L-band data. The predictions of L- and P-band models were compared, and the corrections were evaluated using across-pair validation, where model parameters were estimated using data from one image pair, and predictions were made on another, in all possible permutations.

In study II, the methods were the same as in study I, except that direct measurements of change were available, so no proxy data was needed to estimate model parameters for SAR based AGB change models. No P-band data was used in this study, which used L-band ALOS-2 PALSAR-2 data.

Study III also used ALOS-2 PALSAR-2 data for AGB change estimation using multiple linear regression. In this study however, in addition to the polarization channels, the Freeman Durden decomposition components, and the radar vegetation index (RVI) were included as sets of variables. Additionally, AGB state was modeled, on different sets of variables, and the impact of structural forest variables on the sensitivity of polarimetric backscatter to AGB was assessed by inspection of plots.

### 3.2.2 Studies IV and V

Studies IV and V used relatively short wavelengths X-band data to detect silvicultural treatments (study IV), and to estimate forest age and site productivity in terms of SI (study V). Studies I – III leveraged the ability of long wavelengths to penetrate into the canopy and in a sense probe its density, while study IV and especially V, on the contrary utilized on the propensity of short wavelengths to reflect mainly from the top part of the canopy. Both studies used X-band data from the bistatic TanDEM-X satellite constellation. The slightly separated view points of the satellites (on the order of hundreds of meters in these studies) enabled interferometry, and the simultaneous acquisitions (near zero temporal baseline) ensured relatively high coherence even in rapidly fluctuating forest canopies.

In study IV, the influences of silvicultural treatments on TanDEM-X interferometric phase heights were assessed using a time series of TanDEM-X data, and records of silvicultural treatments during the monitored time period. The TanDEM-X data, which were delivered as co-registered image pairs (one image per satellite for each acquisition) in SLC format, were interferometrically processed to obtain phase heights. In the processing, an ALS-based DEM was used to remove the phase due to ground topography, so that the remaining phase heights reflected the vertical vegetation structure.

It is however known that, even at short wavelengths, the radar signal is not reflected only from the top surface of the forest, but penetrates into the canopy due to its airy structure. In interferometry, the returns are however assumed to emanate from a surface, and significant penetration into a volume results in both a reduced coherence and a downward elevation bias of the interferometric phase height compared to the top of the volume. A correction to this bias was proposed in Dall (2007). The derivation models the target, in our case a canopy, as an infinite volume into which the signal penetrates. The penetration depth also affects the measured coherence, which therefore can

be used to estimate the resulting elevation bias. This correction has previously been evaluated in temperate forest (Schlund et al. 2019), and was applied to the phase heights in study IV in order to evaluate both its performance in hemi-boreal forest, and whether it would augment the detectability of silvicultural treatments. The bias correction is given by

$$\Delta h = -\frac{|HoA|}{2\pi} \arctan(\sqrt{|\gamma|^{-2} - 1}), \quad (37)$$

where  $HoA$  is the height of ambiguity and  $\gamma$  is the volume coherence.

In study V which also used time series of interferometric TanDEM-X data, the same elevation bias correction was applied in order to estimate canopy heights. The purpose was to evaluate the feasibility of predicting stand age and site index (SI) using time series of TanDEM-X heights. This was done by fitting established height development curves to top heights estimated from the TanDEM-X acquisitions. Previous studies had done this but only using a few acquisitions, and additionally, some sort of calibration had always been used to model tree heights from InSAR phase heights. These calibrations amounted to modeling either field measured tree heights or ALS heights on InSAR phase heights, but in this study the estimation of tree heights relied solely on the above elevation bias correction and used no calibration using auxiliary data.

The height development curves used to determine SI relate top height (height of dominant trees) to their age, and thus describe the expected top height as a function of age and SI for a certain species. Applying these functions on field measurements of top height and age is generally regarded as the most reliable way to determine SI. In this study, the time series of TanDEM-X based height estimates on 10 m radius circular field plots were fitted to the height development curves.

The top height on a field plot is not an aggregated measure of all the tree heights on it, but rather corresponds to the height of the tallest trees on it. Different metrics based on the bias corrected TanDEM-X phase heights were explored, and it was seen that high height percentiles constructed from all the phase height values covered or intersected by the field plot corresponded well to the field measured top heights at the time of inventory, and the 90<sup>th</sup> percentile was chosen as the TanDEM-X based top height measurement.

The prediction of SI and age was based on using non-linear least squares regression to fit the theoretical height development curves to the TanDEM-X top heights for each field plot. As the uncertainty of phase measurements

increases with  $HoA$ , each observation was weighted with  $HoA^{-1}$ . Two different cases were explored, one where both age and SI were left as regression parameters to be estimated, and one where field measured age was used, and only SI was estimated.

### 3.2.3 Prediction quality

#### *Bias estimation*

In the included studies, the systematic prediction error for a sample of  $N$  predictions was generally estimated in the included papers using

$$bias = \frac{\sum_{i=1}^N (\hat{y}_i - y_i)}{N}, \quad (38)$$

where  $\hat{y}_i$  is the  $i$ th prediction value and  $y_i$  is the corresponding observed value.

#### *Root Mean Square Error*

Further, the quality of a sample of  $N$  predictions was generally estimated using the root mean square error:

$$RMSE = \sqrt{\frac{\sum_{i=1}^N (\hat{y}_i - y_i)^2}{N}}. \quad (39)$$

The RMSE is essentially the square root of the sample mean squared error (MSE), and it contains contributions from both the variance and the bias of the predictions (Wackerly et al. 2014; Persson and Ståhl 2020). It is nevertheless a convenient and widely used metric for comparing the predictions from different models.

#### *Cross-validation*

If the observation  $y_i$  in equations (38) and (39) is included in estimating the parameters of the model that maps  $y_i$  to  $\hat{y}_i$ , both quality metrics will be underestimated and thus optimistically biased if used to quantify the uncertainty of new predictions. In fact, when the model is obtained via least squares regression, and includes an intercept term, the bias according to (38) will be zero by definition for the sample used to estimate the model parameters.

When the goal of a model is prediction, one wants to estimate the generalizability of the model, i.e., the performance of the model when applied to data independent of the training sample. Methods of estimating

this out-of-sample performance are collectively called cross-validation. The cross-validation method most used in the included papers is leave-one-out cross-validation (LOOCV). It consists of leaving out one observation in a sample when estimating model parameters, predicting on the left-out observation, iterating the procedure until each observation is left out once. Alternatively, any number of observations  $p$  can be left out each time, and the process iterated over all ways of leaving  $p$  observations out. In this general formulation, the procedure is called leave- $p$ -out cross-validation.

A number of variations on cross-validation exist, but regardless of the method of producing the predictions, their aggregate statistics are used to characterize the out-of-sample performance of the model. Specifically, the predictions can be used in equations (38) and (39) to calculate cross-validated estimates of RMSE and bias.

Cross-validation was used in the included studies to ensure that prediction biases and RMSEs were not underestimated. In some cases, quantities with the same mathematical form as RMSE were referred to instead as RMSD (root mean square deviation) to emphasize the fact that the observed values compared to in these cases were not based on field values of the response variable, but modeled from for example ALS data, as in study I.

## 4. Study summaries

### 4.1 Study I

In this study, we assessed the potential of estimating AGB change from fully polarimetric L- and P-band SAR backscatter, separately. The study did not investigate the bands in combination, but compared the prediction results of the two bands. The SAR data at both bands were collected by airborne systems in 2007 and 2010 over Remningstorp, and the intention was to model AGB change from the change in backscatter using multiple linear regression on predictor variables based on all polarizations.

It was however known that the level of backscatter is strongly correlated with the moisture content in both soil and vegetation, and in Sandberg et al. (2014), a backscatter offset correction was proposed for P-band data. The correction is based on the HH/VV polarization ratio, and mitigated backscatter changes in forest due to moisture differences in pairs of P-band SAR images. The scenes from 2007 were collected on dates with large differences in moisture. Altogether six bi-temporal pairs of SAR images per band were constructed, and if uncorrected for, the changes in backscatter pertaining to moisture differences between the acquisition in 2007 and 2010 would likely obfuscate the changes in backscatter related to differences in AGB between the dates.

The correction had previously only been applied to P-band data, and during the study we quickly found that it did not perform as well for L-band. The rationale for using a polarization ratio in for the correction in Sandberg et al. (2014) was that the two polarizations would be affected in the same way by moisture differences for areas with no change in AGB. Because of this, it



was hypothesized that there would be a very small change in the ratio, and that areas with nearly constant AGB could thus be identified using the ratio.

The failure of the correction led us to investigate other polarization ratios for L-band, and we empirically found that the HV/VV ratio exhibited traits similar to those of the HH/VV ratio for P-band data, namely, some correlation with AGB change, but very small differences in backscatter for areas with no change in AGB, regardless of differences in moisture between dates. This prompted us to modify the correction method for L-band data to use the HV/VV-ratio instead.

Ideally, we would have modeled AGB changes on backscatter changes using repeated measurements of field plots, thereby having direct measurements of AGB change as the response variable (Balzter et al. 2003; Fuller et al. 2003; McRoberts et al. 2015). However, very few plot locations were shared between the two large field surveys of 10 m radius plots that were available for the purpose (F1 and F2 in Table 2). This prompted an indirect approach where AGB was first modeled on ALS metrics from 2007 and 2010, and AGB maps over the whole study area were then created for 2007 and 2010. The pixel level difference between these maps was then used as the AGB change response variable when modeling AGB change on backscatter change.

After model selection, the model predictions were evaluated on ten  $80\text{ m} \times 80\text{ m}$  field plots, which were surveyed in both 2007 and 2010 (unless clear-cut between surveys, in which case the reference AGB was set to zero in 2010).

Because the backscatter offsets (unrelated to AGB differences) are different in different image pairs, models with parameters estimated from one pair of images are expected to perform worse when applied to another image pair. Therefore, the correction methods were evaluated by comparing predictions made in-pair and across pairs. In-pair prediction refers to the case when model parameter estimation and prediction was done using SAR data from the same image pair, while across pair predictions on the contrary refers to when model parameters are fit data from one pair of images, and the predictions are made on data from another image pair.

The correction, based on the HV/VV backscatter ratio, facilitated predictions across image pairs almost identical to in-pair predictions. For P-band, previous positive results using an offset correction based on the HH/VV ratio were validated. The best L-band model achieved an RMSE of

21 t/ha, and the best P-band model achieved an RMSE of 19 t/ha. The RMSEs were similar to those of the LiDAR-based biomass change of 18 t/ha.

## 4.2 Study II

In study II, the HV/VV-ratio based backscatter offset correction, developed in study I using L-band data from airborne experimental systems, was applied to six bi-temporal pairs of fully polarimetric L-band data from the PALSAR-2 sensor carried by the ALOS-2 satellite.

In this study, field data with direct measurements of AGB change were available in the form of 263 circular field plots with 10 m radius surveyed before, and resurveyed after, the acquisitions in the SAR image pairs. The candidate models relating AGB change to backscatter change were the same as in study I, with the difference that field measured AGB change, instead of AGB change modeled on ALS data, served as the response variable.

The obtained in-pair and across-pair AGB change predictions were almost identical in prediction performance as in study I, but it was not clear that this could be attributed to the HV/VV-based offset correction. Since the uncorrected pairs showed no clear general offsets in backscatter, there may not have been much need for correction. Much clearer offsets were observed over the same study area in Sandberg et al. (2014) and study I for both airborne L- and P-band data. The lack of clear offsets between the scenes is possibly due to similar weather and moisture conditions at the acquisition dates.

The RMSEs and biases achieved in this study were significantly larger than those reported for L-band models based on airborne data in study I, but this is not only due to differences in quality between satellite and airborne SAR, but also due to much smaller evaluation areas. In study I, 80 m × 80 m plots, about 20 times larger than the 10 m radius plots in this study were used. To facilitate more conclusive comparisons, additional acquisition dates should be included if possible, and larger evaluation plots could decrease the variance in predictions.

### 4.3 Study III

While studies I and II assessed the potential of using all polarization channels in L-band SAR data to predict biomass change, the predictors used were based on single channels. In study III, two of the fully polarimetric PALSAR-2 images used in study II were used to predict AGB change, but this time, in addition to modeling AGB change on the co- and cross polarized channels, models based on different polarimetric measures were also investigated.

Earlier studies have used a number of polarimetric measures for AGB estimation, estimation of other forest variables, and classification of forest type, but papers relating AGB change to such measures have so far been very few.

The objective was to assess, in boreal forest, if the use of multiple polarizations would improve AGB change estimates and/or reduce saturation effects, to compare different polarimetric approaches to predicting AGB change, and to evaluate the impact of forest structure on the sensitivity of L-band polarimetric backscatter to AGB and AGB change.

This paper specifically modeled AGB change between 2015 and 2021 on 1) the cross-polarized channels, 2) the co- and cross-polarized channels, 3) a Freeman-Durden (FD) polarimetric decomposition (Freeman and Durden 1993; Freeman and Durden 1998) and 4) the polarimetric radar vegetation index (RVI) (Kim and van Zyl 2000).

As the variability in predictions was very high in study II, which used 10 m radius field plots in both modeling and evaluation, it was decided to use a smaller set of 40 m radius plots instead (F7 and F8 in Table 2).

There was a slight improvement in AGB change predictions from model 1), based on only the cross-polarized channels, to model 2) using all channels (84.9 tons/ha to 79.4 tons/ha). The predictions improved further when using FD-decomposition (69.7 tons/ha) and the RVI-based model (50.4 tons/ha).

Comparing models based on the same sets of variables as 1 – 4, but for estimating AGB state in 2014, it was seen that the improvement from 1 to 2 was much greater than in the change estimation, and that the differences between 3 and 4 were small. An analysis of structural field variables showed that the sensitivity to AGB was reduced for high values of forest height, basal area, and stem density, but that the sensitivity to AGB change of the best model was unaffected by these variables.

## 4.4 Study IV

This paper assessed the influence of silvicultural treatments on interferometric phase heights obtained from TanDEM-X data. Additionally, a canopy penetration depth correction presented in Dall (2007) and successfully evaluated in temperate forest in Schlund et al. (2019) was applied to the interferometric phase heights.

Thirty-four circular field plots with a 40 m radius (field data sets F9, F10 and F11 in Table 2) were divided into 25 untreated, 5 thinned and 4 clear-cut plots according to silvicultural treatments recorded in a forest management plan for the estate.

A time series of 24 TanDEM-X scenes acquired in bistatic configuration from 9 August 2011 to 4 June 2014 were used. The scenes were collected in strip map mode, and in VV polarization. The scenes were processed to obtain phase heights at a ground resolution of 10 m × 10 m. In an effort to estimate canopy heights the penetration depth correction was then applied to each pixel.

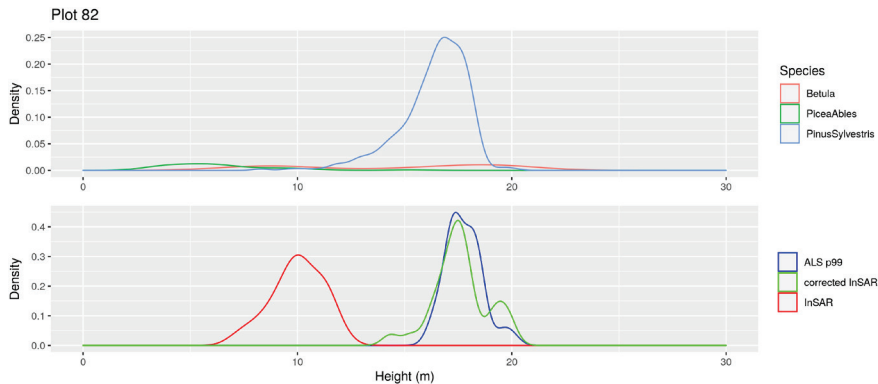


Figure 5 A comparison of estimated height distributions from field measurements (top panel), ALS percentile 99 (blue, bottom panel), TanDEM-X phase heights (red, bottom panel), and penetration depth corrected phase heights (green, bottom panel). ALS and InSAR values are based on pixel values over the field plot. All data are smoothed using kernel density estimates.

To quantify the effect of treatments on phase heights, the mean phase height on each plot was extracted for each date, and the difference in overall mean value of the mean phase heights before and after each treatment was calculated. The calculations were made with and without penetration depth correction, and the results were compared.

The average height decrease resulting from a thinning was on the order of a meter, while clear-cuts resulted in much greater decreases (15 m without correction, 18 m with correction). While there was a mean height decrease for the thinned plots, they were not individually distinguishable from untreated plots in this study.

However, it was seen that the height distribution of penetration depth corrected TanDEM-X phase heights more closely resembled both the distribution of field measured tree heights and ALS percentile 99 (p99) on the test site, than uncorrected phase heights. A comparison of the height distributions from the different data sources for a field plot is shown in Figure 5. The correction had previously been applied to temperate forest with good results, but the results found during study IV indicated the potential of using the procedure to capture top height using TanDEM-X data without the need of local and/or momentary calibration via field and/or ALS data. This result gave us the motivation for study V, in which we would apply the correction in an effort to estimate top height without calibration.

## 4.5 Study V

Study V predicted stand age and site index from time series of bistatic TanDEM-X phase heights. To our knowledge, this had previously been attempted in two studies (Persson and Fransson 2015; Persson and Fransson 2016). In both studies, the time series were however quite short, comprised of four dates spanning a total of three years. Additionally, to estimate canopy heights, TanDEM-X phase heights were calibrated using either field data or ALS data. This study used a much larger time series of 30 TanDEM-X scenes acquired from 2011 to 2018, and instead of relying on auxiliary data for height calibration, the model-based penetration depth correction by Dall (2007), also used in study IV (equation (37)), was applied. Additionally, the influence of silvicultural treatments on prediction quality was investigated by separating the analysis by treatment type using forest management records.

The variables were predicted on 91 field plots with a 10 m radius for which field measurements of SI and age were available from a survey in 2021. For each date, the 90<sup>th</sup> percentile of penetration depth corrected TanDEM-X phase heights on a plot was used as a TanDEM-X based top height.

The SI and age for each field plot was predicted by fitting the time series of these TanDEM-X based top heights for each plot to established height development curves. The fitting was done using weighted non-linear least squares procedure, and each observation was weighted by the reciprocal of HoA, to account for the baseline-related phase height uncertainty. Two cases were assessed: case (a), in which both age and SI were left as parameters to be estimated in the fit, and case (b) in which the age was assumed known, i.e. supplied from field data, and only SI was left as a parameter to be estimated from the time series of TanDEM-X based top heights.

For untreated plots in case (a), the RMSE of predicted SI and age were 6.9 m and 38 years, respectively. In case (b) the RMSE of predicted SI was 4.0 m. No significant bias was observed in either case for untreated plots, nor for treated plots in case (b), while in case (a) the underestimation of SI and overestimation of age increased with the intensity of treatment (in terms of expected biomass reduction).



## 5. Conclusions

The main aim of this thesis has been to develop methods for the estimation of changes in forest variables using SAR data. The use of data from both the relatively long wavelength P- and L-bands, and the short wavelength X-band in the different studies highlight the differences of the bands in their interaction with the forest.

In studies I – III, the relationship between long wavelength backscatter and AGB was exploited to predict changes in AGB between two time points. In study I, fully polarimetric airborne P- and L-band data were compared in their ability to predict AGB change in a hemi-boreal forest, and the differences were found to be small. As is the consensus for AGB prediction, the HV-channel was the most important also for AGB change prediction, for both P- and L-band. A correction for L-band data based on the HV/VV-ratio was developed and found to be effective.

Study II evaluated this correction on satellite based data using fully polarimetric L-band ALOS-2 PALSAR-2 data, but the evaluation did not show the same usefulness as in study I, because no clear differences in backscatter were observed for plots with constant AGB. This is possibly due to similar conditions during the acquisitions, or more consistent calibration for the set of images than in study I.

In study III, also using fully polarimetric ALOS-2 PALSAR-2 data, it was found that that the polarimetric measures, and especially the RVI were able to capture particularly the largest AGB changes more accurately than the polarization channel based models. The analysis of structural forest variables found that high values of basal area weighted mean height, basal area, and stem density were all correlated with a reduction in sensitivity of polarimetric backscatter to AGB.



In studies IV and V, it was instead the tendency of short wavelength X-band SAR to reflect from the top part of the canopy that was exploited. Both studies used interferometric TanDEM-X data to estimate tree heights via a model based correction to phase heights.

In study IV, in line with earlier studies, clear-cuts were found to be clearly distinguishable from a decrease in mean TanDEM-X phase height after the treatment. Thinnings showed a decrease in phase height, but were not individually distinguishable, whether penetration depth correction was applied to the phase heights or not.

Study V presented and assessed a method of predicting SI and age using only time series of TanDEM-X data and a DTM. It was shown that SI and age could be unbiasedly predicted for untreated plots, and the RMSE of the predictions was likely to decrease with the length and temporal resolution of the available time series. When the stand age was known, the SI was predicted with an RMSE comparable to that of field-based measurements. The results for treated plots showed that the RMSE and bias of predictions increase with the intensity of silvicultural treatments.

In conclusion, this thesis underscores the potential of SAR data to be used in generalizable methods for the estimation of changes in forest variables.

## 6. Outlook

The HV/VV-based backscatter offset correction worked well for the L-band data introduced in study I (applied to airborne data), and study II (evaluated for satellite data). Yet, more studies are needed to see if this generalizes to other data sets and regions. Provided that it does, and that present and future L-band missions including ALOS-2, ALOS-4, NISAR, ROSE-L, and SAOCOM operate in modes that offer simultaneous HV and VV channels, the findings suggest a potential for large-area mapping of forest biomass change in boreal and hemi-boreal forests despite varying environmental conditions and calibration uncertainties.

In study III, it was found that models using polarimetric measures, especially the RVI, produced much better AGB change predictions than models based on the polarization channels. The difference was most pronounced for predicting large changes, i.e., clear cuts. Polarimetric measures should be further investigated for AGB change prediction in boreal forests, using high quality SAR- and field data to support the analysis.

Overall, in studies I – III the variation of predictions was still quite high, especially compared to the levels of growth that could be expected in the time periods covered. This makes it challenging to predict growth accurately, other than at very large scales. Models should perhaps be developed separately for forest growth and loss.

In study IV the detectability of silvicultural treatments from TanDEM-X data could be further quantified by investigating the statistical significance of a measured height discontinuity, given a sufficient amount of TanDEM-X measurements both before and after a treatment.

The results in study V demonstrate viability for large-scale wall-to-wall mapping of SI using time series of TanDEM-X data without the need for

ancillary data for height calibration. Further studies should investigate the use of multiple polarizations and both orbit directions to increase the length and temporal density of useful time series in an effort to further increase the obtained prediction quality.

## References

- Askne JIH, Persson HJ, Ulander LMH. 2018. Biomass Growth from Multi-Temporal TanDEM-X Interferometric Synthetic Aperture Radar Observations of a Boreal Forest Site. *Remote Sensing*. 10(4):603. <https://doi.org/10.3390/rs10040603>
- Attema EPW, Ulaby FT. 1978. Vegetation modeled as a water cloud. *Radio Science*. 13(2):357–364. <https://doi.org/10.1029/RS013i002p00357>
- Balzter H, Skinner L, Luckman A, Brooke R. 2003. Estimation of tree growth in a conifer plantation over 19 years from multi-satellite L-band SAR. *Remote Sensing of Environment*. 84(2):184–191. [https://doi.org/10.1016/S0034-4257\(02\)00106-2](https://doi.org/10.1016/S0034-4257(02)00106-2)
- Canadell JG, Le Quéré C, Raupach MR, Field CB, Buitenhuis ET, Ciais P, Conway TJ, Gillett NP, Houghton RA, Marland G. 2007. Contributions to accelerating atmospheric CO<sub>2</sub> growth from economic activity, carbon intensity, and efficiency of natural sinks. *Proceedings of the National Academy of Sciences*. 104(47):18866–18870. <https://doi.org/10.1073/pnas.0702737104>
- Cartus O, Santoro M, Wegmüller U, Rommen B. 2019. Benchmarking the Retrieval of Biomass in Boreal Forests Using P-Band SAR Backscatter with Multi-Temporal C- and L-Band Observations. *Remote Sensing*. 11(14):1695. <https://doi.org/10.3390/rs11141695>
- Chen H, Cloude SR, Goodenough DG. 2016. Forest Canopy Height Estimation Using Tandem-X Coherence Data. *IEEE Journal of Selected Topics in Applied Earth Observations and Remote Sensing*. 9(7):3177–3188. <https://doi.org/10.1109/JSTARS.2016.2582722>
- Cloude S. 2010. *Polarisation: applications in remote sensing*. 1st ed. Oxford ; New York: Oxford University Press.
- Dall J. 2007. InSAR Elevation Bias Caused by Penetration into Uniform Volumes. *IEEE Transactions on Geoscience and Remote Sensing*. 45(7):2319–2324. <https://doi.org/10.1109/TGRS.2007.896613>

Ernst C, Gullick R, Nixon K. 2004. Conserving Forests to Protect Water. *Opflow*. 30(5):1–7. <https://doi.org/10.1002/j.1551-8701.2004.tb01752.x>

Fransson JES, Magnusson M, Olsson H, Eriksson LEB, Sandberg G, Smith-Jonforsen G, Ulander LMH. 2007. Detection of forest changes using ALOS PALSAR satellite images. In: 2007 IEEE International Geoscience and Remote Sensing Symposium. Barcelona, Spain; p. 2330–2333. <https://doi.org/10.1109/IGARSS.2007.4423308>

Freeman A, Durden SL. 1993. Three-component scattering model to describe polarimetric SAR data. In: *Proceedings of SPIE*. Vol. 1748. San Diego, CA, USA; p. 213–224. <https://doi.org/10.1117/12.140618>

Freeman A, Durden SL. 1998. A three-component scattering model for polarimetric SAR data. *IEEE Transactions on Geoscience and Remote Sensing*. 36(3):963–973. <https://doi.org/10.1109/36.673687>

Fuller RM, Smith GM, Devereux BJ. 2003. The characterisation and measurement of land cover change through remote sensing: problems in operational applications? *International Journal of Applied Earth Observation and Geoinformation*. 4(3):243–253. [https://doi.org/10.1016/S0303-2434\(03\)00004-7](https://doi.org/10.1016/S0303-2434(03)00004-7)

Goodman JW. 2015. *Statistical optics*. Second edition. Hoboken, New Jersey: Wiley.

Griffiths DJ. 2013. *Introduction to electrodynamics*. 4. ed., international ed. Boston: Pearson.

Hajnsek I, Scheiber R, Ulander LMH, Gustavsson A, Sandberg G, Tebaldini S, Guarnieri AM, Rocca F, Bombardini F, Pardini M. 2008. *BioSAR 2007, Technical Assistance for the Development of Airborne SAR and Geophysical Measurements during the BioSAR 2007 Experiment: Final Report without Synthesis*. [place unknown]: European Space Agency.

Hohner AK, Rhoades CC, Wilkerson P, Rosario-Ortiz FL. 2019. Wildfires Alter Forest Watersheds and Threaten Drinking Water Quality. *Acc Chem Res*. 52(5):1234–1244. <https://doi.org/10.1021/acs.accounts.8b00670>

Kasischke ES, Melack JM, Dobson MC. 1997. The use of imaging radars for ecological applications—A review. *Remote Sensing of Environment*. 59(2):141–156. [https://doi.org/10.1016/S0034-4257\(96\)00148-4](https://doi.org/10.1016/S0034-4257(96)00148-4)

Kim Y, van Zyl J. 2000. On the relationship between polarimetric parameters. In: Proceedings of IEEE 2000 International Geoscience and Remote Sensing Symposium. Vol. 3. Honolulu, HI, USA; p. 1298–1300 vol.3. <https://doi.org/10.1109/IGARSS.2000.858099>

Kurvonen L, Pulliainen J, Hallikainen M. 1999. Retrieval of biomass in boreal forests from multitemporal ERS-1 and JERS-1 SAR images. *IEEE Transactions on Geoscience and Remote Sensing*. 37(1):198–205. <https://doi.org/10.1109/36.739154>

Lillesand TM, Kiefer RW. 2000. Remote sensing and image interpretation. 4. ed. New York Weinheim: Wiley.

McRoberts RE, Næsset E, Gobakken T, Bollandsås OM. 2015. Indirect and direct estimation of forest biomass change using forest inventory and airborne laser scanning data. *Remote Sensing of Environment*. 164:36–42. <https://doi.org/10.1016/j.rse.2015.02.018>

Neumann M, Saatchi SS, Ulander LMH, Fransson JES. 2012. Assessing Performance of L- and P-Band Polarimetric Interferometric SAR Data in Estimating Boreal Forest Above-Ground Biomass. *IEEE Transactions on Geoscience and Remote Sensing*. 50(3):714–726. <https://doi.org/10.1109/TGRS.2011.2176133>

Persson HJ, Fransson JES. 2015. Analysis of tree height growth with TanDEM-X data. In: 35th EARSeL Symposium. Vol. 1. [place unknown]; p. 1–6.

Persson HJ, Fransson JES. 2016. Estimating Site Index from Short-Term TanDEM-X Canopy Height Models. *IEEE Journal of Selected Topics in Applied Earth Observations and Remote Sensing*. 9(8):3598–3606. <https://doi.org/10.1109/JSTARS.2016.2563158>

Persson HJ, Fransson JES. 2017. Comparison between TanDEM-X- and ALS-based estimation of aboveground biomass and tree height in boreal forests. *Scandinavian Journal of Forest Research*. 32(4):306–319. <https://doi.org/10.1080/02827581.2016.1220618>

Persson HJ, Olsson H, Soja MJ, Ulander LMH, Fransson JES. 2017. Experiences from Large-Scale Forest Mapping of Sweden Using TanDEM-X Data. *Remote Sensing*. 9(12):1253. <https://doi.org/10.3390/rs9121253>

Persson HJ, Ståhl G. 2020. Characterizing Uncertainty in Forest Remote Sensing Studies. *Remote Sensing*. 12(3):505. <https://doi.org/10.3390/rs12030505>

Rauste Y. 2005. Multi-temporal JERS SAR data in boreal forest biomass mapping. *Remote Sensing of Environment*. 97(2):263–275. <https://doi.org/10.1016/j.rse.2005.05.002>

Richards MA, Scheer J, Holm WA. 2010. Principles of modern radar. Melvin WL, editor. Raleigh, NC: SciTech Pub.

Rignot E, Way J, Williams C, Viereck L. 1994. Radar estimates of aboveground biomass in boreal forests of interior Alaska. *IEEE Transactions on Geoscience and Remote Sensing*. 32(5):1117–1124. <https://doi.org/10.1109/36.312903>

Rowland CS, Balzter H, Dawson TP, Luckman A, Patenaude G, Skinner L. 2008. Airborne SAR monitoring of tree growth in a coniferous plantation. *International Journal of Remote Sensing*. 29(13):3873–3889. <https://doi.org/10.1080/01431160801891796>

Saatchi SS, Moghaddam M. 2000. Estimation of crown and stem water content and biomass of boreal forest using polarimetric SAR imagery. *IEEE Transactions on Geoscience and Remote Sensing*. 38(2):697–709. <https://doi.org/10.1109/36.841999>

Sandberg G, Ulander LMH, Fransson JES, Holmgren J, Toan TL. 2011. L- and P-band backscatter intensity for biomass retrieval in hemiboreal forest. *Remote Sensing of Environment*. 115(11):2874–2886. <https://doi.org/10.1016/j.rse.2010.03.018>

Sandberg G, Ulander LMH, Wallerman J, Fransson JES. 2014. Measurements of Forest Biomass Change Using P-Band Synthetic Aperture Radar Backscatter. *IEEE Transactions on Geoscience and Remote Sensing*. 52(10):6047–6061. <https://doi.org/10.1109/TGRS.2013.2294684>

Santoro M, Cartus O, Fransson JES, Wegmüller U. 2019. Complementarity of X-, C-, and L-band SAR Backscatter Observations to Retrieve Forest Stem Volume in Boreal Forest. *Remote Sensing*. 11(13):1563. <https://doi.org/10.3390/rs11131563>

Santoro M, Eriksson LEB, Fransson JES. 2015. Reviewing ALOS PALSAR Backscatter Observations for Stem Volume Retrieval in Swedish Forest. *Remote Sensing*. 7(4):4290–4317. <https://doi.org/10.3390/rs70404290>

Santoro M, Pantze A, Fransson JES, Dahlgren J, Persson A. 2012. Nation-Wide Clear-Cut Mapping in Sweden Using ALOS PALSAR Strip Images. *Remote Sensing*. 4(6):1693–1715. <https://doi.org/10.3390/rs4061693>

Schlund M, Baron D, Magdon P, Erasmi S. 2019. Canopy penetration depth estimation with TanDEM-X and its compensation in temperate forests. *ISPRS Journal of Photogrammetry and Remote Sensing*. 147:232–241. <https://doi.org/10.1016/j.isprsjprs.2018.11.021>

Schlund M, Davidson MWJ. 2018. Aboveground Forest Biomass Estimation Combining L- and P-Band SAR Acquisitions. *Remote Sensing*. 10(7):1151. <https://doi.org/10.3390/rs10071151>

Soja MJ, Persson HJ, Ulander LMH. 2015. Estimation of Forest Biomass from Two-Level Model Inversion of Single-Pass InSAR Data. *IEEE Transactions on Geoscience and Remote Sensing*. 53(9):5083–5099. <https://doi.org/10.1109/TGRS.2015.2417205>

Soja MJ, Persson HJ, Ulander LMH. 2017. Mapping and modeling of boreal forest change in tandem-x data with the two-level model. In: 2017 IEEE International Geoscience and Remote Sensing Symposium (IGARSS). Fort Worth, TX.; p. 2887–2890. <https://doi.org/10.1109/IGARSS.2017.8127601>

Soja MJ, Persson HJ, Ulander LMH. 2018. Modeling and Detection of Deforestation and Forest Growth in Multitemporal TanDEM-X Data. *IEEE Journal of Selected Topics in Applied Earth Observations and Remote Sensing*. 11(10):3548–3563. <https://doi.org/10.1109/JSTARS.2018.2851030>

Solberg S, Næsset E, Gobakken T, Bollandsås O-M. 2014. Forest biomass change estimated from height change in interferometric SAR height models. *Carbon Balance Manage*. 9(1):5. <https://doi.org/10.1186/s13021-014-0005-2>

Sullivan RJ. 2004. Radar foundations for imaging and advanced concepts. Raleigh, NC: SciTech Publ.



Ulaby FT, Moore RK, Fung AK. 1981. Microwave remote sensing: active and passive. Volume I. Microwave remote sensing, fundamentals and radiometry. Norwood, MA: Artech House.

Ulaby FT, Moore RK, Fung AK. 1986. Microwave remote sensing: active and passive. Volume II. Radar remote sensing and surface scattering and emission theory. Norwood, MA: Artech House.

Ulander LMH. 1996. Radiometric slope correction of synthetic-aperture radar images. *IEEE Transactions on Geoscience and Remote Sensing*. 34:1115–1122. <https://doi.org/10.1109/36.536527>

Ulander LMH, Gustavsson A, Flood B, Murdin D, Dubois-Fernandez P, Dupuis X, Sandberg G, Soja MJ, Eriksson LEB, Fransson JES, et al. 2011. BioSAR 2010, Technical Assistance for the Development of Airborne SAR and Geophysical Measurements during the BioSAR 2010 Experiment: Final Report. [place unknown]: European Space Agency.

Wackerly D, Mendenhall W, Scheaffer RL. 2014. *Mathematical Statistics with Applications*. Belmont, CA: Duxbury Press.

Yu H, Lan Y, Yuan Z, Xu J, Lee H. 2019. Phase Unwrapping in InSAR : A Review. *IEEE Geoscience and Remote Sensing Magazine*. 7(1):40–58. <https://doi.org/10.1109/MGRS.2018.2873644>

van Zyl JJ. 2001. The Shuttle Radar Topography Mission (SRTM): a breakthrough in remote sensing of topography. *Acta Astronautica*. 48(5):559–565. [https://doi.org/10.1016/S0094-5765\(01\)00020-0](https://doi.org/10.1016/S0094-5765(01)00020-0)

## Popular science summary

Large scale mapping of changes in forest variables is needed for both environmental monitoring, planning of climate actions and sustainable forest management. Remote sensing can be used in conjunction with field data to produce frequent wall-to-wall estimates that are practically impossible to produce using manual inventory.

Synthetic aperture radar (SAR) can observe the forest independent of sunlight, clouds, snow, or rain, providing reliable high frequency coverage. Its wavelength determines the interaction with the forest, where longer wavelengths interact more with the larger structures of the trees, and shorter wavelengths interact mainly with the top part of the canopy, meaning that the wavelength can be chosen to fit specific applications. Information can also be extracted from the oscillation direction of the radar signal, called its polarization.

This thesis contains five studies conducted on the Remningstorp test site in southern Sweden. Three of the studies predicted above ground biomass (AGB) change using P-band data with a 86 cm wavelength, and L-band data with a 23 cm wavelength. The studies assessed the interaction of the different polarization directions with the forest structures, and especially how the interactions best could be used to predict AGB change.

Studies IV and V instead used X band data with a 3 cm wavelength. The two TanDEM-X satellites that follow parallel orbits side by side use the interference between the signals received by the two satellites to measure height differences on the ground. The process is called interferometric SAR, or InSAR. Time series of such height measurements were used to estimate successive tree heights. In study IV the estimated tree heights were used to detect silvicultural treatments, and in study V they were used to determine the growth rate and age of trees.



## Populärvetenskaplig sammanfattning

Kartläggning av förändringar i skogliga variabler kan utgöra underlag för miljöövervakning, rapportering, planering av klimatåtgärder, och ett hållbart skogsbruk. Fjärranalys kan i kombination med fältinventering användas för att skapa frekventa heltäckande skattningar som är praktiskt omöjliga att åstadkomma med endast fältinventering.

Syntetisk aperturradar (SAR) kan avbilda skogen oberoende av solljus, moln, snöfall, eller regn, och kan därför ge tillförlitliga och frekventa observationer. Interaktionen med skogen är beroende av våglängden, där långa våglängder främst interagerar med de större strukturerna, som stammar och tjocka grenar, och korta våglängder främst reflekteras från den övre delen av trädkronorna. Därför kan våglängden väljas för att passa specifika tillämpningar. Information kan dessutom extraheras ut radarsignalens oscillationsriktning, vilken kallas polarisation.

Denna avhandling innefattar fem studier genomförda på Remningstorps försöksområde i Västergötland. Tre av studierna predikterade förändringar i biomassa ovan jord (B) med hjälp av P-bands-SAR med en våglängd på 86 cm, och L-bands-SAR med en våglängd på 23 cm. Studierna utvärderade interaktionen hos olika polarisationsriktningarna med skogsstrukturerna, och särskilt hur interaktionerna bäst kunde användas för att förutsäga förändringar i B.

Studie IV och V använde istället X-bandsdata med en våglängd på 3 cm. De två TanDEM-X-satelliterna som följer parallella omloppsbanor sida vid sida använder interferens mellan reflekterade signaler för att skatta höjdskillnader på marken. Processen kallas interferometrisk SAR, eller InSAR. Tidsserier av sådana höjdmätningar användes för att skatta trädhöjder under flera år. I studie IV användes de skattade trädhöjderna för att detektera skogsvårdsåtgärder, och i studie V användes de för att skatta trädens ålder och ståndortsindex, ett mått som beskriver tillväxtpotentialen.












## Predictions of Biomass Change in a Hemi-Boreal Forest Based on Multi-Polarization L- and P-Band SAR Backscatter

### Prédictions du changement de la biomasse dans une forêt semi-boréale utilisant la rétrodiffusion RSO multipolarisation en bande L et P

Ivan Huuva<sup>a</sup> , Henrik J. Persson<sup>a</sup> , Maciej J. Soja<sup>b,c</sup> , Jörgen Wallerman<sup>a</sup> , Lars M. H. Ulander<sup>d</sup> , and Johan E. S. Fransson<sup>a</sup> 

<sup>a</sup>Department of Forest Resource Management, Swedish University of Agricultural Sciences, Umeå, Sweden; <sup>b</sup>MJ Soja Consulting, Hobart, Tasmania, Australia; <sup>c</sup>School of Technology, Environments and Design, University of Tasmania, Hobart, Tasmania, Australia; <sup>d</sup>Department of Space, Earth and Environment, Chalmers University of Technology, Gothenburg, Sweden

#### ABSTRACT

Above-ground biomass change accumulated during four growth seasons in a hemi-boreal forest was predicted using airborne L- and P-band synthetic aperture radar (SAR) backscatter. The radar data were collected in the BioSAR 2007 and BioSAR 2010 campaigns over the Remningstorp test site in southern Sweden. Regression models for biomass change were developed from biomass maps created using airborne LiDAR data and field measurements. To facilitate training and prediction on image pairs acquired at different dates, a backscatter offset correction method for L-band data was developed and evaluated. The correction, based on the HV/VV backscatter ratio, facilitated predictions across image pairs almost identical to those obtained using data from the same image pair for both training and prediction. For P-band, previous positive results using an offset correction based on the HH/VV ratio were validated. The best L-band model achieved a root mean square error (RMSE) of 21 t/ha, and the best P-band model achieved an RMSE of 19 t/ha. Those accuracies are similar to that of the LiDAR-based biomass change of 18 t/ha. The limitation of using LiDAR-based data for training was considered. The findings demonstrate potential for improved biomass change predictions from L-band backscatter despite varying environmental conditions and calibration uncertainties.

#### RÉSUMÉ

Les changements de la biomasse accumulée au-dessus du sol dans une forêt semi-boréale ont été prédits au cours de quatre saisons de croissance à l'aide de la rétrodiffusion d'un radar à synthèse d'ouverture (RSO) aéroportée en bande L et P. Les données radar ont été recueillies durant les missions BioSAR 2007 et BioSAR 2010 sur le site test de Remningstorp, dans le sud de la Suède. Des modèles de régression pour le changement de biomasse ont été développés à partir de cartes de biomasse créées à l'aide de données LiDAR aéroportées et de mesures sur le terrain. Afin de faciliter l'entraînement et la prédiction à partir de paires d'images acquises à différentes dates, une méthode de correction du décalage de la rétrodiffusion pour les données en bande L a été élaborée et évaluée. La correction, basée sur le rapport de rétrodiffusion HV/VV, a facilité l'obtention pour des paires d'images de prédictions similaires à celles obtenues pour la même paire d'images et ce tant pour l'entraînement que la prédiction. Pour la bande P, des résultats antérieurs positifs, utilisant une correction de décalage basée sur le rapport HH/VV, ont été validés. Une erreur moyenne de la carrée racine (RMSE) de 21 t/ha et de 19 t/ha a été respectivement obtenue pour le meilleur modèle en bande L et pour celui en bande P. Ces précisions du changement de biomasse étaient semblables à celle des données LiDAR (18 t/ha). La limitation de l'utilisation des données LiDAR pour l'entraînement a aussi été prise en considération. Les résultats démontrent un potentiel d'amélioration des prévisions du changement de la biomasse à partir de la rétrodiffusion de la bande L, malgré des conditions environnementales variables et les incertitudes d'étalement.

#### ARTICLE HISTORY

Received 22 March 2020  
Accepted 14 October 2020

**CONTACT** Ivan Huuva  [ivan.huuva@slu.se](mailto:ivan.huuva@slu.se)

© 2020 The Author(s). Published by Informa UK Limited, trading as Taylor & Francis Group. This is an Open Access article distributed under the terms of the Creative Commons Attribution License (<http://creativecommons.org/licenses/by/4.0/>), which permits unrestricted use, distribution, and reproduction in any medium, provided the original work is properly cited.



## Introduction

Increased concentrations of greenhouse gases in the atmosphere cause global warming, and the largest contributor to this process is carbon dioxide (Stocker et al. 2013). The biosphere acts as a net carbon sink, and changes in its efficiency in storing carbon need to be better understood (Canadell et al. 2007). Forests constitute a large part of the terrestrial biosphere and their carbon storage is proportional to the biomass they contain. This calls for large-scale mapping of forest biomass. Mapping of forest biomass is also of interest in assessing fire, storm, insect, and disease damages, and to support decisions in commercial forest management. Synthetic aperture radar (SAR) systems have the benefit of being able to form images of the terrestrial landscape regardless of clouds, precipitation, and sun illumination conditions, which can inhibit LiDAR or optical systems, making it easier to reliably get full coverage data even over large areas. The relatively long wavelength of L- and P-band SAR systems compared to sensors operating with shorter wavelengths or in the optical domain is an advantage because of the signal penetration into the canopy, which facilitates estimation of above-ground biomass (AGB) (Kasischke et al. 1997).

Advanced SAR methods like InSAR (Solberg et al. 2014; Persson and Fransson 2017) or tomography (Ho Tong Minh et al. 2016) have been used to predict AGB or AGB change, but place high demands on the SAR data in terms of temporal coherence that not all SAR products can meet. In particular, L-band data often do not possess the temporal coherence needed for repeat-pass interferometry over forests (Hamadi et al. 2017; Monteith and Ulander 2018). While data from formation flying satellites ought to overcome this limitation, no such L-band systems are currently in operation. Backscatter-based algorithms for AGB or AGB change prediction do not have this inherent coherency requirement, and can be applied to both L- and P-band data. In this context, simple backscatter-based predictions are more feasible for large-scale mapping of carbon stock dynamics on a national or continental level. Additionally, backscatter algorithms are simpler to implement for non SAR experts, since they can be applied to standard SAR products without the use of specialized SAR software.

Previous studies have used both L- and P-band SAR data to predict AGB, or the highly correlated variable stem volume, in boreal and hemi-boreal forests (Rignot et al. 1994; Kurvonen et al. 1999; Saatchi and Moghaddam 2000; Rauste 2005; Sandberg et al. 2011; Neumann et al. 2012; Santoro et al. 2015;

Schlund and Davidson 2018; Cartus et al. 2019; Santoro et al. 2019). L-band data have also been used to detect clear-cuts and storm damage (Fransson et al. 2007; Santoro et al. 2012), and to estimate AGB growth from multi-satellite SAR data (Balzter et al. 2003). However, algorithms based on backscatter are known to be subject to saturation (loss of sensitivity) when biomass increases beyond a certain level. The onset of sensitivity loss is dependent on the wavelength and forest type, and occurs at 40–100 t/ha and 100–200 t/ha for L- and P-band, respectively, in conifer-dominated forests (Dobson et al. 1992; Le Toan et al. 1992; Rignot et al. 1994; Imhoff 1995; Fransson 1999). While L- and P-band data have previously been compared in their ability to estimate or predict AGB, this study evaluated both bands for prediction of AGB change. The data used in this study are highly comparable between bands as it was acquired in the same geometry over the same area, with almost all acquisitions made on the same days for both bands.

This study extends the work of Sandberg et al. (2014), who analyzed the P-band data from the BioSAR 2007 and BioSAR 2010 campaigns, but omitted the L-band data from the analysis. While the coming BIOMASS mission will operate in P-band, in light of both the scarcity of available P-band data over Europe, and North and Central America in the present and foreseeable future, following the restrictions imposed by the US Department of Defense (Carreiras et al. 2017), and the present and planned L-band missions including ALOS-2, ALOS-4, NISAR, ROSE-L, and SAOCOM (The CEOS database: Missions, instruments, measurements and datasets 2020), it was of interest to expand the analysis to include the L-band data from the same campaigns. Currently, only ALOS-2 PALSAR-2 can, to a certain extent, provide continual global L-band backscatter data sets. In Huuva et al. (2017), single polarization AGB change models were investigated for the L- and P-band data from the campaigns, and it was found that using models based on HV backscatter explained most of the variation in AGB change for both L- and P-band.

In Sandberg et al. (2014), LiDAR-based AGB maps were used to train P-band SAR models. These AGB maps were, however, created using a different method for the two acquisition years. For 2007, the AGB map was created in two steps, by first creating a stem volume map based on field and LiDAR data, which was then converted to an AGB map using biomass expansion factors. For 2010, the AGB map was instead created directly from AGB estimates from field and LiDAR data. In contrast, this study used LiDAR-based

AGB maps created according to a unified and consistent method for both acquisition years to support the analysis and modeling. Unlike Sandberg et al. (2014), individual tree biomass models were applied to the field data for both years, eliminating the need to use biomass expansion factors when creating the AGB maps. This is expected to result in more accurate AGB values (Pettersson et al. 2012). In contrast to the analysis in Sandberg et al. (2014), change predictions were back-transformed to facilitate the comparison of models based on different AGB change transformations. Additionally, while in that study the largest field measured changes used for evaluation were limited in magnitude to 50 t/ha, the evaluation data in the present study were expanded by including additional evaluation plots which were clear-cut between the acquisition years, thereby permitting evaluation of the models on much larger AGB changes, reaching 300 t/ha in magnitude, which is interesting in light of the previously discussed saturation effects.

The intensity of SAR backscatter from a certain location is not only dependent on the amount of biomass and SAR parameters like wavelength, incidence angle, and polarization, but varies with other variables such as soil, stem, and canopy moisture, surface roughness and topography, and forest structure variables such as tree species, stem density, and spatial distribution of trees (Lucas et al. 2010; Kasischke et al. 2011). Moisture can vary significantly with not only seasons but even time of day due to precipitation and diurnal cycles, making it especially challenging when predicting AGB change. The non-AGB related change in backscatter may vary within a given SAR image pair due to, e.g. local precipitation in a region of one of the two images, resulting in wetter soils compared to other areas. Ideally, a non-constant offset correction across scenes would therefore be required. However, a first order approximation can be achieved by estimating the non-AGB related change with a constant offset for a given image pair. While such an offset in backscatter can, when modeling AGB changes from one SAR image pair, be corrected for by a constant term in the model, the offset will generally not be the same for another image pair, thus hindering the applicability of a trained model to other image pairs. To mitigate this effect of moisture and radiometric calibration uncertainty a backscatter change offset correction method was proposed for P-band data by Sandberg et al. (2014). The correction is based on the HH/VV backscatter ratio, found in P-band data to be relatively insensitive to moisture (Soja et al. 2013), and aims to correct the backscatter so that

areas with small changes in AGB also have small changes in backscatter. While the correction method was successful in facilitating AGB change prediction from P-band backscatter data, no such correction method has been developed for L-band data.

The objectives of this study are to develop and evaluate a backscatter offset correction method for L-band SAR data, and to validate the existing correction method for P-band data. In addition, we compare the potential of predicting AGB changes in a hemi-boreal forest using L- and P-band backscatter, given that a suitable offset correction method can be applied to both bands.

## Materials and methods

### Test site

The remote sensing data consisted of SAR and LiDAR data collected during the airborne SAR campaigns BioSAR 2007 and BioSAR 2010 conducted at the Remningstorp estate (Figure 1), in southern Sweden (58°30'N, 13°40'E). In addition, parts of the *in situ* data were also collected within the campaigns. Full descriptions of the campaigns can be found in the BioSAR reports by Hajnsek et al. (2008) and Ulander et al. (2011). The test site is located within the hemi-boreal zone, which covers the transition between the boreal and temperate zones. This zone is characterized by mixtures of coniferous and deciduous species. The test site consists of managed forest dominated by Norway spruce (*Picea abies* (L.) H.Karst.) and Scots pine (*Pinus sylvestris* L.) with some birch (*Betula* spp.). In a Swedish context, the climate and geology are favorable for forest growth. Two thirds of the forest within the estate are located on till (i.e. a mixture of glacial debris) with a field layer consisting of different herbs, blueberry (*Vaccinium myrtillus* L.), and narrow-leaf grass (e.g. *Deschampsia flexuosa* (L.) Trin.). In denser old spruce stands the field layer is absent. The remaining forest grows on peatland, which is dominated by Scots pine. Regardless of tree cover, the main soil type on till is brown earth. Extensive ditching of peatlands on the estate over the years has been conducted to increase the productive forest area. However, some of the peatlands are frequently saturated (Ahlberg and Kardell 1997). The above-ground biomass range is 0–400 t/ha, at plot level (with 10 m radius). The ground slopes on the test site are generally small, with an average slope of 4° and a 95th percentile of 11.5°, as calculated from the 2 m × 2 m resolution LiDAR-based digital terrain

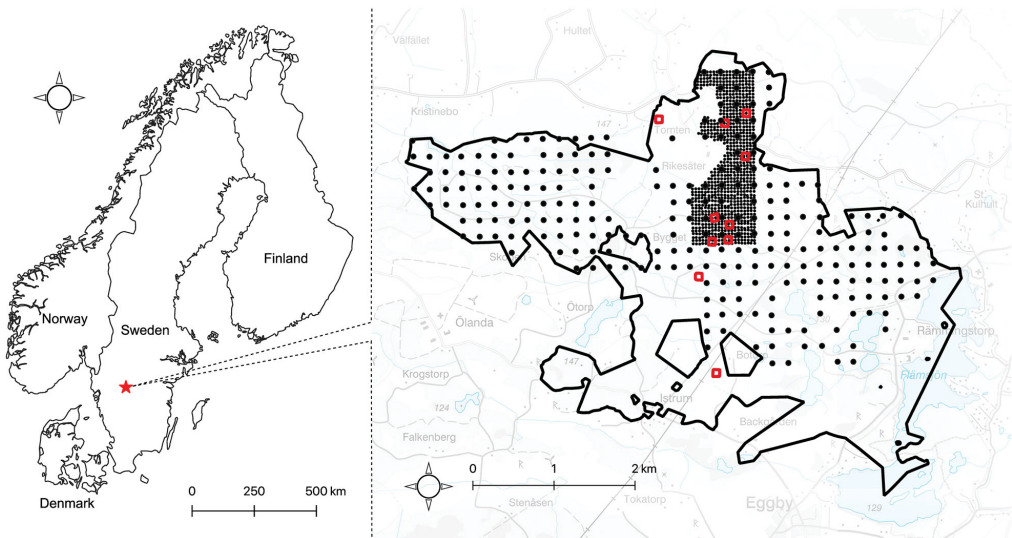


**Figure 1.** The Remningstorp estate, located in southern Sweden. The field plots for the 2004–2005 and 2007 inventories are pictured using black markers (all plots with a radius of 10 m). The 2004–2005 inventory used a plot spacing of 40 m, while the 2010 inventory used a spacing of 200 m. The ten  $80\text{ m} \times 80\text{ m}$  plots, inventoried in 2007 and 2010, and used for evaluation in the study, are outlined in red. Country outlines © Esri, and background map of Remningstorp © Lantmäteriet.

model (DTM). The ground surface topology lies between 120 m and 145 m above sea level.

### *In situ data*

Three sets of field plot data were inventoried at the Remningstorp test site. The first set consisted of a systematic grid with 849 circular plots with 10 m radius and 40 m plot spacing. The inventory was started before, and completed after the vegetation season in 2005. In order to match the SAR data, the forest variable estimates were forecast to 2007, using established models in the Heureka forestry decision support system (Lämås and Eriksson 2003; Wikström et al. 2011). The second data set, part of the BioSAR 2010 campaign, was inventoried after the growth season 2010, and consists of 216 circular plots with 10 m radius and 200 m spacing (Sandberg et al. 2011; Ulander et al. 2011). The third data set consisted of ten  $80\text{ m} \times 80\text{ m}$  plots, distributed across the Remningstorp estate, all but one fully contained within homogeneous stands. All ten large plots were surveyed just before the growth season of 2007. Three of the large plots were clear-cut between 2007 and 2010, and the remaining seven large plots were inventoried again after the growth season of 2010, thereby matching the SAR data without forecasting. The AGB was set to 0 t/ha in 2010 for the three large plots that

were clear-cut between the acquisitions. One third of plot 9 was not clear-cut, since two of its corners are located in another, retained, stand. Therefore, only data from the central part of this plot, contained in the clear-cut, was used to represent the whole plot, as if the whole plot were clear-cut. Details of these large plots are given in Table 1.

For all data sets, all trees with a diameter at breast height (DBH, measured at 1.3 m above ground) of more than 4 cm were calipered, species determined, and positioned using a real time kinematic global positioning system. For the data sets consisting of circular plots, the height was measured on about 10% of the trees, randomly sampled with probability proportional to the basal area, using a hypsometer. For the  $80\text{ m} \times 80\text{ m}$  plots, the height of every calipered tree was measured. AGB was estimated using the Heureka system (Wikström et al. 2011), which used established models for height by Söderberg (1986) and AGB by Marklund (1988). Only plots found to be completely contained in a single stand, and with a Lorey's mean tree height (i.e. basal area weighted mean tree height) above 3.7 m (corresponding to DBH greater than 4 cm) were used in the study. This resulted in sample sizes of 763 and 208 plots from 2005 and 2010, respectively. In addition to the three field data sets, a stand delineation map over the area was used to allocate training and validation sets in the evaluation of regression models.

**Table 1.** Data for ten 80 m × 80 m plots for which field measurements were made before the growth season of 2007, and after the growth season of 2010.

Plot ID	AGB 2007 [t/ha]	AGB 2010 [t/ha]	AGB change [t/ha]	Stem density 2007	Stem density 2010	Dominant species
1	195.3	205.8	10.5	267	261	Scots pine
5	150.5	99.7	-50.8	539	174	Scots pine
9	243.3	0	-243.3	287	0	Norway spruce
10	167.3	182.3	15	418	389	Norway spruce
12	298.3	0	-298.3	361	0	Norway spruce
14	50.6	60.4	9.8	337	330	Birch
15	126	135.3	9.3	401	397	Birch
16	303	0	-303	362	0	Norway spruce
17	145.4	173	27.6	374	362	Norway spruce
18	222	245	23	321	303	Norway spruce

**Table 2.** Volumetric soil moisture and air temperature for each scene acquired from E-SAR and SETHI.

Acquisition date	Scene ID	Band	Volumetric soil moisture [%]	Air temperature [°C] (local time)
09/03/2007	104	L	21	2.6 (07:00), 4.8 (19:00)
09/03/2007	109	P	21	2.6 (07:00), 4.8 (19:00)
31/03/2007	205	L	17	4.8 (08:00), 7.1 (20:00)
02/04/2007	306	P	17	6.0 (08:00), 6.5 (20:00)
02/05/2007	405	L	13	7.3 (08:00), 13.8 (20:00)
02/05/2007	411	P	13	7.3 (08:00), 13.8 (20:00)
23/09/2010	bio01L	L	11	8.4 (08:00), 14.2 (20:00)
23/09/2010	bio01P	P	11	8.4 (08:00), 14.2 (20:00)
23/09/2010	bio02L	L	11	8.4 (08:00), 14.2 (20:00)
23/09/2010	bio02P	P	11	8.4 (08:00), 14.2 (20:00)

Moreover, tree species information from a forest management plan of the estate was used in creating a LiDAR-based biomass map of the test site, as explained below. The average size of a stand in the test site was 2.5 ha, and the area covered by all remote sensing data sets contained 158 stands.

Since the 10 m radius field plot grids for the two years were not the same, and the number of shared plots was small, changes in AGB could not be directly measured *in situ* with a reasonable amount of field plots. Instead, AGB maps were created for 2007 and 2010 using the field plots and LiDAR data. The AGB maps are further described below. The 80 m × 80 m plots were set aside for validation of the results, and were thus not used in model selection or training.

### SAR data

The SAR scenes used are fully polarimetric in L- and P-band. For 2007, the SAR data were collected using the German E-SAR system by the German Aerospace Center (DLR), while the 2010 SAR data were collected using the French SETHI system by ONERA. The two systems and hence the SAR data for the two years are not identical. While the acquisitions in 2010 were all conducted on the same day, the SAR data for 2007 were collected during four dates ranging from early spring with recently thawed snow cover and wet soil,

to late spring and dry soil. Soil moisture was continuously measured using an Aquaflex sensor installed 15 cm below ground in a forested area within the test site. In addition, air temperature and precipitation were recorded at a weather station located in the eastern part of the estate (Table 2). At the time of SAR acquisition, no precipitation was observed (Hajsek et al. 2008; Ulander et al. 2011).

To eliminate the influence of different imaging geometries between the bands, only acquisitions with heading (along-track direction) 200° were chosen for the analysis. All of the selected acquisitions were made from the same flight track, i.e. the incidence angle for a given location on ground is the same in all images (regardless of sensor). The acquisition dates are given in Table 2. For both bands, one image per acquisition date in 2007 was included. The first and last 2007 acquisition dates are the same for L- and P-band, with about two months passing between them, while the intermediate date differs by two days between the bands. For each band, both scenes in the chosen heading for 2010 were included in the analysis to allow both images to be different across image pairs. However, the differences between the scenes from the same date are expected to be small. Table 3 lists the image pairs used in the subsequent analysis. The 2007 data, from E-SAR, were geometrically calibrated using corner reflectors deployed at the test site.

**Table 3.** Image pairs used in the analysis.

Image pair ID	E-SAR scene ID	SETHI scene ID	E-SAR acquisition date	SETHI acquisition date
L <sub>a</sub>	104	bio01L	09/03/2007	23/09/2010
L <sub>b</sub>	205	bio01L	31/03/2007	23/09/2010
L <sub>c</sub>	405	bio01L	02/05/2007	23/09/2010
L <sub>d</sub>	104	bio02L	09/03/2007	23/09/2010
L <sub>e</sub>	205	bio02L	31/03/2007	23/09/2010
L <sub>f</sub>	405	bio02L	02/05/2007	23/09/2010
P <sub>a</sub>	109	bio01P	09/03/2007	23/09/2010
P <sub>b</sub>	306	bio01P	02/04/2007	23/09/2010
P <sub>c</sub>	411	bio01P	02/05/2007	23/09/2010
P <sub>d</sub>	109	bio02P	09/03/2007	23/09/2010
P <sub>e</sub>	306	bio02P	02/04/2007	23/09/2010
P <sub>f</sub>	411	bio02P	02/05/2007	23/09/2010

All images were acquired from the same flight track, in the same imaging geometry.

The reflectors were also used to validate the radiometric calibration of the data. For the 2010 data, from SETHI, the corner reflectors were used for both geometric and radiometric calibration. The radiometric calibration uncertainty was estimated to be  $\pm 1$  dB for both SAR systems.

The delivered geocoded standard products of the two SAR systems were used for the analysis. A full description of the SAR data can be found in the BioSAR reports (Hajnsek et al. 2008; Ulander et al. 2011). A brief summary of the main characteristics of the data used is presented here.

The 2007 SAR data, from E-SAR, were acquired with a center frequency of 1,300 MHz and a bandwidth of 94 MHz for L-band, and a center frequency of 350 MHz and a bandwidth of 70 MHz for P-band. The center frequencies correspond to wavelengths of 23 cm and 86 cm for L- and P-band, respectively. The single look resolutions of the data were  $2.1 \text{ m} \times 0.9 \text{ m}$  for L-band and  $2.1 \text{ m} \times 1.6 \text{ m}$  for P-band (slant range  $\times$  azimuth). The L-band data were multilooked by DLR 8 times, and the P-band data 4 times, both only in azimuth, with a 50% overlap. The resulting resolution for both bands was  $2.1 \text{ m} \times 4.0 \text{ m}$ .

The 2010 SAR data, from SETHI, were collected with a center frequency of 1,325 MHz and a bandwidth of 150 MHz for L-band, and a center frequency of 360 MHz and a bandwidth of 166 MHz for P-band, with some notches and gaps in the latter spectrum to avoid radio frequency interference. The center frequencies correspond to wavelengths of 23 cm and 83 cm for L- and P-band, respectively. The single look resolutions of the L- and P-band data were  $0.9 \text{ m} \times 0.9 \text{ m}$  and  $0.8 \text{ m} \times 0.8 \text{ m}$  (slant range  $\times$  azimuth), respectively.

The SAR images were radiometrically corrected for local ground slope and incidence angle induced variations in the intensity and transformed to  $\gamma^0$  using a  $2 \text{ m} \times 2 \text{ m}$  resolution DTM. From the DTM, the surface normal for each  $2 \text{ m} \times 2 \text{ m}$  pixel was obtained. The angle  $\psi$  between the surface normal and the

slant range image plane normal was then used to obtain the average radar cross section per unit ground area,  $\sigma^0$ , according to

$$\sigma^0 = \beta^0 \times \cos(\psi), \quad (1)$$

where  $\beta^0$  is the average radar cross section per image pixel area (Ulander 1996). After this, a first order correction for variations in incidence angle was applied to obtain

$$\gamma^0 = \sigma^0 / \cos(\theta), \quad (2)$$

where  $\theta$  is the local incidence angle (Ulaby et al. 1982). The radiometrically corrected backscatter  $\gamma^0$  will henceforth be referred to as *backscatter*. The resulting backscatter images were averaged with a  $50 \text{ m} \times 50 \text{ m}$  filter and resampled to *backscatter maps* with  $50 \text{ m} \times 50 \text{ m}$  pixels following the methodology in Sandberg et al. (2014). The resampling has the effect of suppressing most of the speckle in the SAR data, as a pixel of  $50 \text{ m} \times 50 \text{ m}$  contains between 700 and 4,000 resolution cells. This is also expected to make the differences in original resolution between the sensors negligible. The selected pixel size is on the same order of magnitude as the  $80 \text{ m} \times 80 \text{ m}$  plots used for evaluation of AGB change predictions, while still permitting the models to capture biomass variations on a sub-stand scale.

### LiDAR data

LiDAR acquisitions for both years were made using helicopter-mounted TopEye systems (Mk II in 2007, Mk III in 2010). The 2007 scanning was performed on April 24 with densities of 30–40 pulses/m<sup>2</sup>. In 2010, the scanning took place on August 29 with an average density of 69 pulses/m<sup>2</sup>. Further details can be found in the BioSAR reports (Hajnsek et al. 2008; Ulander et al. 2011). In processing the point clouds, point densities were locally found to be significantly lower than the averages, and to avoid artifacts in the

AGB modeling from the varying point density, the point clouds were thinned to 10 points/m<sup>2</sup> to obtain an even point density throughout the test site.

### LiDAR-based biomass maps

The field data from the two inventory years were not from the same set of plots, necessitating an indirect approach to estimate the AGB change from 2007 to 2010. Therefore, AGB maps were created using data from the LiDAR measurements.

Multiple linear regression models were developed to relate *in situ* AGB values with LiDAR percentiles and density metrics. The biomass modeling included investigation of numerous transformations of both the response and explanatory variables, and inspection of scatter plots, residual plots, and covariances. As the AGB state predictions for each year were to be used to compute the AGB change, the determination of a common model that could describe both of the data sets well was prioritized. A log-log model was selected that fulfilled the requirements of linearity, normality and homoscedasticity for both LiDAR data sets. The relationship between AGB and LiDAR metrics was similar for spruce dominated plots for both years, while pine and deciduous dominated plots exhibited relationships that were different both from each other and from spruce dominated plots, and differed for the different years. The regression model used indicator and interaction variables to handle the different relations due to tree species (pine and deciduous) and acquisition year. A plot was defined as pine or deciduous dominated if the fraction of biomass from pine or deciduous trees was 0.7 or higher. Accordingly, a single overall model was fit to the LiDAR and field data for both acquisition years. The model was given by

$$\ln(\text{AGB}_i) = \beta_0 + \beta_{0k} + (\beta_1 + \beta_{1k}) \cdot \ln(P_{50\%i}) + (\beta_2 + \beta_{2k}) \cdot \ln(P_{90\%i} \cdot \text{dns}_i) + \epsilon_i, \quad (3)$$

where  $i$  denotes an observation,  $\epsilon_i$  is an error term,  $\beta_0$  is a common intercept term,  $\beta_{ik} = 0$  for spruce dominated plots for both years, and  $k=1$  for pine dominated plots scanned in 2007,  $k=2$  for deciduous dominated plots scanned in 2007,  $k=3$  for pine dominated plots scanned in 2010, and  $k=4$  for deciduous dominated plots scanned in 2010.  $P_{50\%}$  and  $P_{90\%}$  are the 50th and 90th height percentiles of points above 1.37 m, and  $\text{dns}$  is the canopy density, computed as the fraction of all points in an observation that are above this height.

The accuracy of the LiDAR-based AGB model was estimated by calculating the root mean square error

(RMSE) of predictions by applying leave-one-out cross-validation on the plots used to create them. The RMSE of the AGB model was 32.4 t/ha, corresponding to 23.1% of the mean AGB derived from the field measurements of both years. The coefficient of determination,  $R^2$ , was found to be 0.78.

By applying the model to LiDAR metrics over the test site, and stand level dominant species information from the forest management plan, AGB maps for each year were produced with a 17.5 m × 17.5 m pixel size to match the pixel area with that of the field plots (with a radius of 10 m). The maps were subsequently resampled through spatial averaging to 50 m × 50 m pixels coregistered with the backscatter maps. The resampling has the effect of further reducing the prediction variance, as the resampled pixel value is essentially a mean value of about eight predictions of the model relating AGB to LiDAR metrics.

The change prediction accuracy of the AGB maps was evaluated by computing the average pixel differences between 2007 and 2010 for all pixels inside the ten 80 m × 80 m plots, and comparing these values to the AGB differences derived from the field measurements from these plots. In the calculation, the value of a pixel partially inside a plot was weighted by the fraction of its area covered by the plot polygon. The change prediction RMSE of the LiDAR-based AGB maps was determined to be 18.1 t/ha (5.5% of the range of field measured AGB change in the ten evaluation plots) with a bias of 2.0 t/ha. Although the uncertainties of both AGB maps are combined when the difference between them is evaluated, the lower RMSE is not surprising, since the evaluation plots are much larger than the 10 m radius plots used to estimate the uncertainty in the AGB model itself.

### Backscatter offset correction

The backscatter intensity varies due to environmental conditions such as moisture variations. For both L- and P-band, the SAR data used in this study showed significant changes in backscatter for areas with little change in AGB between the acquisition years. Scatterplots of the differences from all image pairs of both bands are shown in Figure 2.

Most of the data points are clustered around relatively low positive values of AGB change, indicating natural growth, while larger AGB changes present in the data are from clear-cuts in stands with relatively high AGB, resulting in a tail of large negative changes in AGB. Aside from a significant spread in backscatter change for the same AGB change, we can observe that

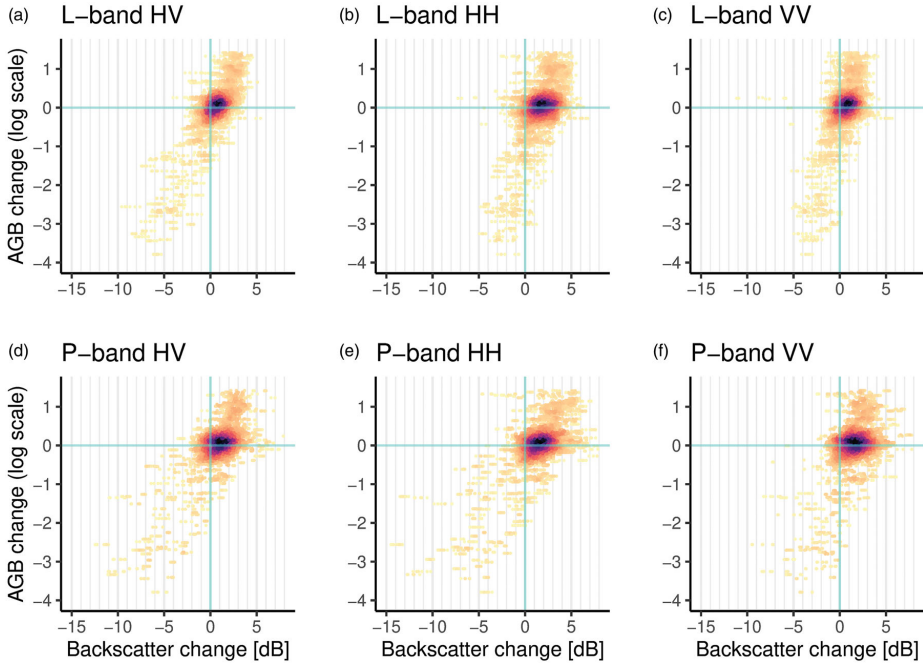


**Figure 2.** Bivariate plots of AGB change and backscatter change between 2007 and 2010 for all L-band image pairs (a–c), and all P-band image pairs (d–f). A data point corresponds to the change in value for a  $50\text{ m} \times 50\text{ m}$  pixel between the AGB maps and between the images in one of the backscatter map pairs. The change scales for AGB and backscatter are defined in Equations 11 and 14, respectively. Points are colored according to the density of points around that location in the plot. The darker the color, the higher the density.

many points close to zero AGB change are not centered around zero in backscatter change, but are offset by 1–2 dB for both bands. While all image pairs have a positive offset, its magnitude differs between different image pairs, as witnessed by the horizontal striping in the plots. These differences in offset pose a problem in constructing a linear model of AGB change that would generalize across different image pairs. To mitigate these offsets, Sandberg et al. (2014) proposed a backscatter change offset correction method for P-band data. The correction was based on the HH/VV backscatter ratio, found to be correlated with biomass but relatively insensitive to changes in moisture (Soja et al. 2013; Sandberg et al. 2014). To find a suitable method for correcting L-band data, the correction method was generalized by analyzing different candidate polarization ratios.

The backscatter offset correction procedure is as follows. For each pair of scenes, find the set of  $50\text{ m} \times 50\text{ m}$  pixels,  $\Omega$ , that have a change in the chosen polarization ratio  $\Delta R$ , on a decibel scale, within some threshold  $t$ . Then, choose a polarization, calculate the mean backscatter level of the pixels in  $\Omega$

for each year, multiply each full image in the pair by the mean of the two  $\Omega$ -means, and divide it by its own  $\Omega$ -mean. The resulting images have the same mean backscatter in the low  $\Delta R$  pixels for each year. For an image pair  $I_1$  and  $I_2$ , Equations 4 and 5 give the corrected images  $I_1'$  and  $I_2'$ , when applied separately to each of the polarizations of  $I_1$  and  $I_2$ :

$$I_1' = I_1 \times ((q_1 + q_2)/2)/q_1, \quad (4)$$

$$I_2' = I_2 \times ((q_1 + q_2)/2)/q_2, \quad (5)$$

where  $q_1$  and  $q_2$  are the mean backscatter of  $I_1$  and  $I_2$  over areas with  $\Delta R$  within  $t$ , that is,

$$q_1 = \text{mean}(I_1(\Omega)), \quad (6)$$

$$q_2 = \text{mean}(I_2(\Omega)). \quad (7)$$

Figure 3 shows the changes in backscatter polarization ratios HH/VV, HV/VV, and HV/HH for all L- and P-band pairs. At P-band, the offset for the ratio HH/VV (Figure 3d) was clearly smaller than the offset of the single polarization channels themselves (Figure 2d–f). Despite backscatter offsets due to moisture changes and possible radiometric calibration

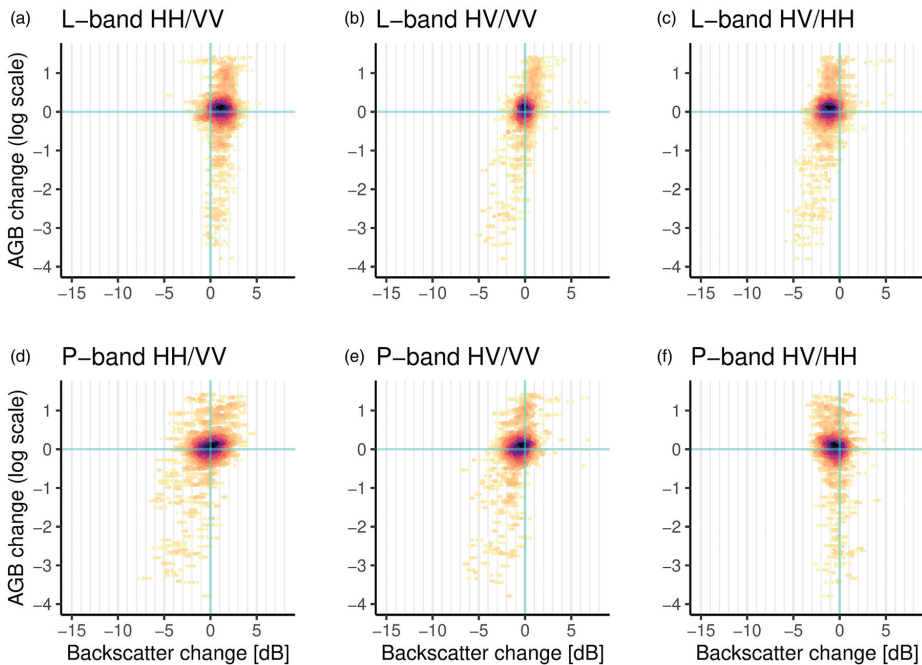


**Figure 3.** Bivariate plots of AGB change and polarization ratio change between 2007 and 2010 for all L-band image pairs (a–c), and all P-band image pairs (d–f). A data point corresponds to a change in value for a  $50\text{ m} \times 50\text{ m}$  pixel between the AGB maps and between the images in one of the backscatter map pairs. The change scales for AGB and backscatter are defined by Equations 11 and 14, respectively. Points are colored according to the density of points around that location in the plot. The darker the color, the higher the density.

errors, the HH/VV ratio could therefore be used to detect areas with relatively low changes in AGB between SAR acquisitions, and the images from the two acquisitions could then be corrected so that the average backscatter in these areas was equal in each image. The HV/VV ratio also showed a dependence on AGB change (Figure 3e), but with a slightly negative offset, albeit significantly smaller than the offset in backscatter of the individual polarization channels. The HV/HH ratio showed no apparent dependence on AGB change and a slight negative offset.

At L-band, the HH/VV ratio was weakly correlated with AGB change, and it furthermore showed a positive change in backscatter irrespective of AGB change (Figure 3a). As such, it was not suitable for correcting L-band data in the manner described above. Instead, the HV/VV ratio of the L-band data showed the desired characteristics of sensitivity to AGB change paired with an insensitivity for changes external to AGB change (Figure 3b). The HV/HH showed a dependence on AGB change, but also an average negative offset of about 2 dB for pixels with no change in AGB. In this study, the L-band data were therefore

offset corrected using the HV/VV ratio, while the P-band data were corrected using the HH/VV ratio as in Sandberg et al. (2014).

A suitable threshold  $t$  for backscatter correction was assessed by calculating the change in mean backscatter for pixels with a small change in the AGB maps, i.e. pixels with a change in AGB on a natural logarithmic scale less than 0.1. Figure 4 shows how this remaining backscatter offset depends on the threshold used for L- and P-band. The two correction methods reduced the backscatter offset for areas with small changes in AGB significantly. Many of the estimated offsets for the different channels were not within the radiometric calibration uncertainty of  $\pm 1\text{ dB}$  reported by DLR and ONERA. In the worst case, this could lead to a calibration offset with a magnitude of  $\pm 2\text{ dB}$ . For both bands, the remaining offset was greatly reduced when applying a correction using even a small threshold. Note that uncorrected data were plotted as being corrected using a threshold of zero in Figure 4. Then, after initial fluctuations as the threshold was increased, a minimum magnitude of the offset was achieved. As the threshold was further increased, the offset started to grow again



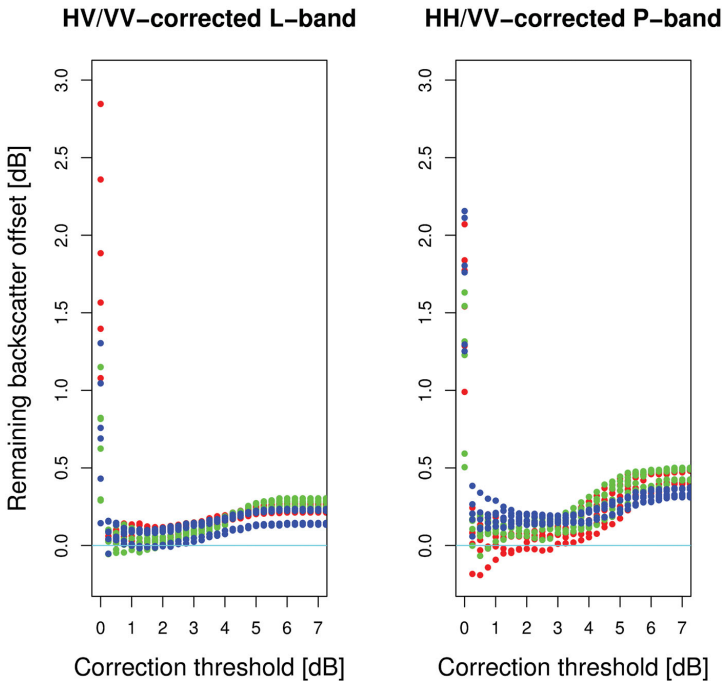


**Figure 4.** Bivariate plots of estimated remaining backscatter offset versus correction threshold for all polarizations of all image pairs. Red, green, and blue markers correspond to HH, HV, and VV polarizations, respectively.

as a larger portion of the images was used for the correction. Finally, as the full dynamic range of the images was within the threshold, the remaining offset became constant.

Backscatter correction using the HV/VV-ratio at a threshold of 2 dB reduced the offset in L-band backscatter from at most 2.85 dB to within 0.12 dB for all image pairs and polarizations (Figure 4). The difference in offset between image pairs for a given polarization was also greatly reduced from at most 1.77 dB to 0.12 dB or less for all polarizations. Backscatter correction using the HH/VV ratio at a threshold of 3 dB reduced the offset in P-band data from a maximum of 2.16 dB to within 0.19 dB for all image pairs and polarizations. For P-band, the largest difference in offset between image pairs was also reduced from about 1.13 dB to 0.11 dB or less for all polarizations. This reduction in offset *difference* is really the important metric, since the aim was to train a model on data from one pair of images, and predict AGB change on data from another image pair. The difference in offset should be small so that the constant term in the model is applicable across image pairs. Based on this evaluation, backscatter offset correction using thresholds of 2 dB and 3 dB was performed on the L- and

P-band SAR data, respectively, before the model selection. It was noted that the correction was not sensitive to the precise value of the threshold, and that values within  $\pm 1$  dB gave very similar correction results.

Scatterplots of offset corrected backscatter maps from all image pairs using the chosen thresholds are shown in Figure 5. Comparing to the scatterplots of uncorrected backscatter change in Figure 2, we can see that the corrections have succeeded in reducing the offset so that the scatterplots in Figure 5 are centered at the origin, and that areas of low backscatter change were roughly centered on zero change in AGB. The horizontal striping of the plots was also reduced, as the differences in offset between different image pairs were reduced.

### Modeling of AGB change using backscatter

The LiDAR-based AGB maps were used in the multiple linear regression analysis to select and train backscatter change models. The evaluation plots and non-forest areas were masked out, and only pixels available in the AGB maps for both 2007 and 2010 were used. The data set then consisted of 1,355 50 m  $\times$  50 m pixels for each image. The incidence

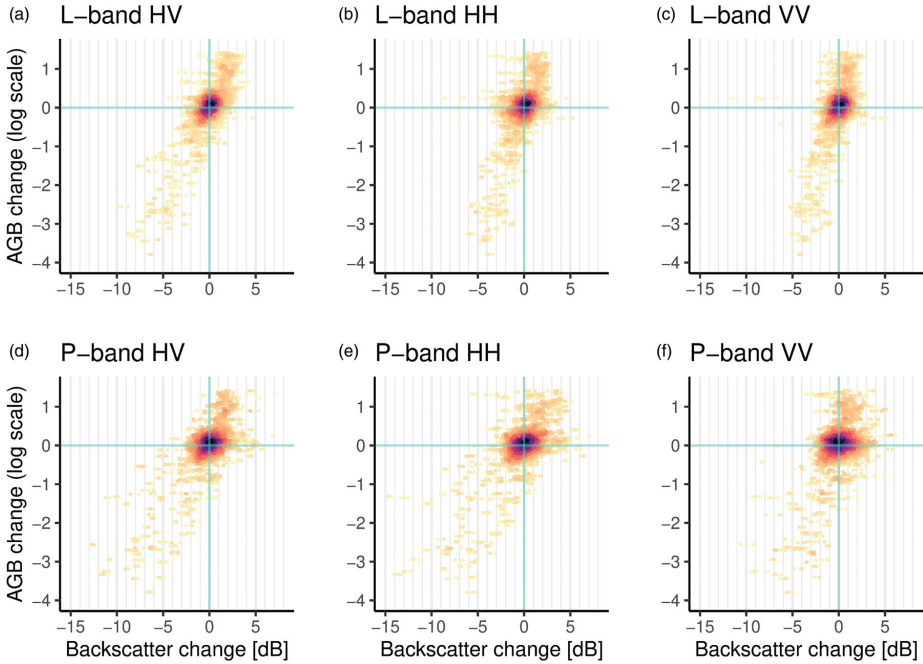


**Figure 5.** Bivariate plots of AGB change versus backscatter change between 2007 and 2010 for all L-band image pairs (a–c), and all P-band image pairs (d–f) after backscatter offset correction. A data point corresponds to the change in value for a 50 m by 50 m pixel between the AGB maps and between the images in one of the backscatter map pairs. The change scales for AGB and backscatter are defined in Equations 11 and 14, respectively. Points are colored according to the density of points around that location in the plot. The darker the color, the higher the density.

angle for the SAR data used in the analysis ranged from  $28^\circ$  to  $50^\circ$ . The dependence of backscatter change on AGB change is not linear, and therefore a number of transformations of both AGB and backscatter were investigated in the model selection process. The transformations are an attempt to empirically find a suitable model that is linearly correlated with the LiDAR-based AGB maps. To mitigate overfitting, a cross-validation procedure was used in the model selection. The regression models investigated are generally given by

$$y = b_0 + b_1 x_{HV} + b_2 x_{HV}^2 + b_3 x_{HH} + b_4 x_{HH}^2 + b_5 x_{VV} + b_6 x_{VV}^2 + \epsilon, \quad (8)$$

where the response variable  $y$  is the AGB change on the linear, square root, or logarithmic scales defined in Equations 9, 10, and 11, respectively:

$$\Delta AGB \cong AGB_{after} - AGB_{before} \quad (9)$$

$$\Delta \sqrt{AGB} \cong \sqrt{AGB_{after}} - \sqrt{AGB_{before}} \quad (10)$$

$$\Delta \ln(AGB) \cong \ln AGB_{after} - \ln AGB_{before} \quad (11)$$

The  $b_k$  are the regression coefficients and  $\epsilon$  is an error term. The  $x_{ij}$  in Equation 8 are backscatter change in amplitude, power or decibel (dB) units defined according to Equations 12, 13, and 14, respectively, for a given polarization.

$$\Delta \gamma_A^0 \cong \sqrt{\gamma_{after}^0} - \sqrt{\gamma_{before}^0} \quad (12)$$

$$\Delta \gamma^0 \cong \gamma_{after}^0 - \gamma_{before}^0 \quad (13)$$

$$\Delta \gamma_{dB}^0 \cong 10 \log_{10}(\gamma_{after}^0) - 10 \log_{10}(\gamma_{before}^0) \quad (14)$$

Different backscatter change measures were not mixed in the same model, meaning the same transformation was applied to all explanatory variables for a certain model. The described response and explanatory variable transformations result in nine different transformation combinations for the left and right hand side of Equation 8. All submodels of these with two to five non-zero regression coefficients  $b_k$  were included as candidate models. Since the intercept  $b_0$  is always included, this means all models with one to

four explanatory variables were investigated. The different combinations of response variable and explanatory variable transformations, and the different possible choices of explanatory variables give a total of 504 possible models.

As a first step of two in the model selection, the models with the highest adjusted  $R^2$  out of all models with the same number of explanatory variables and the same response variable transformation were chosen. This was done separately for each response variable transformation, since adjusted  $R^2$  values cannot be compared across different response variable transformations. Additionally, a model was not chosen if its adjusted  $R^2$  was not increased compared to a model with fewer variables with the same response variable transformation.

As the same model was to be used for all image pairs, we were interested in models that simultaneously fit data from all pairs. Because of this, the first step of model selection was done on the backscatter offset corrected data, with data from all image pairs concatenated into one combined data set on which the model parameters were estimated. The backscatter offset correction adjusts the relation between backscatter change and AGB change to be similar across image pairs.

### ***Cross-validation of backscatter-based AGB change models***

In the second step of model selection, an approach that was denoted leave-one-stand-out (LOSO) cross-validation was used to validate the AGB change predictions. Using the stand delineation map, each model was trained on data from all stands but one, and then evaluated on the left-out stand. This was repeated until each stand had been used once for evaluation. The LOSO cross-validation reduced the computational cost compared to leave-one-out cross-validation at the pixel level, and aggregated alternatives such as spatial leave-one-out cross-validation, as proposed by Le Rest et al. (2014). The latter has been used to overcome spatial autocorrelation and was demonstrated in the modeling of ecological processes.

Since the models should be applicable between image pairs, the cross-validation was simultaneously conducted not only across stands, but also across image pairs. This showed the potential of using a model trained in one area on one image pair to predict AGB changes in another area from another image pair.

The procedure was repeated for all image pairs and the average performance of each model over all image pair combinations was estimated to produce an overall pixel level root-mean-square deviation (RMSD), and a stand level RMSD for each model. RMSD was used to denote comparisons with LiDAR-generated references, while RMSE was used to denote comparisons with field-based references. RMSD is calculated in the same manner as RMSE, the only difference being the used reference data set.

RMSD values were also calculated by applying LOSO cross-validation, but without switching image pairs between training and validation. The difference between these in-pair RMSDs (best-case conditions) and the across-pair RMSDs (showing temporal stability) was the accuracy loss (in terms of RMSD) when training a model on one pair of images, and predicting on another pair of images. Additionally, in-pair and across-pair biases were estimated through calculating the mean residuals for all image pair combinations. The biases were estimated through comparisons with both the LiDAR-based AGB change and the field measured AGB change in the evaluation plots.

To be able to compare models with different transformations of the response variable, the predictions on logarithmic and square root form were back-transformed and corrected for back-transformation bias prior to computing RMSDs. The predictions on logarithmic form were bias corrected using a ratio estimator according to Snowdon (1991), while the predictions on the square root scale were bias corrected following the method described in Gregoire et al. (2008).

## **Results**

### ***Comparisons with LiDAR estimated AGB change***

Summaries of the validation results are presented in Tables 4 and 5 (L- and P-band, respectively). These accuracies were used as criteria for the model selection. For both bands, for a given number of variables, the best performance when compared on the pixel level to the LiDAR-based AGB maps was achieved for the AGB change modeled on the square root scale and backscatter change modeled on the logarithmic (dB) scale. For these models, at L-band, the standard deviations of RMSDs from different image pair combinations were within 1 t/ha. At P-band, the corresponding values were within 0.5 t/ha. At L-band, there was a decrease in RMSD of about 4 t/ha and 6 t/ha for the pixel and stand level, respectively, when

**Table 4.** Validation accuracy of cross-validated L-band models trained and evaluated on different image pairs.

AGB change measure	$\gamma^0$ change measure	Number of variables	Pixel-RMSD [t/ha]	Pixel-RMSD min [t/ha]	Pixel-RMSD max [t/ha]	Pixel-RMSD SD [t/ha]	Stand-RMSD [t/ha]
$\Delta\sqrt{AGB}$	$\Delta\gamma_{dB}^0$	2	22.2	21.4	23.3	0.6	18.2
$\Delta\sqrt{AGB}$	$\Delta\gamma_{dB}^0$	3	22.3	21.4	23.2	0.5	18.3
$\Delta\sqrt{AGB}$	$\Delta\gamma_{dB}^0$	4	22.4	21.5	23.4	0.5	18.4
$\Delta AGB$	$\Delta\gamma_{dB}^0$	2	26.1	25.4	27.1	0.5	19.1
$\Delta AGB$	$\Delta\gamma_{dB}^0$	3	26.2	25.4	27.2	0.5	19.1
$\Delta AGB$	$\Delta\gamma_{dB}^0$	4	26.3	25.5	27.5	0.6	19.3
$\Delta\sqrt{AGB}$	$\Delta\gamma_{dB}^0$	1	26.3	24.6	28.0	1.0	24.1
$\Delta AGB$	$\Delta\gamma^0$	3	29.2	26.1	36.8	2.3	19.9
$\Delta AGB$	$\Delta\gamma^0$	4	29.4	26.1	37.8	2.4	19.9
$\Delta AGB$	$\Delta\gamma_{dB}^0$	1	32.7	31.5	34.3	0.8	24.8
$\Delta\ln(AGB)$	$\Delta\gamma_{dB}^0$	4	87.0	38.0	171.0	47.8	73.8
$\Delta\ln(AGB)$	$\Delta\gamma_{dB}^0$	3	95.6	38.0	208.0	62.3	65.7
$\Delta\ln(AGB)$	$\Delta\gamma_{dB}^0$	1	123.4	55.6	292.1	76.0	235.4
$\Delta\ln(AGB)$	$\Delta\gamma_{dB}^0$	2	129.1	53.5	339.1	88.8	260.3

Pixel-RMSD and Stand-RMSD are averages over all combinations of training and evaluation pairs. Columns 5–7 give the minimum, maximum, and standard deviation of the pixel level RMSDs from all combinations. The models which are highlighted were also evaluated by comparison to field measured AGB change. Definitions of the AGB and  $\gamma^0$  change measures are given in Equations 9–14.

**Table 5.** Validation accuracy of cross-validated P-band models trained and evaluated on different image pairs.

AGB change measure	$\gamma^0$ change measure	Number of variables	Pixel-RMSD [t/ha]	Pixel-RMSD min [t/ha]	Pixel-RMSD max [t/ha]	Pixel-RMSD SD [t/ha]	Stand-RMSD [t/ha]
$\Delta\sqrt{AGB}$	$\Delta\gamma_{dB}^0$	4	25.6	25.2	26.1	0.3	19.1
$\Delta\sqrt{AGB}$	$\Delta\gamma_{dB}^0$	3	25.7	25.1	26.3	0.4	19.2
$\Delta\sqrt{AGB}$	$\Delta\gamma_{dB}^0$	2	25.7	25.1	26.4	0.5	19.4
$\Delta AGB$	$\Delta\gamma_{dB}^0$	4	29.0	28.7	29.6	0.3	19.8
$\Delta AGB$	$\Delta\gamma_{dB}^0$	2	29.3	28.9	29.8	0.3	20.0
$\Delta AGB$	$\Delta\gamma_{dB}^0$	3	29.6	29.2	30.0	0.2	19.9
$\Delta\sqrt{AGB}$	$\Delta\gamma_{dB}^0$	1	30.0	29.6	30.5	0.3	27.0
$\Delta\sqrt{AGB}$	$\Delta\gamma_A^0$	1	31.0	29.6	34.2	1.5	22.3
$\Delta AGB$	$\Delta\gamma^0$	4	31.8	28.2	38.1	2.9	22.7
$\Delta AGB$	$\Delta\gamma^0$	3	32.4	28.3	39.7	3.3	22.9
$\Delta AGB$	$\Delta\gamma_A^0$	1	35.0	34.1	35.8	0.5	23.5
$\Delta AGB$	$\Delta\gamma_{dB}^0$	1	35.3	35.1	35.6	0.1	26.5
$\Delta\ln(AGB)$	$\Delta\gamma_{dB}^0$	2	93.4	86.9	99.7	3.5	60.2
$\Delta\ln(AGB)$	$\Delta\gamma_{dB}^0$	4	110.2	106.2	112.8	1.8	70.7
$\Delta\ln(AGB)$	$\Delta\gamma_{dB}^0$	3	110.4	103.6	116.2	3.5	70.7
$\Delta\ln(AGB)$	$\Delta\gamma_{dB}^0$	1	146.3	118.9	183.2	18.2	224.8

Pixel-RMSD and Stand-RMSD are averages over all combinations of training and evaluation pairs. Columns 5–7 give the minimum, maximum, and standard deviation of the pixel level RMSDs from all combinations. The models which are highlighted were also evaluated by comparison to field measured AGB change. Definitions of the AGB and  $\gamma^0$  change measures are given in Equations 9–14.

adding a second explanatory variable, but further increasing the number of variables reduced the predictive performance, indicating overfitting. At P-band, each added explanatory variable decreased the RMSDs of these backscatter models (with AGB change modeled on the square root scale and backscatter change modeled on the logarithmic scale). However, RMSDs did not decrease more than 0.1 t/ha and 0.3 t/ha for the pixel and stand level, respectively, when more than two explanatory variables were added. Based on these results, the models highlighted in Tables 4 and 5 were selected to be evaluated through comparison

with the field measured AGB change in the ten 80 m × 80 m field plots.

In Table 6 (upper half), the mean biases as compared to the LiDAR-based AGB maps, standard deviation of biases, and  $p$  values for the selected models are shown. The  $p$  value indicates whether the variance in bias across pairs (i.e. when training a model on one image pair, and using the model to make predictions on another image pair) is significantly larger than in pairs. The models are identified by a letter indicating the band and a figure indicating the number of explanatory variables. In Table 6, it can be seen that the mean biases for

**Table 6.** Validation and prediction biases of selected models for L- and P-band (models with the lowest pixel level RMSD for a given number of variables).

Model	Across-pair mean bias [t/ha]	In-pair mean bias [t/ha]	Across-pair bias SD [t/ha]	In-pair bias SD [t/ha]	<i>p</i>
Bias as compared to LiDAR-based AGB maps					
L1	2.26	2.25	1.14	0.80	0.219
L2	2.19	2.18	0.81	0.63	0.300
P1	2.99	2.99	0.46	0.18	0.022
P2	2.81	2.81	0.38	0.11	0.006
P3	2.78	2.76	0.26	0.11	0.032
P4	2.61	2.68	0.47	0.16	0.012
Bias as compared to evaluation plots					
L1	-2.29	-2.23	4.78	5.49	0.716
L2	-1.75	-2.09	3.38	4.12	0.775
P1	1.90	1.90	0.99	0.60	0.130
P2	-0.15	-0.17	0.83	0.64	0.301
P3	-0.07	-0.13	0.84	0.88	0.622
P4	-0.31	-0.46	1.41	1.40	0.554

Across-pair values were calculated by training and evaluating on different image pairs, as in Tables 4 and 5, while in-pair values were calculated by training and evaluating on the same image pair.

L- and P-band were positive and less than 3 t/ha. Furthermore, the mean biases decreased with the number of explanatory variables. It is also worth noting that the mean biases were lower for the L-band models compared to P-band. The mean biases across pairs and in pairs differed by less than 0.1 t/ha for a given model. For P-band the variances in bias across pairs were significantly larger ( $p < 0.05$ ) than in pairs.

### Comparisons with field estimated AGB change

Details of the models with the best predictive performance with respect to the LiDAR-based AGB maps (RMSD) for both bands are given in Table 7, where in-pair and across-pair accuracies are presented. To also evaluate the predictive performance of the models and avoid the uncertainties related to using the LiDAR-based estimates, the predictions were compared with the field estimates, and listed as RMSE in Table 7.

The prediction accuracies (across-pair) from SAR (18.6–25.8 t/ha, Table 7) were similar to those from LiDAR (18.1 t/ha). The L-band model L2 (highest validation accuracy) had an RMSE of 20.8 t/ha, while the corresponding P-band model, P4, had an RMSE of 19.0 t/ha. Compared to the range of field measured AGB change in the ten evaluation plots, the RMSEs correspond to 6.3% and 5.7%, for L- and P-band, respectively. The chosen models indicate that HV was the polarization most sensitive to AGB changes, and HH- and VV-derived variables contributed only in P-band models with three or more explanatory variables, resulting in very small improvements to the RMSEs. However, the prediction accuracies across image pairs depend on the offset corrections, which cannot be performed with access only to the HV polarization.

The mean biases compared to the field measurements in the evaluation plots, standard deviation of biases and *p* values for the selected models are shown in Table 6 (lower half). Overall, the magnitude of the mean biases for L- and P-band were less than 2.3 t/ha. The lowest mean biases were achieved for the P-band models with more than one explanatory variable.

To compare the model prediction accuracies from different sensors and bands, the change predictions of the SAR models L2 and P4 and the LiDAR-based AGB maps for the large plots are shown in Figure 6 together with field measured AGB changes. There is no apparent overall band-related difference in the predictions, and neither a clear bias or a change in variance for the largest changes, originating from the clear-cut plots 9, 12, and 16.

Evaluation of the SAR-based predictions by comparison to the LiDAR-based AGB maps captures a more complete set of AGB change values than present in the field plots, despite the uncertainty of using LiDAR-based estimates as reference. Figure 7 shows the AGB change prediction maps of models L2 and P4 together with the LiDAR-based AGB change map. The SAR maps depict across-pair LOSO cross-validated predictions.

The training–prediction pairs used for Figure 7 are  $L_a - L_\beta$  and  $P_a - P_\beta$  for L- and P-band, respectively. These combinations represent worst cases in terms of backscatter offset, in that the 2007 acquisitions across the pairs have the largest time difference out of all combinations. Change maps based on other combinations are, however, similar. The predictions both with L- and P-band data overall capture the general trends in LiDAR predicted AGB change quite well, albeit with larger variance locally than the LiDAR-based change map.

**Table 7.** Attributes and accuracies of selected models for L- and P-band (models with the lowest pixel level RMSD for a given number of variables).

Model	AGB change measure	$\gamma^0$ change measure	Predictors	Across-pair pixel-RMSD [t/ha]	In-pair pixel-RMSD [t/ha]	Across-pair plot-RMSE [t/ha]	In-pair plot-RMSE [t/ha]
L1	$\Delta\sqrt{AGB}$	$\Delta\gamma_{dB}^0$	HV	26.3	26.3	25.8	25.7
L2	$\Delta\sqrt{AGB}$	$\Delta\gamma_{dB}^0$	HV + HV <sup>2</sup>	22.2	22.2	20.8	20.7
P1	$\Delta\sqrt{AGB}$	$\Delta\gamma_{dB}^0$	HV	30.0	30.0	26.4	26.4
P2	$\Delta\sqrt{AGB}$	$\Delta\gamma_{dB}^0$	HV + HV <sup>2</sup>	25.7	25.7	19.1	19.0
P3	$\Delta\sqrt{AGB}$	$\Delta\gamma_{dB}^0$	HH <sup>2</sup> + HV + HV <sup>2</sup>	25.7	25.7	18.6	18.5
P4	$\Delta\sqrt{AGB}$	$\Delta\gamma_{dB}^0$	HH <sup>2</sup> + HV + HV <sup>2</sup> + VV <sup>2</sup>	25.6	25.6	19.0	18.8

Across-pair pixel-RMSD and Across-pair plot-RMSE were calculated by training and evaluating on different image pairs, as in Tables 4 and 5, while In-pair pixel-RMSD and In-pair plot-RMSE were calculated by training and evaluating on the same image pair. All figures are averages over all valid image pair combinations.

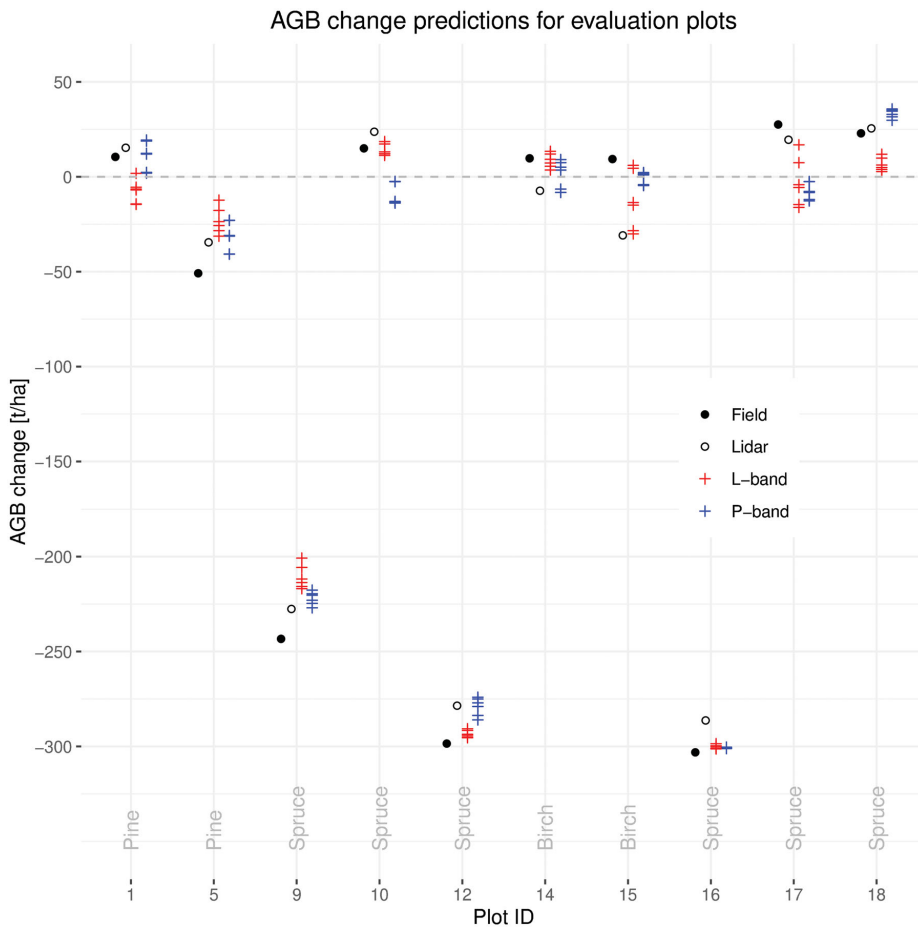


**Figure 6.** Field measured AGB change and predicted AGB change based on LiDAR, L-, and P-band SAR data. The SAR-based predictions are obtained using the models with the lowest RMSD on the pixel level, L2 and P4 in Table 7. For these models, one prediction per image pair is shown. The dominant tree species for each plot is reported above the plot ID.

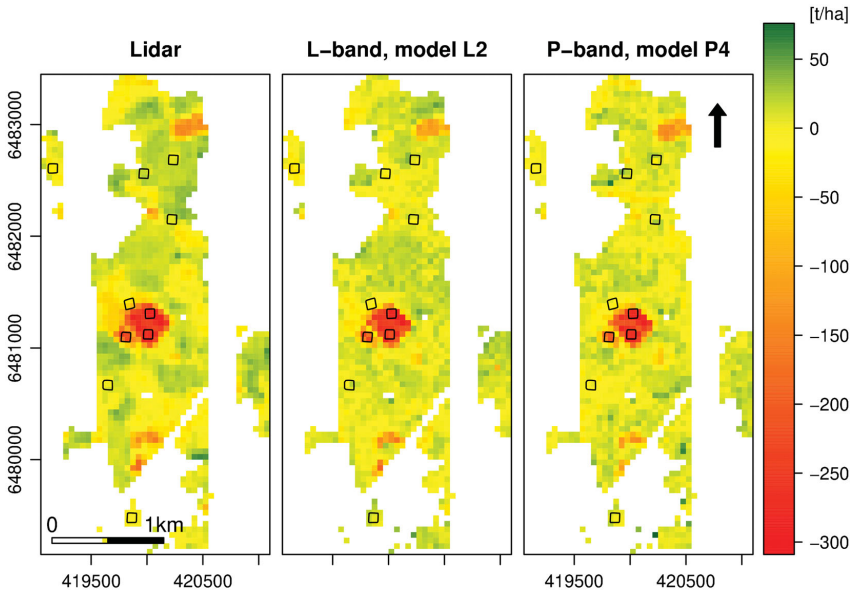


**Figure 7.** Biomass change maps, from left to right, based on LiDAR, L-, and P-band SAR data. The SAR-based predictions were obtained using the models with the lowest RMSD on the pixel level, L2 and P4 in Table 7. The black squares show the locations of the evaluation plots. The axes are labeled in meters, in UTM zone 33 N, datum WGS84 projection.

The predictions were temporally robust, with differences in RMSD between in-pair and across-pair predictions within 0.1 t/ha (Table 7). Correspondingly, a similar robustness was apparent for the RMSEs, which were calculated from the predictions on the field evaluation plots (Table 7). The differences in RMSE were within 0.1 t/ha for L-band, and within 0.2 t/ha for P-band. Moreover, the mean biases (Table 6) across pairs and in pairs differed by less than 0.4 t/ha for a given model. The variances in bias across pairs were not significantly larger ( $p > 0.05$ ) than in pairs.

## Discussion

The relatively long wavelength of the radar systems used in this study is a strength when estimating forest biomass via SAR backscatter, due to long wavelengths penetrating deeper into the forest canopy and being sensitive to forest elements down to the order of a wavelength. Consequently, because the wavelength is on the order of decimeters for L-band, compared to meters for P-band, we may further expect L-band backscatter to be less sensitive to biomass than P-band backscatter. However, the results of this study did not show a large difference in performance between the two bands for predicting hemi-boreal forest AGB change. Instead, the predictions with L-band

data achieved RMSD and mean bias values slightly lower, but close to those with P-band data, when compared to the LiDAR-based AGB maps. Yet, when compared to direct change measurements on field plots, the roles were reversed, and the predictions at L-band were slightly worse than at P-band, but still achieving RMSEs close to those of the LiDAR-based AGB maps used for estimating the parameters of the models.

The discrepancies between model predictions on the LiDAR-based AGB maps and the evaluation plots illustrate a limitation of the study in comparing the performance of the bands. As the parameters of the SAR models were estimated on LiDAR-based AGB maps, and the models achieve accuracies close to the accuracy of the training data, it may be that their performance is limited by the quality of the LiDAR-based AGB maps. The prediction accuracy achieved using SAR data is generally not better than when using LiDAR data for AGB or AGB change modeling, but as the SAR data used in the study are high resolution airborne acquisitions, the two data sources might be close to each other in information content. Higher accuracies for the SAR models would possibly have been achieved if field measurements of AGB change could have been used to train the models. However, one must often rely on LiDAR-based predictions due

to the lack of field plot inventory for large-area mapping.

The change prediction results presented in Figure 6 show no decrease in accuracy even for the largest changes of around 300 t/ha. This contradicts the saturation effect noted in earlier studies of biomass state prediction (Dobson et al. 1992; Rignot et al. 1994; Imhoff 1995; Fransson 1999), which indicates that it could be difficult to measure changes below about 100 or 200 t/ha. This result should be further evaluated on other data sets. However, some previous studies have indicated that the saturation for high biomass was not caused by the high biomass itself, but from different structural changes in the forest as the biomass increases, with some of them increasing the backscatter, and others decreasing it (Smith-Jonforsen et al. 2007; Joshi et al. 2017). Another important reason for saturation is due to ground topography (Soja et al. 2013), which is relatively modest at the Remningstorp test site and thus increases the point of saturation. As almost all pixels with a biomass change below 100 t/ha in the test site are from a handful of stands, the fact that the models can capture unexpectedly large changes may be due to the specific structure of the stands or area in question.

The offset correction and change prediction results were obtained in a hemi-boreal forest that is relatively flat in topography, and while the results are promising, they may not generalize to forests growing on more undulating terrain in the boreal region. This type of forest is relatively sparse, and a non-negligible ground contribution is expected to disturb the signal more with increasing topography. Insights could also be gained from comparing the performance of the offset correction methods for different tree species. While the correction methods may not be suitable for other forest types, studies evaluating the offset correction methods in temperate and tropical forests could give further insights about the underlying processes. In high biomass tropical forests, it is possible that the HV/VV-based correction could be better suited for also correcting P-band data, as the SAR signal does not penetrate as far into the dense canopy, making the interaction more like that of L-band scattering in less dense forests. For this test site, the P-band HV/VV ratio showed a slight offset in backscatter, but has some dependence on biomass change (Figure 3), and could therefore give a reasonable offset correction for P-band.

The most important contribution of this study was the development of a backscatter offset method for L-band data, which facilitated the prediction of biomass

change between images acquired in different moisture conditions or with radiometric calibration differences between them. Specifically, the proposed correction enabled predictions across image pairs with similar accuracies as those obtained within an image pair. An important finding was that a correction based on the HH/VV polarization ratio, as previously developed for P-band data, was not suitable for L-band in the same forest and environmental conditions. Instead, it was found that for the L-band data, the HV/VV ratio had the qualities needed for detecting low change areas, and the offset correction method developed was based on this ratio. The offset corrections made predictions across image pairs almost as good as those within each pair. Yet, the remaining variance in predictions on the evaluation plots from different image pairs indicate a more complex relationship between moisture and backscatter intensity than that of a simple offset. Understanding these relationships considering the underlying backscatter mechanisms might enable even better correction methods and more precise SAR-based AGB change predictions. The correction methods developed and applied in this study remove an offset due to moisture or calibration error that is constant over the whole scene, but cannot remove local variations.

## Conclusions

We have evaluated the performance of a method for predicting AGB change from changes in P- and L-band SAR backscatter data in hemi-boreal forests. An important element of the method is a backscatter-offset correction, which is based on a polarization ratio and does not require any reference ground data. By training regression models for each band on AGB maps created from field surveys and LiDAR data, we showed that both L- and P-band backscatter could predict AGB changes with errors close to those of the LiDAR-based AGB maps used for training the models. The prediction accuracies of L- and P-band models differed only slightly, although this result may have been due to limitations of the LiDAR-based AGB maps used to train the models.

The P-band results were in line with earlier studies, verifying the results of Sandberg et al. (2014). The method and evaluation for L-band presented in this paper is new and the results show almost the same prediction errors as for P-band. Furthermore, it was empirically found that the HH/VV-based backscatter-offset correction used for P-band was not suitable for correcting L-band data, and instead an HV/VV-based



correction performed better. The reason for this is yet to be fully understood, but as P-band SAR is known to interact more strongly with the ground and stems of the forest, while L-band SAR backscatter is mainly from the upper parts of the canopy (Tebaldini and Rocca 2012), it is possible that the HH/VV-based correction mainly corrects for ground moisture and that L-band data instead need to be corrected for canopy moisture.

The proposed backscatter offset correction method for L-band data was shown to facilitate prediction results across different image pairs almost identical to those obtained when training and predicting on the same image pair. Finally, while the HV/VV-based offset correction worked well for the L-band data in this data set, more studies are needed to see if this generalizes to other data sets and regions. Provided that it does, and that future L-band SAR missions provide HV and VV data, the method can alleviate and improve the mapping of AGB change using L-band SAR data. The findings suggest a potential for large-area mapping of forest biomass change using, e.g. the upcoming satellite SAR missions ALOS-4 and NISAR (L-band), and BIOMASS (P-band), despite varying environmental conditions and calibration uncertainties.

## Acknowledgments

The authors would like to thank DLR and ONERA for acquisition and processing of the SAR images. Additionally, we would like to thank the anonymous reviewers for the help in improving the quality and the overall readability of this paper.




## Disclosure statement



No conflict of interest was reported by the author(s). The funding sponsors had no role in the design of the study; in the collection, analyses, or interpretation of data; in the writing of the manuscript, or in the decision to publish the results.

## Funding

This research was funded by the Swedish National Space Agency grants [147/14] and [300/16], and Hildur and Sven Wingquist's Foundation for Forest Research. The BioSAR campaigns were funded by ESA.

## ORCID

Ivan Huuva  <http://orcid.org/0000-0002-8664-4872>  
Henrik J. Persson  <http://orcid.org/0000-0002-3403-057X>  
Maciej J. Soja  <http://orcid.org/0000-0002-4683-3142>

Jörgen Wallerman  <http://orcid.org/0000-0002-9996-1447>  
Lars M. H. Ulander  <http://orcid.org/0000-0001-5757-9517>

Johan E. S. Fransson  <http://orcid.org/0000-0002-7913-8592>

## References

- The CEOS database: Missions, instruments, measurements and datasets, 2020. <http://database.eohandbook.com/>.
- Ahlberg, O., and Kardell, L. 1997. *Remningstorp: Från herresäte till skogslaboratorium*. Skara: Hildur och Sven Wingquists stiftelse för skogsvetenskaplig forskning.
- Balzer, H., Skinner, L., Luckman, A., and Brooke, R. 2003. "Estimation of tree growth in a conifer plantation over 19 years from multi-satellite L-band SAR." *Remote Sensing of Environment*, Vol. 84(No. 2): 184–191.
- Canadell, J.G., Le Quéré, C., Raupach, M.R., Field, C.B., Buitenhuis, E.T., Ciais, P., Conway, T.J., Gillett, N.P., Houghton, R.A., and Marland, G. 2007. "Contributions to accelerating atmospheric CO<sub>2</sub> growth from economic activity, carbon intensity, and efficiency of natural sinks." *Proceedings of the National Academy of Sciences of the United States of America*, Vol. 104(No. 47): 18866–18870.
- Carreiras, J.M.B., Quegan, S., Le Toan, T., Ho Tong Minh, D., Saatchi, S.S., Carvalhais, N., Reichstein, M., and Scipal, K. 2017. "Coverage of high biomass forests by the ESA BIOMASS mission under defense restrictions." *Remote Sensing of Environment*, Vol. 196: 154–162.
- Cartus, O., Santoro, M., Wegmüller, U., and Rommen, B. 2019. "Benchmarking the retrieval of biomass in boreal forests using P-band SAR backscatter with multi-temporal C- and L-band observations." *Remote Sensing*, Vol. 11(No. 14): 1–20.
- Dobson, M.C., Ulaby, F.T., Le Toan, T., Beaudoin, A., Kasischke, E.S., and Christensen, N. 1992. "Dependence of radar backscatter on coniferous forest biomass." *IEEE Transactions on Geoscience and Remote Sensing*, Vol. 30(No. 2): 412–415.
- Fransson, J.E.S. 1999. "Estimation of stem volume in boreal forests using ERS-1 C- and JERS-1L-band SAR data." *International Journal of Remote Sensing*, Vol. 20(No. 1): 123–137.
- Fransson, J.E.S., Magnusson, M., Olsson, H., Eriksson, L.E.B., Sandberg, G., Smith-Jonforsen, G., and Ulander, L.M.H. 2007. "Detection of forest changes using ALOS PALSAR satellite images." In Proceedings of IGARSS 2007, Barcelona, Spain, 23–27 July, 2007, 2330–2333.
- Gregoire, T.G., Lin, Q.F., and Boudreau, J.N.R. 2008. "Regression estimation following the square-root transformation of the response." *Forest Science*, Vol. 54(No. 6): 597–606.
- Hajnsek, I., Scheiber, R., Ulander, L.M.H., Gustavsson, A., Sandberg, G., Tebaldini, S., Guarnieri, A.M., Rocca, F., Bombardini, F., and Pardini, M. 2008. *BioSAR 2007, Technical Assistance for the Development of Airborne SAR and Geophysical Measurements during the BioSAR 2007 Experiment: Final Report without Synthesis*. ESA Contract No.: 20755/07/NL/CB. European Space Agency.

- Hamadi, A., Villard, L., Borderies, P., Albinet, C., Koleck, T., and Le Toan, T. 2017. "Comparative analysis of temporal decorrelation at P-band and low L-band frequencies using a tower-based scatterometer over a tropical forest." *IEEE Geoscience and Remote Sensing Letters*, Vol. 14(No. 11): 1918–1922.
- Ho Tong Minh, D., Le Toan, T., Rocca, F., Tebaldini, S., Villard, L., Réjou-Méchain, M., Phillips, O.L., et al. 2016. "SAR tomography for the retrieval of forest biomass and height: Cross-validation at two tropical forest sites in French Guiana." *Remote Sensing of Environment*, Vol. 175: 138–147.
- Huuvu, I., Fransson, J.E.S., Persson, H.J., Wallerman, J., Ulander, L.M.H., Blomberg, E., and Soja, M.J. 2017. "Measurements of forest biomass change using L- and P-band SAR backscatter." In Proceedings of IGARSS 2017, Fort Worth, Texas, USA, 23–28 July, 2017, 5818–5821.
- Imhoff, M.L. 1995. "Radar backscatter and biomass saturation: Ramification for global biomass inventory." *IEEE Transactions on Geoscience and Remote Sensing*, Vol. 33(No. 2): 511–518.
- Joshi, N., Mitchard, E.T.A., Broly, M., Schumacher, J., Fernández-Landa, A., Johannsen, V.K., Marchamalo, M., and Fensholt, R. 2017. "Understanding 'saturation' of radar signals over forests." *Scientific Reports*, Vol. 7(No. 3505): 1–11.
- Kasischke, E.S., Melack, J.M., and Dobson, M.C. 1997. "The use of imaging radars for ecological applications—A review." *Remote Sensing of Environment*, Vol. 59(No. 2): 141–156.
- Kasischke, E.S., Tanase, M.A., Bourgeau-Chavez, L.L., and Borr, M. 2011. "Soil moisture limitations on monitoring boreal forest regrowth using spaceborne L-band SAR data." *Remote Sensing of Environment*, Vol. 115(No. 1): 227–232.
- Kurvonen, L., Pulliainen, J., and Hallikainen, M. 1999. "Retrieval of biomass in boreal forests from multitemporal ERS-1 and JERS-1 SAR images." *IEEE Transactions on Geoscience and Remote Sensing*, Vol. 37(No. 1): 198–205.
- Lämäs, T., and Eriksson, L.O. 2003. "Analysis and planning systems for multiresource, sustainable forestry: The Heureka Research Programme at SLU." *Canadian Journal of Forest Research*, Vol. 33(No. 3): 500–508.
- Le Rest, K., Pinaud, D., Monestiez, P., Chadoeuf, J., and Bretagnolle, V. 2014. "Spatial leave-one-out cross-validation for variable selection in the presence of spatial autocorrelation." *Global Ecology and Biogeography*, Vol. 23(No. 7): 811–820.
- Le Toan, T., Beaudoin, A., Riou, J., and Guyon, D. 1992. "Relating forest biomass to SAR data." *IEEE Transactions on Geoscience and Remote Sensing*, Vol. 30(No. 2): 403–411.
- Lucas, R., Armston, J., Fairfax, R., Fensham, R., Accad, A., Carreiras, J., Kelley, J., et al. 2010. "An evaluation of the ALOS PALSAR L-band backscatter—above ground biomass relationship Queensland, Australia: Impacts of surface moisture condition and vegetation structure." *IEEE Journal of Selected Topics in Applied Earth Observations and Remote Sensing*, Vol. 3(No. 4): 576–593.
- Marklund, L.G. 1988. *Biomass Functions for Pine, Spruce and Birch in Sweden*. Umeå: Swedish University of Agricultural Sciences.
- Monteith, A.R., and Ulander, L.M.H. 2018. "Temporal survey of P- and L-band polarimetric backscatter in boreal forests." *IEEE Journal of Selected Topics in Applied Earth Observations and Remote Sensing*, Vol. 11(No. 10): 3564–3577.
- Neumann, M., Saatchi, S.S., Ulander, L.M.H., and Fransson, J.E.S. 2012. "Assessing performance of L- and P-band polarimetric interferometric SAR data in estimating boreal forest above-ground biomass." *IEEE Transactions on Geoscience and Remote Sensing*, Vol. 50(No. 3): 714–726.
- Persson, H.J., and Fransson, J.E.S. 2017. "Comparison between TanDEM-X- and ALS-based estimation of aboveground biomass and tree height in boreal forests." *Scandinavian Journal of Forest Research*, Vol. 32(No. 4): 306–319.
- Pettersson, H., Holm, S., Ståhl, G., Alger, D., Fridman, J., Lehtonen, A., Lundström, A., and Mäkipää, R. 2012. "Individual tree biomass equations or biomass expansion factors for assessment of carbon stock changes in living biomass—A comparative study." *Forest Ecology and Management*, Vol. 270: 78–84.
- Rauste, Y. 2005. "Multi-temporal JERS SAR data in boreal forest biomass mapping." *Remote Sensing of Environment*, Vol. 97(No. 2): 263–275.
- Rignot, E., Way, J., Williams, C., and Viereck, L. 1994. "Radar estimates of aboveground biomass in boreal forests of interior Alaska." *IEEE Transactions on Geoscience and Remote Sensing*, Vol. 32(No. 5): 1117–1124.
- Saatchi, S.S., and Moghaddam, M. 2000. "Estimation of crown and stem water content and biomass of boreal forest using polarimetric SAR imagery." *IEEE Transactions on Geoscience and Remote Sensing*, Vol. 38(No. 2): 697–709.
- Sandberg, G., Ulander, L.M.H., Fransson, J.E.S., Holmgren, J., and Le Toan, T. 2011. "L- and P-band backscatter intensity for biomass retrieval in hemiboreal forest." *Remote Sensing of Environment*, Vol. 115(No. 11): 2874–2886.
- Sandberg, G., Ulander, L.M.H., Wallerman, J., and Fransson, J.E.S. 2014. "Measurements of forest biomass change using P-band SAR backscatter." *IEEE Transactions on Geoscience and Remote Sensing*, Vol. 52(No. 10): 6047–6061.
- Santoro, M., Cartus, O., Fransson, J.E.S., and Wegmüller, U. 2019. "Complementarity of X-, C-, and L-band SAR backscatter observations to retrieve forest stem volume in boreal forest." *Remote Sensing*, Vol. 11(No. 13): 1–25.
- Santoro, M., Eriksson, L.E.B., and Fransson, J.E.S. 2015. "Reviewing ALOS PALSAR backscatter observations for stem volume retrieval in Swedish forest." *Remote Sensing*, Vol. 7(No. 4): 4290–4317.
- Santoro, M., Pantze, A., Fransson, J.E.S., Dahlgren, J., and Persson, A. 2012. "Nation-wide clear-cut mapping in Sweden using ALOS PALSAR strip images." *Remote Sensing*, Vol. 4(No. 6): 1693–1715.
- Schlund, M., and Davidson, M.W.J. 2018. "Aboveground forest biomass estimation combining L- and P-band SAR acquisitions." *Remote Sensing*, Vol. 10(No. 7): 1–23.

- Smith-Jonforsen, G., Folkesson, K., Hallberg, B., and Ulander, L.M.H. 2007. "Effects of forest biomass and stand consolidation on P-band backscatter." *IEEE Geoscience and Remote Sensing Letters*, Vol. 4(No. 4): 669–673.
- Snowdon, P. 1991. "A ratio estimator for bias correction in logarithmic regressions." *Canadian Journal of Forest Research*, Vol. 21(No. 5): 720–724.
- Söderberg, U. 1986. *Functions for Forecasting of Timber Yields: Increment and Form Height for Individual Trees of Native Species in Sweden*. Umeå: Swedish University of Agricultural Sciences.
- Soja, M.J., Sandberg, G., and Ulander, L.M.H. 2013. "Regression-based retrieval of boreal forest biomass in sloping terrain using P-band SAR backscatter intensity data." *IEEE Transactions on Geoscience and Remote Sensing*, Vol. 51(No. 5): 2646–2665.
- Solberg, S., Naesset, E., Gobakken, T., and Bollandsås, O.-M. 2014. "Forest biomass change estimated from height change in interferometric SAR height models." *Carbon Balance Manag.*, Vol. 9(No. 5): 1–12.
- Stocker, T.F., Qin, D., Plattner, G.-K., Tignor, M.M.B., Allen, S.K., Boschung, J., Nauels, A., Xia, Y., Bex, V., and Midgley, P.M. 2013. *Climate Change 2013: The Physical Science Basis. Intergovernmental Panel on Climate Change*. Cambridge, UK; New York, NY: Cambridge University Press.
- Tebaldini, S., and Rocca, F. 2012. "Multibaseline polarimetric SAR tomography of a boreal forest at P- and L-bands." *IEEE Transactions on Geoscience and Remote Sensing*, Vol. 50(No. 1): 232–246.
- Ulaby, F.T., Moore, R.K., and Fung, A.K. 1982. *Microwave Remote Sensing: Active and Passive. Volume II. Radar Remote Sensing and Surface Scattering and Emission Theory*, Reading, Massachusetts: Addison-Wesley.
- Ulander, L.M.H. 1996. "Radiometric slope correction of synthetic-aperture radar images." *IEEE Transactions on Geoscience and Remote Sensing*, Vol. 34(No. 5): 1115–1122.
- Ulander, L.M.H., Gustavsson, A., Flood, B., Murdin, D., Dubois-Fernandez, P., Dupuis, X., Sandberg, G., et al. 2011. *BioSAR 2010, Technical Assistance for the Development of Airborne SAR and Geophysical Measurements during the BioSAR 2010 Experiment: Final Report*. ESA Contract No.: 4000102285/10/NL/JA/ef. European Space Agency.
- Wikström, P., Edenius, L., Elfving, B., Eriksson, L.O., Lämås, T., Sonesson, J., Öhman, K., Wallerman, J., Waller, C., and Klintebäck, F. 2011. "The Heureka forestry decision support system: An overview." *Mathematical and Computational Forestry & Natural-Resource Sciences (MCFNS)*, Vol. 3(No. 2): 87–94.





# PREDICTION OF HEMI-BOREAL FOREST BIOMASS CHANGE USING ALOS-2 PALSAR-2 L-BAND SAR BACKSCATTER

Ivan Huuva<sup>1</sup>, Henrik J. Persson<sup>1</sup>, Jörgen Wallerman<sup>1</sup>, Lars M.H. Ulander<sup>2</sup>, Johan E.S. Fransson<sup>3</sup>

<sup>1</sup>Swedish University of Agricultural Sciences, Department of Forest Resource Management, Umeå, Sweden

<sup>2</sup>Chalmers University of Technology, Department of Space, Earth and Environment, Göteborg, Sweden

<sup>3</sup>Linnaeus University, Department of Forestry and Wood Technology, Växjö, Sweden

## ABSTRACT

Pairs of fully polarimetric ALOS-2 PALSAR-2 L-band SAR images were used to model biomass on backscatter change over seven growth seasons in a hemi-boreal forest. The biomass change was related to backscatter change via consecutive field surveys of 263 field plots with a 10 m radius. To correct for differences in backscatter not related to biomass abundance, a HV-VV polarization ratio based correction, previously used on airborne L-band data, was applied to the data. The uncertainty of obtained predictions (lowest model mean RMSE 65.1 t/ha, lowest model mean bias 7.1 t/ha) was almost identical whether model fitting and prediction used data from the same scene pair, or different scene pairs. This could possibly attest to the feasibility of the backscatter correction for PALSAR-2 data, but no large backscatter offsets were observed for uncorrected data, and significant variance in predictions, due to the inherent noise in the data and the comparatively small area of evaluation plots, inhibit the analysis.

**Index Terms**— SAR, backscatter, biomass change, ALOS-2 PALSAR-2, forestry

## 1. INTRODUCTION

The Synthetic Aperture Radar (SAR) backscatter intensity of longer wavelengths is correlated with forest biomass up to a wavelength dependent saturation threshold [1]. Previous studies have successfully predicted both biomass and biomass change by exploiting this correlation [2–13]. However, backscatter intensity is not sensitive only to biomass abundance, but also environmental factors, a crucial one being soil and canopy moisture, which varies considerably between not only seasons, but also between days. Thus, when relating changes in backscatter to changes in biomass, one has to control for these variations. This has been done successfully in hemi-boreal forests using both P- and L-band SAR backscatter, utilizing polarization ratios to correct for non-biomass related variations in backscatter intensity [14, 15]. These studies reported root mean square

errors (RMSEs) of 19 t/ha and 21 t/ha for biomass change predictions using L- and P-band models, respectively. However, these previous studies utilized data from airborne SAR systems. In this study, biomass change over seven growth seasons between 2015 and 2022 was predicted using regression models relating the biomass change to L-band SAR data from the spaceborne ALOS-2 PALSAR-2 sensor, using the HV-VV backscatter ratio to correct the backscatter intensity, as was previously done for airborne BioSAR L-band data in [14].

## 2. MATERIAL AND METHODS

Remningstorp is a hemi-boreal forest test site in southern Sweden (Lat. 58°30' N, Long. 13°40' E). The site consists of 1,200 ha of productive, commercially managed forest. The main species in Remningstorp are Norway spruce (*Picea abies* (L.) H. Karst.), Scots pine (*Pinus sylvestris* L.), and birch (*Betula* spp.). The soil type is mainly till with a field layer of different herbs, blueberry (*Vaccinium myrtillus* L.), and narrow leaved grass (e.g. *Deschampsia flexuosa* (L.) Trin.). The field layer is absent in denser old spruce stands. The site is relatively flat, with an elevation that varies between 120 m and 145 m above sea level. The estate is managed by the Forestry Society's Estate Management Company (Skogssällskapet). A thorough description of the property has been published in [15].

### 2.1. Field data

A systematic grid of 263 field plots with a 10 m radius and a 200 m spacing were surveyed in 2014-2015, and resurveyed after the growth period of 2021. All trees with a diameter at breast height (DBH, measured at 1.3 m above ground) of more than 4 cm were calipered, species determined, and positioned using a real time kinematic global positioning system. The height was measured on a subsample of trees, randomly sampled with probability proportional to the basal area, using a hypsometer. Above ground biomass (AGB) was estimated using the Heureka system [17], which applied established models for AGB by Marklund [18].

## 2.2. SAR data and processing

The study used ALOS-2 PALSAR-2 fully polarimetric high-sensitive mode data in strip map format. The acquisitions were chosen to match the field surveys as well as possible, while also avoiding winter dates, when negative temperatures and potential snow cover can severely affect the backscatter.

In addition, to avoid changes in backscatter due to acquisition geometry, the acquisitions were chosen from the same track and with the same ascending orbital direction. Three such acquisitions before, and two acquisitions after the growth periods between the field surveys were chosen as they met the requirements (Table 1).

**Table 1.** ALOS-2 PALSAR-2 scenes used in the study.

Scene ID	Observation mode	Observation direction	Processing level	Orbit direction	Observation time
ALOS2056751170-150611	HBQ	Right-looking	1.1	Ascending	22:37
ALOS2379671170-210603	HBQ	Right-looking	1.1	Ascending	22:37
ALOS2054681170-150528	HBQ	Right-looking	1.1	Ascending	22:37
ALOS2052611170-150514	HBQ	Right-looking	1.1	Ascending	22:37
ALOS2342411170-200924	HBQ	Right-looking	1.1	Ascending	22:37

The data were delivered in slant range geometry in Single Look Complex (SLC) format. Using an airborne laser scanning derived digital terrain model (DTM), the scenes were radiometrically and geometrically corrected with respect to incidence angle and ground slope and projected to ground range to produce radiometrically corrected backscatter,  $\gamma^0$ , henceforth just called backscatter [14,15]. All possible pairs of scenes containing one scene from each of the years, altogether six pairs, were defined. Following the procedure in [15], each of these pairs were backscatter offset corrected so that pixels with a change smaller than 2 dB in the HV-VV ratio between the two scenes get the same mean backscatter. The correction was applied to each polarization separately. After the correction, the mean backscatter in each field plot (10 m in radius) was extracted by weighing each pixel value by the fraction of the pixel area contained in the circular plot area.

between AGB change and backscatter change, while still keeping the models fairly simple.

In a first model selection step, offset corrected backscatter change data from all scene pairs and field plots were pooled to select candidate models from all possible ones defined by Equation (1). In this process, adjusted  $R^2$  was used to select candidate models for each number of variable. Since these measures cannot be compared for models with different dependent variable scales, the  $R^2$  were used to compare only models with the same AGB-scale.

The AGB change predictions of the selected models were evaluated in a twofold cross-validation procedure, designed to also evaluate the effectiveness of the backscatter offset correction by fitting and predicting *across-pairs*, i.e. fitting model parameters on data from one pair and predicting using data from another pair. These predictions were then compared to fitting and predicting *in-pair*, i.e. fitting model parameters and predicting using data from the same pair of scenes. In both cases, leave-one-out cross-validation (LOO-CV) was applied to the field plots, so that predictions on a plot were always done using model parameters fitted to data from the remaining field plots. The predictions were evaluated by calculating RMSE averages over all such combinations, and their standard deviations (SD), for each evaluated model. Biases were similarly calculated for each combination and averaged for each model.

## 2.3. Biomass change prediction

Using the difference in mean backscatter for a plot between the two scenes in a pair, biomass change was modelled using multivariate linear regression models of the general form

$$y = b_0 + b_1x_{HV} + b_2x_{HV}^2 + b_3x_{HH} + b_4x_{HH}^2 + b_5x_{VV} + b_6x_{VV}^2 + \epsilon, \quad (1)$$

where  $y$  is the AGB change,  $x_{ij}$  are backscatter change for a given polarization  $ij$ , and  $b$  denotes the regression coefficient to be estimated. The AGB was modelled on either linear (untransformed), square root, or logarithmic scale, and  $\gamma^0$  was modelled on square root, linear (untransformed, power), or dB scale. The decibel scale is simply a logarithmic transformation, but was specifically chosen to comply with radar conventions. Different transformations of either AGB of  $\gamma^0$  were not used in the same model, except as allowed by the second power terms in Equation (1). The transformations were an attempt to empirically determine a sufficiently expressive model to capture the non-linear relationship

## 3. RESULTS

The results of the cross-validation procedure for selected models are presented in Table 2. Overall, the predictions were very similar whether model parameter fitting and prediction were performed using data from the same pair of SAR scenes or from different ones.

Based only on RMSE values, models using the change in AGB on a square root scale and the change in  $\gamma^0$  on a logarithmic (dB) scale performed the best, with a five parameter model (four coefficients and an intercept) achieving an RMSE of 65.1 t/ha. Compared to the largest field measured AGB change, the RMSEs corresponds to

18 %. On the other hand, models using the AGB change modelled linearly, still using change on a dB scale, had very similar RMSE, 68.7 t/ha (19 %) at best, while having smaller

biases around 8 t/ha, about half the biases of the models with AGB change on a square root scale.

**Table 2.** Summary cross-validation statistics of biomass change prediction models. Columns 4, 6, and 8 are the evaluation results when model parameter estimation and prediction were done on separate image pairs, while columns 5, 7, and 9 are results from fitting and predicting on data from the same image pairs. Each RMSE and bias figure is an average over all such combinations of training and evaluation pairs. The SD of RMSEs are also computed over all such combinations.

AGB change measure	$\gamma^0$ change measure	Number of variables	Across-pair RMSE [t/ha]	In-pair RMSE [t/ha]	Across-pair SD of RMSE [t/ha]	In-pair SD of RMSE [t/ha]	Across-pair bias [t/ha]	In-pair Bias [t/ha]
$\Delta\sqrt{AGB}$	$\Delta\gamma_{dB}^0$	4	65.1	65.0	1.6	1.3	16.6	16.6
$\Delta\sqrt{AGB}$	$\Delta\gamma_{dB}^0$	3	65.9	65.7	1.7	1.6	17.0	16.9
$\Delta\sqrt{AGB}$	$\Delta\gamma_{dB}^0$	2	66.1	66.2	1.4	1.5	17.2	17.3
$\Delta\sqrt{AGB}$	$\Delta\gamma_{dB}^0$	1	68.0	68.0	1.7	2.2	18.2	18.3
$\Delta AGB$	$\Delta\gamma_{dB}^0$	4	68.7	68.8	0.9	1.0	6.9	7.1
$\Delta AGB$	$\Delta\gamma_{dB}^0$	3	69.1	69.1	1.0	1.2	7.1	7.2
$\Delta AGB$	$\Delta\gamma_{dB}^0$	2	69.2	69.4	1.0	1.2	7.1	7.2
$\Delta AGB$	$\Delta\gamma_{dB}^0$	1	71.6	71.6	1.0	1.4	8.6	8.7
$\Delta \ln(AGB)$	$\Delta\sqrt{\gamma^0}$	4	87.2	87.4	0.6	1.1	11.1	11.2
$\Delta \ln(AGB)$	$\Delta\gamma_{dB}^0$	3	87.2	87.3	0.7	0.5	11.4	11.4
$\Delta \ln(AGB)$	$\Delta\gamma_{dB}^0$	4	87.2	87.2	0.7	0.4	11.4	11.4
$\Delta \ln(AGB)$	$\Delta\sqrt{\gamma^0}$	3	87.3	87.5	0.6	0.8	11.2	11.3
$\Delta \ln(AGB)$	$\Delta\sqrt{\gamma^0}$	1	87.4	87.3	1.4	0.5	11.4	11.3
$\Delta \ln(AGB)$	$\Delta\gamma_{dB}^0$	2	87.4	87.5	1.0	0.6	11.4	11.4
$\Delta \ln(AGB)$	$\Delta\gamma_{dB}^0$	1	87.5	87.5	1.0	0.6	11.4	11.4
$\Delta \ln(AGB)$	$\Delta\sqrt{\gamma^0}$	2	87.5	87.6	0.7	0.9	11.1	11.3

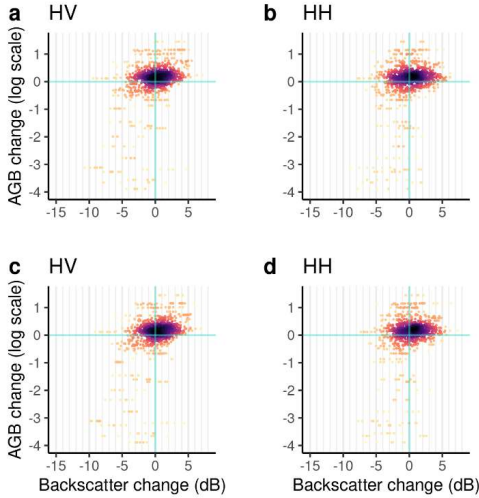


**Figure 1.** Bivariate plots of AGB change and  $\gamma^0$  change between all image pairs. **a** and **b** show uncorrected, while **c** and **d** show corrected data. VV-data were similar, but not shown due to page limitations.

Remaining models included in the cross-validation employed other combinations of change measures for AGB and  $\gamma^0$  and had higher RMSEs than the aforementioned model classes, with RMSEs of 87 t/ha and more, but with biases somewhere in between the two, around 11 t/ha. The most important polarization in best performing models was HV. All measures in the best performing one- and two variable models are based on HV. The best performing three variable models incorporate one variable based on HH, while one VV variable is included in both the best performing four variable models. Fig. 1 shows the change in AGB between the inventories plotted against the change in  $\gamma^0$  between all scene pairs. There is no clear overall offset in  $\gamma^0$  in any direction, and no clear difference in offset or decrease in variance for the corrected data.

#### 4. DISCUSSION AND CONCLUSIONS

While the obtained in-pair and across-pair AGB change predictions were almost identical in prediction performance, it is not clear that this could be attributed to the offset correction applied to the image pairs. Since the uncorrected pairs showed no general offsets in backscatter, there may not have been much need for correction. Much clearer offsets were observed over the same study area in [14,15] for both airborne L- and P-band data. The lack of clear offsets between the scenes is possibly due to similar weather and moisture conditions at the acquisition dates.



The RMSEs and biases reported in this study are significantly larger than those reported for L-band models based on airborne data in [15], but this is not only due to differences in quality between satellite and airborne SAR, but also due to much smaller evaluation areas. In [14], 80 m × 80 m plots, about 20 times larger than the 10 m radius plots in this study were used. Furthermore, the normalization procedure used to calculate relative RMSEs here was to relate the RMSE to the largest field measured AGB change. This is in contrast to relating it to the average, which is often used in the context of state predictions. The problem with using the average to normalize biomass change, is that the average change tends to be very close to zero, thereby inflating and making relative RMSEs extremely dependent on the field data set used. A solution could be to treat positive and negative changes separately in the evaluation process. To facilitate more conclusive comparisons, additional acquisition dates should be included if possible, and larger evaluation areas could decrease the variance in predictions.

## 5. ACKNOWLEDGEMENTS

The ALOS-2 PALSAR-2 strip map data were provided by JAXA EORC within the 3<sup>rd</sup> Research Announcement on the Earth Observations (PI: Johan Fransson, ER3A2N096). This project was funded by The Forestry Society's Estate Management Company (Skogssällskapet), 2021-923-Step 2 2020.

## 6. REFERENCES

- [1] E.S. Kasischke, J.M. Melack, and M.C. Dobson, "The use of imaging radars for ecological applications—A review," *Remote Sensing of Environment*, vol. 59, no. 2, pp. 141-156, 1997.
- [2] G. Sandberg, L.M.H. Ulander, J.E.S. Fransson, J. Holmgren, and T. Le Toan, "L- and P-band backscatter intensity for biomass retrieval in hemi-boreal forest", *Remote Sensing of Environment*, vol. 115, no. 11, pp. 2874-2886, 2011.
- [3] M. Neumann, S.S. Saatchi, L.M.H. Ulander, and J.E.S. Fransson, "Assessing performance of L- and P-band polarimetric interferometric SAR data in estimating boreal forest above-ground biomass", *IEEE Transactions on Geoscience and Remote Sensing*, vol. 50, no. 3, pp. 714-726, March 2012.
- [4] E. Rignot, J. Way, C. Williams, and L. Viereck, "Radar estimates of aboveground biomass in boreal forests of interior Alaska," *IEEE Transactions on Geoscience and Remote Sensing*, vol. 32, no. 5, 1117-1124, 1994.
- [5] L. Kurvonen, J. Pulliainen, and M. Hallikainen, "Retrieval of biomass in boreal forests from multitemporal ERS-1 and JERS-1 SAR images," *IEEE Transactions on Geoscience and Remote Sensing*, vol. 37, no. 1, 198-20, 1999.
- [6] S.S. Saatchi, and M. Moghaddam, "Estimation of crown and stem water content and biomass of boreal forest using polarimetric SAR imagery," *IEEE Transactions on Geoscience and Remote Sensing*, vol. 38, no. 2, 697-709, 2000.
- [7] Y. Rauste, "Multi-temporal JERS SAR data in boreal forest biomass mapping," *Remote Sensing of Environment*, vol. 97, no. 2, 263-275, 2005.
- [8] M. Neumann, S.S. Saatchi, L.M.H. Ulander, and J.E.S. Fransson, "Assessing performance of L- and P-band polarimetric interferometric SAR data in estimating boreal forest above-ground biomass," *IEEE Transactions on Geoscience and Remote Sensing*, vol. 50, no. 3, 714-726, 2012.
- [9] M. Santoro, L.E.B. Eriksson, and J.E.S. Fransson, "Reviewing ALOS PALSAR backscatter observations for stem volume retrieval in Swedish forest," *Remote Sensing*, vol. 7, no. 4, 4290-4317, 2015.
- [10] M. Schlund, and M.W.J. Davidson, "Aboveground forest biomass estimation combining L- and P-band SAR acquisitions," *Remote Sensing*, vol. 10, no. 7, 1-23, 2018.
- [11] O. Cartus, M. Santoro, U. Wegmüller, and B. Rommen, "Benchmarking the retrieval of biomass in boreal forests using P-band SAR backscatter with multi-temporal C- and L-band observations," *Remote Sensing*, vol. 11, no. 14, 1-20, 2019.
- [12] M. Santoro, O. Cartus, J.E.S. Fransson, and U. Wegmüller, "Complementarity of X-, C-, and L-band SAR backscatter observations to retrieve forest stem volume in boreal forest," *Remote Sensing*, vol. 11, no. 13, 1-25, 2019.
- [13] M. Hayashi, T. Motohka, and Y. Sawada, "Aboveground biomass mapping using ALOS-2/PALSAR-2 time-series images for Borneo's forest," *IEEE Journal of Selected Topics in Applied Earth Observations and Remote Sensing*, vol. 12, no. 12, pp. 5167-5177, 2019.
- [14] G. Sandberg, L.M.H. Ulander, J. Wallerman, and J.E.S. Fransson, "Measurements of forest biomass change using P-band SAR backscatter," *IEEE Transactions on Geoscience and Remote Sensing*, vol. 52, no. 10, pp. 6047-6061, Oct. 2014.
- [15] I. Huuva, H.J. Persson, M.J. Soja, J. Wallerman, L.M.H. Ulander and J.E.S. Fransson, "Predictions of biomass change in a hemi-boreal forest based on multi-polarization L- and P-band SAR backscatter," *Canadian Journal of Remote Sensing*, vol. 46, no. 6, pp. 661-680, 2020.
- [16] O. Ahlberg and L. Kardell, *Remningstorp: Fran herresäte till skogslaboratorium*, Västergötlands Tryckeri AB, Skara, Sweden, 1997.
- [17] P. Wikström, L. Edenius, B. Elfving, L.O. Eriksson, T. Lämås, J. Sonesson, K. Öhman, J. Wallerman, C. Waller, and F. Klinteback, "The Heureka forestry decision support system: An overview," *Mathematical and Computational Forestry & Natural-Resource Sciences*, vol. 3, no. 2, 87-94, 2011.
- [18] L.G. Marklund, *Biomassfunktioner for tall gran och björk i Sverige*, Swedish University of Agricultural Sciences, Umeå, Sweden, 1988.





# DETECTABILITY OF SILVICULTURAL TREATMENTS IN TIME SERIES OF PENETRATION DEPTH CORRECTED TANDEM-X PHASE HEIGHTS

*Ivan Huuva<sup>1</sup>, Henrik J. Persson<sup>1</sup>, Jörgen Wallerman<sup>1</sup>, Johan E.S. Fransson<sup>1,2</sup>*

<sup>1</sup> Swedish University of Agricultural Sciences, Department of Forest Resource Management, SE-901 83 Umeå, Sweden

<sup>2</sup> Linnaeus University, Department of Forestry and Wood Technology, SE-351 95 Växjö, Sweden

## ABSTRACT

This study investigated the potential of utilizing time series of TanDEM-X phase heights, corrected for penetration depth, to detect silvicultural treatments in hemi-boreal forest. In total, 34 field plots with 40 m radius were used in conjunction with detailed forest management records to construct a reliable data set of treatments. The study area is situated in Remningstorp, a forest test site in southern Sweden. In the analysis, the temporal mean corrected phase heights were compared before and after a silvicultural treatment in order to quantify the effects of thinnings and clear-cuts on the phase height. As expected clear-cuts were highly distinguishable, but thinnings, while exhibiting a negative change in phase height on average, were not individually distinct from all untreated plots. Moreover, the results regarding the utility of applying penetration depth correction for the task were inconclusive. Overall, the results look very promising for using time series of phase height from TanDEM-X to map thinnings and clear-cuts, especially when several observations are available before and after the silvicultural treatment.

**Index Terms**— TanDEM-X, forestry, change detection, time series, penetration depth, thinnings, clear-cuts

## 1. INTRODUCTION

Remote sensing using satellite synthetic aperture radar (SAR) enables frequent mapping of forest variables, since the SAR works even in darkness and poor visibility conditions with clouds, rain and fog. Free-of-charge data from satellite SAR with 5-10 m resolution have great possibility to become one of the most important data sources for semi- or automatic mapping of forest resources with the potential to revolutionize forest planning. Here, time series will play an important role to be used in order to map changes, i.e. thinnings, clear-cuts and growth, and being the basis for proposing appropriate silvicultural treatments. In this context, data could be used from several satellite systems using different wavelength bands and polarizations, e.g. TanDEM-X (X-band ~3 cm, DLR), Sentinel-1 (C-band ~6 cm, ESA),

ALOS-2 (L-band ~24 cm, JAXA), complementing each other by capturing information of the forest from the upper part of the canopy (short wavelength) and from the trunks and larger branches (long wavelength).

Recent research shows that tree height and density can be estimated with high accuracy based on interferometric satellite SAR (InSAR) using TanDEM-X data [1, 2]. In [3], above-ground biomass (AGB) and tree height were estimated with about the same accuracy from TanDEM-X and ALS data. Standwise tree height was estimated with root mean square errors (RMSEs) of 4.1% and 7.6% and AGB with 14.6% and 17.2% at the Swedish test sites Remningstorp and Krycklan, respectively. In [4], repeated backscatter observations from TerraSAR-X, Sentinel-1 and ALOS-2 from Remningstorp and Krycklan were analyzed, separately and in combination, and used to estimate stem volume based on the Water Cloud Model [5, 6]. The relationship between SAR backscatter and stem volume differed depending on forest structure and environmental conditions, in particular at X- and C-band. The highest estimation accuracy was obtained at L-band. The combination of stem volume estimates from data acquired at two or three frequencies achieved an accuracy that was superior to values using single frequency. When combining estimates from X-, C- and L-band data, the relative RMSE for 0.5 ha field plots at Remningstorp was ~30%. It was suggested to combine multiple frequencies to ensure the highest achievable accuracy. In [4], only stem volume was estimated using backscatter data from X-, C- and L-band, separately and in combination, but without any analysis of change. In [7, 8], biomass change algorithms were developed separately for L- and P-band airborne data. The best L- and P-band model achieved an RMSE of 21 t/ha and 19 t/ha, respectively (similar to the ALS-based biomass change of 18 t/ha). Earlier studies have used TanDEM-X data to detect thinnings and clear-cuts in hemi-boreal forests [9, 10], but the treatments so far detected have been relatively aggressive, with half or more of the forest volume harvested.

The objective of the study was to investigate the possibilities of detecting changes of tree height using time series of phase height from InSAR data, and to assess the utility of applying an InSAR elevation bias correction for the

purpose. The change studies included detection and mapping of thinnings and clear-cuts. The research was based on data from the advanced SAR mission TanDEM-X and evaluated against reference data in the form of inventoried 40 m radius field plots and forest management records detailing performed treatments at the hemi-boreal test site of Remningstorp in southern Sweden.

## 2. MATERIAL AND METHODS

### 2.1. Test site

The study was conducted at the hemi-boreal test site Remningstorp in southern Sweden (Lat. 58°30' N, Long. 13°40' E). The site covers about 1,200 ha of productive forest. The dominant tree species are Norway spruce (*Picea abies* (L.) H. Karst.), Scots pine (*Pinus sylvestris* L.), and birch (*Betula* spp.). The soil type is mainly till (i.e., a mixture of glacial debris) with a field layer consisting of different herbs, blueberry (*Vaccinium myrtillus* L.) and narrow leaved grass (e.g., *Deschampsia flexuosa* (L.) Trin.). In denser old spruce stands the field layer is absent. The ground elevation varies moderately between 120 m and 145 m above sea level. The Remningstorp estate is managed by the Forestry Society's Estate Management Company (Skogssällskapet). A more exhaustive description of the property are presented in [11].

### 2.2. Field data

Circular field plots with 40 m radius were subjectively distributed within the test site. The plots were situated well inside homogenous stands, representing a range of tree species, stand ages and stem volumes. For most of the plots, every tree was calipered and positioned, while some plots, containing dense young forest, were instead sampled using 12 to 16 circular plots of 5 m to 7 m radius allocated in a systematic grid inside the 40 m plots. Allometric functions valid for the region were then used to estimate stem volume and AGB [12]. Plots were inventoried in three different years. In the fall of 2011, 25 plots were inventoried, and during the fall of 2012 and spring of 2013 a different set of 20 plots were inventoried. In the fall of 2014 the plots previously inventoried were revisited unless they had been clear-cut since the last inventory. Some additional field plots were also added in 2014, resulting in 27 inventoried plots in 2014.

In order to construct a data set of silvicultural treatments, a management plan containing detailed records on performed treatments on the forest holding was used. The treatment record was used to distribute the field plots into treatment types, and the field inventories were used to verify that the recorded treatments had actually been performed on approximately the recorded date. As some inventoried field plots were located outside the estate, they were not present in the treatment records, and were thus removed from the study. After the verification process, 34 plots in total were included in the study, 25 untreated, 5 thinned and 4 clear-cut. The stem volume decrease in the thinned plots, as determined from the

field measurements, ranged from 5% to 80%, while about 90% to 100% was harvested in the clear-cut plots, leaving only seed trees in some cases.

### 2.3. Remote sensing data

A time series of 24 TanDEM-X scenes acquired in bi-static configuration from 9 August 2011 to 4 June 2014 were used. The scenes were collected in strip map mode, all in VV polarization, from either single polarization scenes, or as a single channel from a dual polarization scene, with bandwidths of 100 MHz or 150 MHz, respectively. The height of ambiguity,  $h_a$ , ranged between 43 m and 100 m, but with the bulk of acquisitions obtained with a  $h_a$  between 50 m and 65 m. The incidence angles ranged from 19° to 40°.

### 2.4. InSAR processing

TanDEM-X data were delivered in the Coregistered Single look Slant range Complex (CoSSC) format. A complex interferogram was computed with 5×5 spatial averaging in range and azimuth. The interferogram was flattened with respect to earth curvature, and Goldstein filtered [13]. The flattened phase was unwrapped and converted to the phase height by scaling with the wavenumber, and the interferometric coherence was estimated from the flattened interferogram, using a coherence window of 3×3 pixels. Finally, the scenes were interpolated to a ground resolution of 10 m by 10 m. The estimated coherence was then corrected for decreasing signal-to-noise ratio [14-16].

The canopy is subject to substantial penetration of the radar signal, and for boreal coniferous forests this leads to a downward elevation bias of measured canopy heights of 11-22 m [17]. In [18], a correction of this bias was proposed, which was successfully applied to TanDEM-X data over temperate forests [19]. The canopy height bias is given by

$$\Delta h = -\frac{h_a |\gamma|}{2\pi} \arctan(\sqrt{|\gamma|^{-2} - 1}), \quad (1)$$

where  $\gamma$  is the coherence. The InSAR phase heights in the time series were corrected for elevation bias by calculating  $\Delta h$  on the pixel level, and subtracting it from the height values. A thorough derivation of (1) is presented in [18]. As the bias correction assumes penetration into an infinite volume, it is not theoretically valid when the signal has significant ground contributions. While this may apply to some field plots with low canopy heights, the correction was applied to all plots.

### 2.5. InSAR height changes from silvicultural treatments

To measure the effect of silvicultural treatments on the InSAR phase heights, the arithmetic mean phase height over each plot was extracted from the TanDEM-X time series, and the difference in overall mean value of these mean phase heights before and after a recorded treatment was calculated. In order to use the untreated plots as a baseline, these were assigned false treatment dates. To minimize the effect of the non-uniform temporal distribution of the InSAR acquisitions,

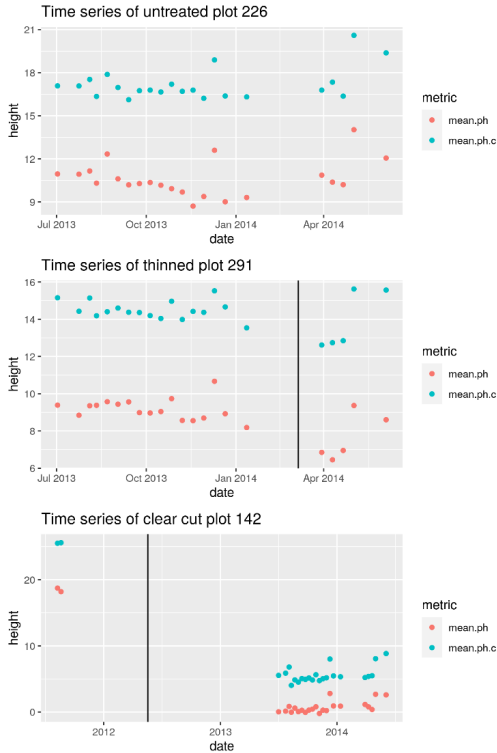


**Figure 1.** Time series of TanDEM-X phase heights (red) and height bias corrected TanDEM-X phase heights (cyan) for three treatment types. Treatment dates are indicated by vertical lines.

these were not placed randomly, or in the midpoint of the time series, but at the mean value of actual treatment dates for treated plots.

To assess the utility of the phase height bias correction, the calculations were made with and without application of the correction.

### 3. RESULTS, DISCUSSION AND CONCLUSIONS

While the height bias correction resulted in heights more closely resembling the actual tree heights in the data set, the results relating to detecting a change from silvicultural treatments were inconclusive. As the results in Figures 1 and 2, and Table 1 show, the average changes resulting from thinnings were on the order of meter, and clear-cuts expectedly resulted in much larger decreases. While there are group differences between the changes from untreated and thinned plots, the box-plots in Figure 2 reveals that they are hard to distinguish in individual

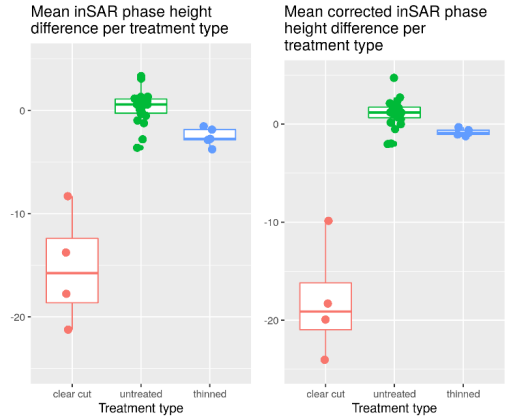


**Figure 2.** Box-plots of mean height difference per treatment type for both uncorrected and corrected TanDEM-X phase heights.

cases. However, given a sufficient density of data points both before and after a time point, the statistical significance of a measured height discontinuity could be used to quantify the uncertainty of a detected treatment. For time series spanning longer intervals it would be reasonable to account for possible growth in the forest by replacing the simple mean heights before and after a time-point by linear equations, and comparing the difference in the constant term, or if the time series was long enough to reflect the actual non-linear character of tree growth, tree height development curves could be fitted to the time series, and step-like deviations from a fitted model could similarly reflect silvicultural treatments or forest damage.

**Table 1.** Mean phase height change after treatment (m) with 'Untreated' included for baseline.

Metric	Untreated	Thinned	Clear-cut
Phase height	0.404896	-2.53911	-15.2584
Corrected phase height	1.233816	-0.8281	-18.0332

### ACKNOWLEDGEMENTS

The authors want to acknowledge The Foundation Skogssällskapet and the EU Interreg Botnia-Atlantica project KvarkenSpaceEco – New Space Digital Economy Innovation Center for funding the study and the Hildur and Sven Wingquist's foundation for funding the field data. We would also like to thank the German Aerospace Center (DLR) for providing the SAR data.

## REFERENCES

- [1] Persson, H., *Estimation of Forest Parameters Using 3D Satellite Data: Stereogrammetry, Radar-grammetry and Interferometry*, Ph.D. thesis, Swedish University of Agricultural Sciences, Umeå, Sweden, 2014.
- [2] Soja, M., *Modelling and Retrieval of Forest Parameters from Synthetic Aperture Radar Data*, Ph.D. thesis, Chalmers University of Technology, Göteborg, Sweden, 2014.
- [3] H.J. Persson, and J.E.S. Fransson, "Comparison between TanDEM-X- and ALS-based estimation of aboveground biomass and tree height in boreal forests," *Scandinavian Journal of Forest Research*, vol. 32, no. 4, pp. 306-319, 2017.
- [4] M. Santoro, O. Cartus, J.E.S. Fransson, and U. Wegmüller, "Complementarity of X-, C-, and L-band SAR backscatter observations to retrieve forest stem volume in boreal forest," *Remote Sensing*, vol. 11, no. 13, pp. 1-25, 2019.
- [5] J. Askne, P.B.G. Dammert, L.M.H. Ulander, and G. Smith, "C-band repeat-pass interferometric SAR observations of the forest," *IEEE Transactions on Geoscience and Remote Sensing*, vol. 35, pp. 25-35, 1997.
- [6] J.E.S. Fransson, and H. Israelsson, "Estimation of stem volume in boreal forests using ERS-1 C- and JERS-1 L-band SAR data," *International Journal of Remote Sensing*, vol. 20, no. 1, pp. 123-137, 1999.
- [7] I. Huuva, J.E.S. Fransson, H.J. Persson, J. Wallerman, L.M.H. Ulander, E. Blomberg, and M.J. Soja, "Measurements of forest biomass change using L- and P-band SAR backscatter. In *Proceedings of IGARSS 2017, International Cooperation for Global Awareness, Fort Worth, Texas, USA, 23-28 July, 2017*, pp. 5818-5821.
- [8] I. Huuva, H.J. Persson, M.J. Soja, J. Wallerman, L.M.H. Ulander, and J.E.S. Fransson, "Predictions of biomass change in a hemi-boreal forest based on multi-polarization L- and P-band SAR backscatter," *Canadian Journal of Remote Sensing*, vol. 46, no. 6, pp. 661-680, 2020.
- [9] M.J. Soja, H.J. Persson, and L.M.H. Ulander, "Mapping and modeling of boreal forest change in TanDEM-X data with the two-level model, In *Proceedings of IGARSS 2017, International Cooperation for Global Awareness, Fort Worth, Texas, USA, 23-28 July, 2017*, pp. 2887-2890.
- [10] M.J. Soja, H.J. Persson, and L.M.H. Ulander, "Modeling and detection of deforestation and forest growth in multitemporal TanDEM-X data," *IEEE Journal of Selected Topics in Applied Earth Observations and Remote Sensing*, vol. 11, no. 10, pp. 3548-3563, 2018.
- [11] Ahlberg, O., and L. Kardell, *Remningstorp: Från herresäte till skogslaboratorium*, Västergötlands Tryckeri AB, Skara, Sweden, 1997.
- [12] Marklund, L.G., *Biomassafunktioner för tall, gran och björk i Sverige*, Swedish University of Agricultural Sciences, Umeå, Sweden, 1988.
- [13] R.M. Goldstein, and C.L. Werner, "Radar interferogram filtering for geophysical applications," *Geophysical Research Letters*, vol. 25, 1998.
- [14] H. Chen, S.R. Cloude, and D.G. Goodenough, "Forest canopy height estimation using TanDEM-X coherence data," *IEEE Journal of Selected Topics in Applied Earth Observations and Remote Sensing*, vol. 9, no. 7, pp. 3177-3188, 2016.
- [15] F. Kugler, D. Schulze, I. Hajnsek, H. Pretzsch, and K. P. Papathanassiou, "TanDEM-X Pol-InSAR performance for forest height estimation," *IEEE Transactions on Geoscience and Remote Sensing*, vol. 52, no. 10, pp. 6404-6422, 2014.
- [16] H.J. Persson, H. Olsson, M.J. Soja, L.M.H. Ulander, and J.E.S. Fransson, "Experiences from large-scale forest mapping of Sweden using TanDEM-X data," *Remote Sensing*, vol. 9, pp. 1-26, 2017.
- [17] R.N. Treuhaft, S.N. Madsen, M. Moghaddam, and J.J. van Zyl, "Vegetation characteristics and underlying topography from interferometric radar," *Radio Science*, vol. 31, no. 6, pp. 1449-1485, 1996.
- [18] J. Dall, "InSAR elevation bias caused by penetration into uniform volumes," *IEEE Transactions on Geoscience and Remote Sensing*, vol. 45, no. 7, pp. 2319-2324, 2007.
- [19] M. Schlund, D. Baron, P. Magdon, and S. Erasmi, "Canopy penetration depth estimation with TanDEM-X and its compensation in temperate forests," *ISPRS Journal of Photogrammetry and Remote Sensing*, vol. 147, pp. 232-241, 2019.









Article

# Prediction of Site Index and Age Using Time Series of TanDEM-X Phase Heights

Ivan Huuva<sup>1,\*</sup>, Jörgen Wallerman<sup>1</sup> , Johan E. S. Fransson<sup>2</sup> and Henrik J. Persson<sup>1</sup>

<sup>1</sup> Department of Forest Resource Management, Swedish University of Agricultural Sciences, Skogsmarksgränd 17, SE-901 83 Umeå, Sweden; henrik.persson@slu.se (H.J.P.)

<sup>2</sup> Department of Forestry and Wood Technology, Linnaeus University, Georg Lückligns väg 1, SE-351 95 Växjö, Sweden

\* Correspondence: ivan.huuva@slu.se

**Abstract:** Site index and stand age are important variables in forestry. Site index describes the growing potential at a given location, expressed as the height that trees can attain at a given age under favorable growing conditions. It is traditionally used to classify forests in terms of future timber yield potential. Stand age is used for the planning of management activities such as thinning and harvest. SI has previously been predicted using remote sensing, but usually relying on either very short time series or repeated ALS acquisitions. In this study, site index and forest stand age were predicted from time series of interferometric TanDEM-X data spanning seven growth seasons in a hemi-boreal forest in Remningstorp, a test site located in southern Sweden. The goal of the study was to see how satellite-based radar time series could be used to estimate site index and stand age. Compared to previous studies, we used a longer time series and applied a penetration depth correction to the phase heights, thereby avoiding the need for calibration using ancillary field or ALS data. The time series consisted of 30 TanDEM-X strip map scenes acquired between 2011 and 2018. Established height development curves were fitted to the time series of TanDEM-X-based top heights. This enabled simultaneous estimation of both age and site index on 91 field plots with a 10 m radius. The RMSE of predicted SI and age were 6.9 m and 38 years for untreated plots when both SI and age were predicted. When predicting SI and the age was known, the RMSE of the predicted SI was 4.0 m. No significant prediction bias was observed for untreated plots, while underestimation of SI and overestimation of age increased with the intensity of treatment.

**Keywords:** site index; time series; InSAR; height development curves; growth measurement; forestry; TanDEM-X



**Citation:** Huuva, I.; Wallerman, J.; Fransson, J.E.S.; Persson, H.J. Prediction of Site Index and Age Using Time Series of TanDEM-X Phase Heights. *Remote Sens.* **2023**, *15*, 4195. <https://doi.org/10.3390/rs15174195>

Academic Editor: Lars T. Waser

Received: 28 June 2023

Revised: 17 August 2023

Accepted: 18 August 2023

Published: 25 August 2023



**Copyright:** © 2023 by the authors. Licensee MDPI, Basel, Switzerland. This article is an open access article distributed under the terms and conditions of the Creative Commons Attribution (CC BY) license (<https://creativecommons.org/licenses/by/4.0/>).

## 1. Introduction

In forests, wood productivity is of interest in commercial forestry to determine economic value and to support the planning of silvicultural treatments. Mapping of forest productivity and age can also be useful in monitoring and modeling forest biomass (carbon stock) and changes in this over time. Forest productivity can be expressed in terms of site index (SI), a variable expressing the expected height of dominant trees at a reference age, given the local conditions. In addition to being a useful tool in economic assessments, forecasting, and planning in the commercial management of forests, large-scale mapping of SI can be used to quantify the effects of environmental changes, such as mean temperature changes or droughts, on the productivity of forests [1]. Such mappings can be used to make predictions about the geographically distinct consequences of climate change.

SI can be determined based on climatic and field conditions such as precipitation, temperature, and classification of soil strata, which is useful when no trees are present on the site. Another way to estimate SI uses age and dominant- or top-height measurements and is generally favored over the previous method due to its practicality, low cost, and higher accuracy. It requires the location to have an established even-aged forest and relies

on a strong correlation between volume growth and height growth [2]. The definitions of top height vary, where some are based on the mean height of dominant trees, and others on the maximum tree height, or the mean height of a certain percentage of the highest trees in an area. In Sweden, the SI estimated from top height describes the site productivity for the dominant species in terms of the achievable height in meters of the largest diameter trees at a specific reference age ( $A_{SI}$ ). The top height is defined as the mean height of the 100 trees with the largest diameter at breast height per hectare. This definition of top height is sometimes called H100, and is meant to represent the upper height of tree crowns in the forest. Top height has successfully been estimated using different remote sensors. Examples include estimating top height with the maximum airborne laser scanning (ALS) canopy model height in a 10 m × 10 m window, or the maximum height in 500 m<sup>2</sup> plots of an aerial stereo-image-based canopy height model (CHM) [3,4].

While SI is not the most commonly estimated forest variable, it has been successfully predicted, often together with the related variable stand age, using a few different approaches, sensors, and sensor combinations. Commonly stand or tree heights are estimated by some remote sensing techniques and compared to known height–age curves to determine SI and age [5–11]. Véga and Onge [5] used CHMs based on historical aerial photographs and ALS from four time points spanning a period of 58 years to predict SI and age. Their models were estimated by minimizing mean absolute residuals to age–height curves, where the heights were extracted from CHMs calibrated with individual tree growth reconstruction. This method required counting tree rings on the cross-sections of felled trees to derive correction equations between tree heights from manual CMH interpretation and the field reconstructed heights. The procedure resulted in 2.4 m RMSE for SI and seven years RMSE for age predictions on 400 m<sup>2</sup> plots. Kandare et al. [6] used an individual tree crown (ITC) approach for predicting SI in boreal forests using airborne laser scanning (ALS) and hyperspectral data. They estimated the age, height, and diameter at breast height of the dominant trees from ALS and hyperspectral metrics. These were then used in age–height curves to predict SI. When predicting both SI and age, the method by Kandare et al. achieved RMSEs of 4.3 m and 34 years, respectively. When the age from field data was used in the prediction, the RMSE of SI predictions dropped to 1.18 m [6]. Solberg et al. used age-independent equations of top height growth and single tree ALS data to predict SI by matching single dominant trees in repeated ALS measurements six years apart [7]. They estimated SI values very close to field-based values for individual sample trees (bias 0.27 m, RMSE about 2.8 m, as interpreted from a figure). Penner et al. [8] used two successive ALS collections, acquired 13 years apart, to estimate SI with an RMSE of 2.5 m and a bias of 0.3 m on 400 m<sup>2</sup> field plots.

Many of the reported results are good but require access to long time series, as in the case of [5], rely on relatively costly ALS data, usually from several years, or on local calibration of remote sensing data or predicted attributes. Synthetic Aperture Radar (SAR) provides a cost-efficient alternative to ALS and aerial photography that is independent of sunlight and relatively unhindered by clouds and precipitation, thereby providing reliable year-round coverage of large parts of the world from different spaceborne systems. These operate in different parts of the microwave spectrum, called bands, corresponding to different wavelengths. Shorter wavelengths, such as the X and C bands, have significant contributions from the top part of the canopy and are, therefore, well suited for canopy height estimation using single-pass SAR interferometry (InSAR). Sentinel-1, a C band SAR system that provides open access data over large parts of the world, does, however, not have single-pass capability. TanDEM-X (TerraSAR-X add-on for Digital Elevation Measurement) is a two-satellite constellation that captures single-pass interferometric InSAR images at X-band (wavelength 3.1 cm). It provides data over a large part of the world and has proven itself valuable in forest variable retrieval [12,13]. Several studies have used TanDEM-X for the retrieval of forest variables [3,14–17]. Many of these have estimated forest heights from TanDEM-X data [3,14,17–21], and a few have investigated

height development due to deforestation, silvicultural treatments, or growth [22–24], or used phase height development to estimate biomass and volume changes [25–27].

The use of TanDEM-X data for SI prediction has so far been limited to Persson and Fransson [9], Wallerman et al. [10], and Persson and Fransson [11]. In these studies, simple linear models relating TanDEM-X phase heights to ALS percentiles or Lorey's heights (i.e., basal area weighted mean heights) from field data were used as calibration. Wallerman et al. [10] estimated SI when the age was provided, with an RMSE of 18.6% (corresponding to around 6–7 m, as interpreted from a figure) on 314 m<sup>2</sup> plots. They used TanDEM-X image pairs from three growth seasons calibrated using ALS data. Persson and Fransson [11] used four TanDEM-X acquisitions covering three growth seasons, calibrated using ALS data or Lorey's height from field data. They predicted SI with 4.4 m RMSE and age with 17.8 years RMSE on 0.5 ha plots. The need for calibration, however, hampers the scalability of the methods, as it relies on local high-resolution ALS data or field data. Furthermore, the usefulness of calibration data decreases with the time between data collection and the TanDEM-X acquisition date due to forest growth and other changes. Because of this, longer time series may often need calibration data from multiple time points.

In this study, we wanted to use a longer and denser time series of TanDEM-X acquisitions than in the previous studies and simultaneously avoid the use of calibration of the TanDEM-based heights via ancillary remote sensing or field data. Additionally, all remote sensing studies predicting SI that we are aware of use only plots, which appear to be unaffected by silvicultural treatments during the observation period. This study included plots subject to different silvicultural treatments during the study period to assess the potential effects on the predictions.

The remainder of the paper is structured as follows: Section 2 starts with a description of the test site and field data, after which the TanDEM-X data and its processing into TanDEM-X-based top heights are detailed. After this, established height development curves (HDC) and how they are used to calculate SI from field-measured top height and age are described. This is followed by a description of the method by which the SI and age are predicted by fitting an HDC to the time series of TanDEM-X-based top heights and how the results were evaluated. Section 3 presents the results of SI and age predictions. Section 4 contains a discussion of the results, and finally, Section 5 concludes the paper.

## 2. Materials and Methods

### 2.1. Test Site and Field Data

The study was conducted in Remningstorp, a forest test site located in southern Sweden (Lat. 58°30'N, Long. 13°40'E), consisting of about 1200 ha of commercially managed hemi-boreal forest. About two-thirds of the forest grows on till, a mixture of glacial debris, with, except in old spruce stands, a field layer of herbs, blueberry (*Vaccinium myrtillus* L.), and narrow-leaf grass (e.g., *Deschampsia flexuosa* (L.) Trin.). The main tree species are Norway spruce (*Picea abies* (L.) H. Karst.), Scots pine (*Pinus sylvestris* L.), and birch (*Betula* spp.). The rest of the forest grows on peatland, dominated by Scots pine. The landscape is mainly flat, with mild slopes, located 120 m to 145 m above sea level.

SI was determined for 91 circular field plots with a 10 m radius in a survey carried out in the fall of 2021. The age and height of two dominant trees per plot were measured, and the dominant species recorded. SI was calculated from the mean age and height for each plot. Using forest treatment records and inspection of biannual aerial orthophotos, the plots were classified into 2 clear-cut plots, 45 thinned plots, 7 pre-commercially thinned plots, and 26 untreated plots. Among the 91 plots, 11 plots were not covered by the available treatment records nor determined clear-cut in the inspection of orthophotos and, therefore, referred to as “undocumented”. While clear-cuts were evident in the available orthophotos, thinnings were difficult to detect, and it is likely that a significant portion of these undocumented plots were, in fact, thinned or pre-commercially thinned. Table 1. shows the mean and range of SI and the field-measured variables for each treatment group.

**Table 1.** Summary statistics on the 10 m radius field plots used in the study.

Treatment	Top Height [m]	Age [Years]	SI	n
	Min/Mean/Max	Min/Mean/Max	Min/Mean/Max	
Untreated	14/25/32	25/52/140	13/34/45	26
Pre-commercially thinned	14/20/28	15/25/50	27/35/44	7
Thinned	12/21/32	20/35/105	16/38/50	45
Clear-cut	25/26/28	60/70/80	30/30/30	2
Undocumented	15/24/29	25/49/96	16/34/40	11

SI values based on a previous field survey in 2014 were also available for 51 of the plots. Since the inherent productive potential of a specific site is not expected to change significantly in seven years, this dataset provided a means to characterize the uncertainty in the reference data. For these 51 plots, the variation in terms of Root Mean Square Deviation (RMSD) and bias, calculated according to Equations (1) and (2), between the 2021 and 2014 surveys of SI was 3.3 m and 2.0 m, respectively.

$$RMSD = \sqrt{\frac{\sum_{i=1}^N (SI_i^{2021} - SI_i^{2014})^2}{N}} \quad (1)$$

$$bias = \frac{\sum_{i=1}^N (SI_i^{2021} - SI_i^{2014})}{N} \quad (2)$$

## 2.2. SAR Data

Thirty TanDEM-X scenes were acquired in a bi-static configuration over Remningstorp between 11 August 2013 and 24 September 2018. The scenes were acquired in strip-map mode and included a vertical transmit/receive (VV) polarization, acquired either as a single polarization or as a single channel from a dual-polarization scene. The bandwidths were 100 MHz or 150 MHz, respectively. A single polarization was chosen to avoid polarization-dependent systematic differences in phase heights, and the VV polarization specifically was chosen because it provided the best temporal coverage of the time period under study. Furthermore, using meteorological records, only acquisitions from dates preceded by a three-day average temperature of above 5 °C were included since freezing temperatures severely affect the observed radar phase heights from vegetation. The height of ambiguity, *HoA*, ranged between 43 m and 100 m, but most scenes were acquired with a *HoA* between 50 m and 65 m. The incidence angles ranged from 19° to 40°.

The data were delivered in the Coregistered Single look Slant range Complex (CoSSC) format. A complex interferogram was computed with  $5 \times 5$  spatial averaging in range and azimuth. The interferogram was flattened with respect to earth curvature, and Goldstein filtered [28]. The flattened phase was unwrapped and converted to phase height by scaling with the wavenumber, and the interferometric coherence was estimated from the flattened interferogram using a coherence window of  $3 \times 3$  pixels. Finally, the scenes were interpolated to a ground resolution of 10 m  $\times$  10 m. The estimated coherence was corrected for decreasing signal-to-noise ratio [3,15,17].

The radar signal penetrates significantly into the canopy, and for boreal coniferous forests, this leads to a negative elevation bias of the canopy heights that can sometimes be as large as 10–20 m [3]. In [29], a correction of this bias was proposed, which has successfully been evaluated on TanDEM-X data over temperate and hemi-boreal forests [24, 30]. According to [29], the canopy height bias is given by

$$\Delta h = \frac{|HoA|}{2\pi} \tan^{-1} \left( \sqrt{|\gamma|^{-2} - 1} \right), \quad (3)$$

where  $\gamma$  is the volume coherence, and  $HoA$  is the height of ambiguity. The InSAR phase center heights in the time series were corrected for elevation bias by calculating  $\Delta h$  on pixel level and correcting the height values to produce InSAR-based canopy heights. A thorough derivation of (3) is given in [29]. As the bias correction assumes penetration into an infinite volume, it is not theoretically valid when the signal has significant ground contributions, and as a rule of thumb, the canopy height should be at least twice the bias correction. The correction was applied to all plots, although some field plots with low canopy heights or sparse forests could potentially violate this criterion. The ground contributions to the pixels with the highest phase heights on each plot are generally assumed to be small, and as described in Section 2.3, only the highest InSAR canopy heights on each plot influence the estimated top height in the method applied. However, ground contributions are likely dominant in clear-cut plots after treatment, but these were nevertheless corrected using Equation (3).

Each acquisition was assigned an integer representing its growth period based on the date of acquisition. A growth period was defined to start on 15 June, approximating the halfway point of the actual growth period, and last for one year. The earliest acquisition date was assigned to growth period 0, and the latest acquisitions were assigned to growth period 5.

### 2.3. Top Height Estimation

For each date, the corrected phase height values of pixels covered or intersected by a polygon defining the field plot region were extracted. In order to estimate the top height from these pixels, the 90th height percentile was calculated for each plot and date. Different percentiles were investigated, and generally, the higher percentiles correlated better with field-measured top heights. The 90th height percentile will hereafter be referred to simply as TanDEM-X top height.

### 2.4. Site Index

Established HDCs for common Swedish tree species, as developed in [31,32] and summarized in [33], describe the expected top height  $H_2$  at stand age  $A_2$ , given a measured top height  $H_1$  at stand age  $A_1$ :

$$H_2(H_1, A_1, A_2) = \frac{H_1 + d + r(H_1, A_1)}{2 + \frac{4\beta A_2^{b_2}}{H_1 - d + r(H_1, A_1)}}, \quad (4)$$

$$r(H_1, A_1) = \sqrt{(H_1 - d)^2 + 4\beta H_1 A_1^{b_2}}, \quad (5)$$

$$d = \beta A_{SI}^{b_2}, \quad (6)$$

where  $\beta$  and  $b_2$  are previously determined tree species-specific fixed parameters, and  $A_{SI}$  is the reference age. Equation (4) is commonly used to calculate SI given field measurements of top height and age, as was done with the field data in this study. By setting  $A_2$  to the preferred SI reference age and  $H_1$  and  $A_1$  to the measured height and age,  $H_2$  equals the SI. The HDCs were developed from multiple measurements on sets of field plots in even-aged forests, the predominant forest type in Sweden, and are therefore valid in such forests.

If  $H_1$  is set to a specific SI value instead of a measured height and  $A_1$  is set to the corresponding reference age,  $H_2$  gives the expected top height at any age  $A_2$ . For illustration, the resulting HDCs of Norway spruce for a few values of SI are shown in Figure 1.

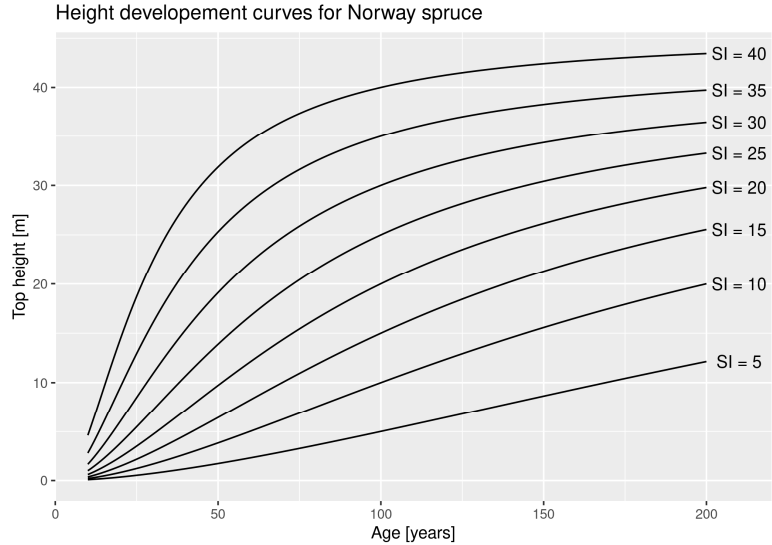


Figure 1. HDC describing the top height growth of Norway spruce.

2.5. Site Index Estimation

Setting  $H_1$  and  $A_1$  in Equation (4) to SI and the corresponding reference age, respectively, and substituting  $A_0 + GP$  (growth period) for  $A_1$ , allows us to express TanDEM-X top height  $H$  as a function of SI and  $GP$ , explicitly

$$H(A_0 + GP, SI) = \frac{SI + d + r(SI, A_{SI})}{2 + \frac{4\beta(A_0 + GP)^{\beta_2}}{SI - d + r(SI, A_{SI})}} \tag{7}$$

SI and  $A_0$  were determined by applying a weighted non-linear least squares regression of Equation (7) to the time series of TanDEM-X top heights, leaving initial age (age at the time of the first TanDEM-X measurement,  $A_0$ ) and/or SI as parameters. The function was fit to each field plot using dominant species information from the field data to select the correct fixed parameters, and two different prediction cases were applied; (a) estimates of both SI and  $A_0$  for each plot, and (b) estimates of only SI, assuming that the initial age is known. In case (b),  $A_0$  in the fitting was supplied from the field data. Figure 2 illustrates prediction case (a). In this figure, the process of fitting  $A_0$ , can be considered as a translation in time of the time series of TanDEM-X top heights to find the optimal fit, while the fitting of SI corresponds to the choice of optimal curve out of the family defined by Equation (7).

The least squares regression was performed using the *nls* function from the *stats* package of the open-source R programming language [34]. By using the *port* algorithm, the solver utilized an implementation of the *nl2sol* algorithm [35]. The SI and  $A_0$  (in prediction case (a)) were initialized to 25 and 75 and constrained to the intervals [4, 60] and [4, 200], respectively. This algorithm was chosen because of the possibility of setting bounds for the parameters. Otherwise, the algorithm tended to diverge or produce implausible parameter values for plots where TanDEM-X phase heights decreased over time. In case the fitting did not converge, it was restarted and initialized using the parameter values obtained in the non-converging fit.

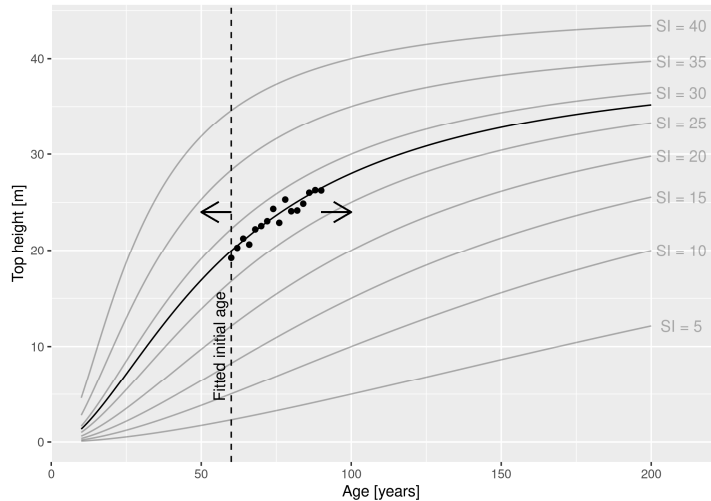


**Figure 2.** An illustration of the prediction of initial age  $A_0$  and SI by fitting a HDC to a time series of TanDEM-X top heights. The fitting of  $A_0$ , indicated by a dashed line in the figure, can be thought of as horizontal translation of the time series of data points, while the fitting of SI corresponds to the choice of curve.

The uncertainty of the InSAR phase height is, up to a critical value, roughly inversely proportional to the interferometric baseline [36] and hence proportional to  $HoA$ . Because of this, scenes with a baseline below, or equally an  $HoA$  above, some threshold value are often omitted in pursuit of high precision. In order to account for the  $HoA$ -related uncertainty without sacrificing temporal resolution, each observation was weighted in the fitting procedure with the reciprocal of  $HoA$ .

The SI and  $A_0$  predicted by parameter estimation were visually inspected via plots of the fitted HDC alongside the TanDEM-X top heights and the HDC expected from the field-data-based SI and age. The quality of predictions of  $A_0$  and SI were evaluated by comparisons with the corresponding field-data-based values, and prediction results were further visually evaluated through plots to investigate possible correlations between prediction errors and SI, stand age, species, or treatment groups. The Root Mean Square Error (RMSE) and bias were calculated for each treatment group  $k$  as

$$RMSE_k = \sqrt{\frac{\sum_{i=1}^{i=n_k} (\hat{y}_i - y_i)^2}{n_k}}, \text{ and} \quad (8)$$

$$bias_k = \frac{\sum_{i=1}^{i=n_k} (\hat{y}_i - y_i)}{n_k}, \quad (9)$$

where  $\hat{y}_i$  is the  $i$ th prediction,  $y_i$  the corresponding field data value, and  $n_k$  is the number of field plots in group  $k$ . Additionally, the coefficient of determination between predictions and reference values was calculated.

### 3. Results

In both prediction cases, the HDC fitting resulted in convergent solutions for all 91 field plots. For the vast majority of plots, a convergent solution was computed from the first initialization, but for a handful of plots, a re-initialization was required, as described in Section 2.5.



### 3.1. Predicting Both SI and Stand Age

In prediction case (a), when predicting both SI and  $A_0$ , the RMSEs and biases (as defined in Equations (8) and (9)) tended to increase with the intensity (in terms of expected relative biomass reduction) of the treatment. Table 2 shows the evaluation results for this case. For the untreated plots, the predicted SI had an RMSE of 6.9 m. The RMSE of pre-commercially thinned plots was 9.5 m, increasing to 16.1 m for the thinned group. The clear-cut group, however, had a slightly lower RMSE of 13.2 m.

**Table 2.** Treatment-wise summary statistics of SI and age predictions from HDC fitting to time series of TanDEM-X phase heights. P-c thinned = Pre-commercially thinned.

Treatment	SI RMSE [m]	SI $R^2$	SI Bias [m]	Age RMSE [Years]	Age $R^2$	Age Bias [Years]	$n$
Untreated	6.9	0.46	−1.6	38	0.406	9.6	26
P-c thinned	9.5	0.24	−7.8	22	0.321	11.9	7
Thinned	16.1	0.06	−12.6	82	0.015	52.5	45
Clear-cut	13.2	-	−13.2	137	-	136.8	2

The coefficient of determination between predicted and reference SI was 0.46 for the untreated plots and decreased to 0.24 for the pre-commercially thinned plots. It was very low, 0.06, for the thinned plots.  $R^2$  of the clear-cut plots is not reported, as it yields no information with only two observations. A plot of the field measured vs. predicted SI is shown in Figure 3.

Similarly, the magnitude of the biases of predicted SI increased with the relative intensity of the treatment, from a bias of −1.6 m for the untreated group to −7.8 m for the pre-commercially thinned group, −12.6 m for the thinned group, and −13.2 m for the clear-cut group. However, only the biases for the thinned and pre-commercially thinned plots were significant at the 95% confidence level (Table 2 and Figure 4).

The predicted initial age  $A_0$  had an RMSE of 38 years for the untreated group, 22 years for the pre-commercially thinned group, and then increased with the intensity of treatment to 82 for the thinned group and 137 years for the clear-cut plots.

The  $R^2$  between predicted and reference age are similar to those for SI, 0.4 for untreated plots, and decreasing with treatment intensity. The  $R^2$  of the clear-cut plots is not reported, as it yields no information for only two observations.

The bias of predicted initial age increased in magnitude with the intensity of treatment, with a more intense treatment having a larger positive age prediction bias, going from 9.6 years for the untreated group to 137 years for the clear-cut plots. However, only the age prediction biases for thinned and clear-cut plots were significant at a 95% confidence level (Table 2 and Figure 5).

### 3.2. Predicting SI Assuming Known Age

In prediction case (b), when predicting only SI, using the field-measured age in the HDC fitting, the precision was better than for case (a), with RMSEs between 2.2 m and 5.3 m for all treatment groups. The biases were also smaller for every treatment, all between −2 m and 0.5 m (Table 3 and Figure 6). Moreover, none of the biases were statistically significant at a 95% confidence level. The coefficients of determination,  $R^2$ , between true and predicted SI were relatively high, with  $R^2$  values between 0.6 and 0.8. A plot of the field measured vs. predicted SI is shown in Figure 7.

An example of a time series of TanDEM-X top heights for an untreated plot superimposed with the fitted HDC and the reference-data-based HDC is shown in Figure 8. The size of a point representing TanDEM-X top height observation is proportional to its weight (reciprocal of  $HoA$ ) in the regression. In this example, the slope is slightly overestimated, leading to an overestimation of SI and an underestimation of stand age.

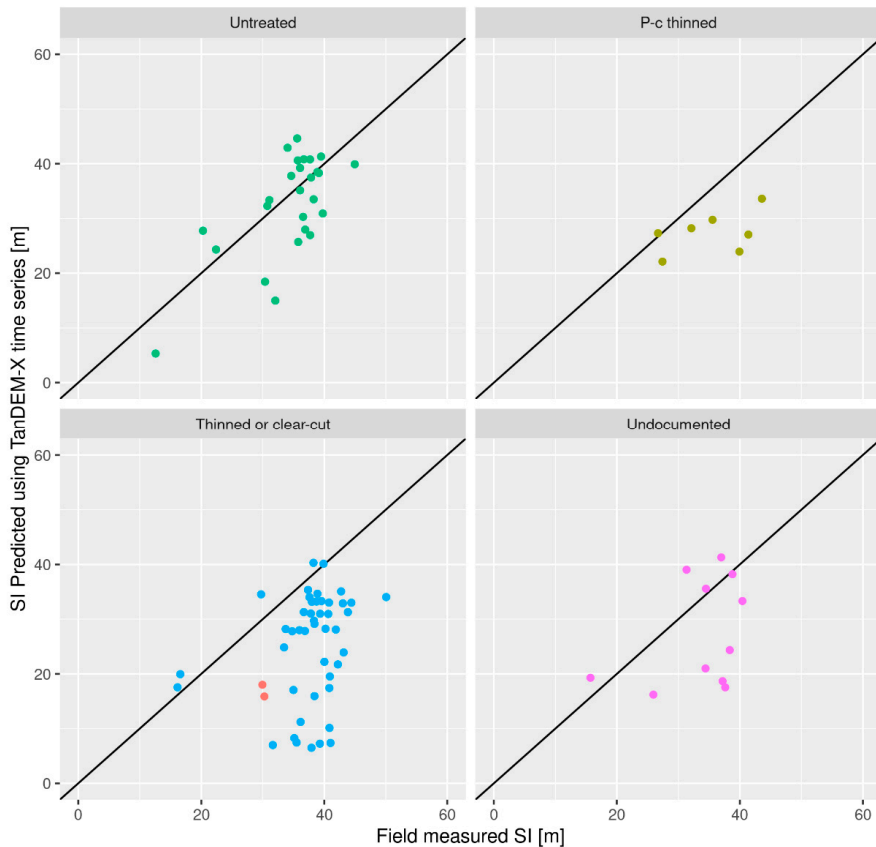


**Figure 3.** Plot of Predicted vs. field measured SI, obtained via simultaneous prediction of age. Colored by treatment. In the bottom left panel, thinned plots are shown in blue, while clear-cut plots are shown in red.

**Table 3.** Treatment-wise summary statistics of SI predictions assuming known age.

Treatment	SI RMSE [m]	SI R <sup>2</sup>	SI Bias [m]	<i>n</i>
Untreated	4.0	0.80	−0.8	26
P-c thinned	5.3	0.63	−1.21	7
Thinned	3.3	0.73	0.47	45
Clear-cut	2.2	—	−1.99	2

### 3.3. Error Characteristics

A clear correlation between severe underestimations of SI and overestimations of age was observed, as can be deduced from Table 2, and is perhaps even more clear in Figure 9, which shows predicted vs. reference SI, colored by the age prediction error. For both prediction cases, plots of prediction errors against reference age (in case (a)), reference top height and averaged height residuals from HDC fits were inspected to identify additional correlations, but none were found.

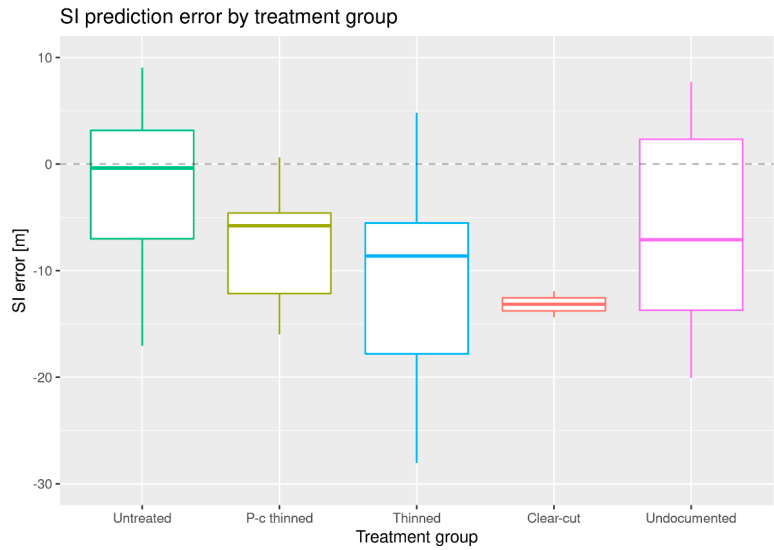


Figure 4. Box plot of SI prediction errors by group, obtained when simultaneously predicting age.

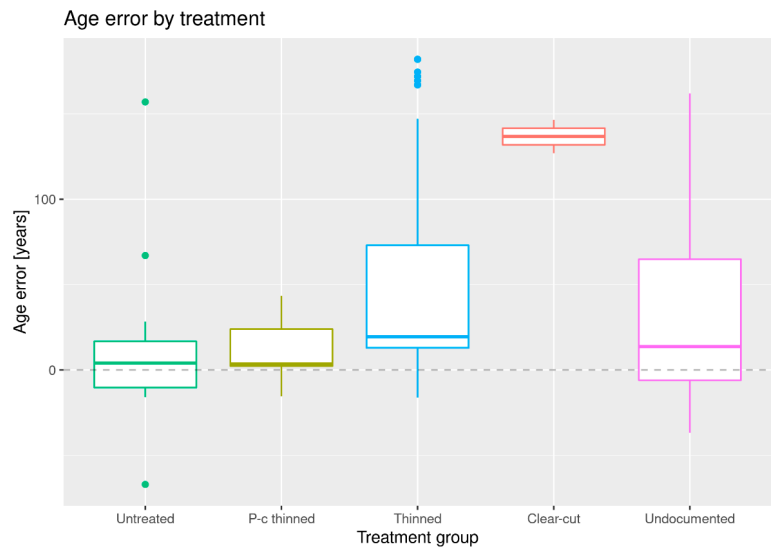
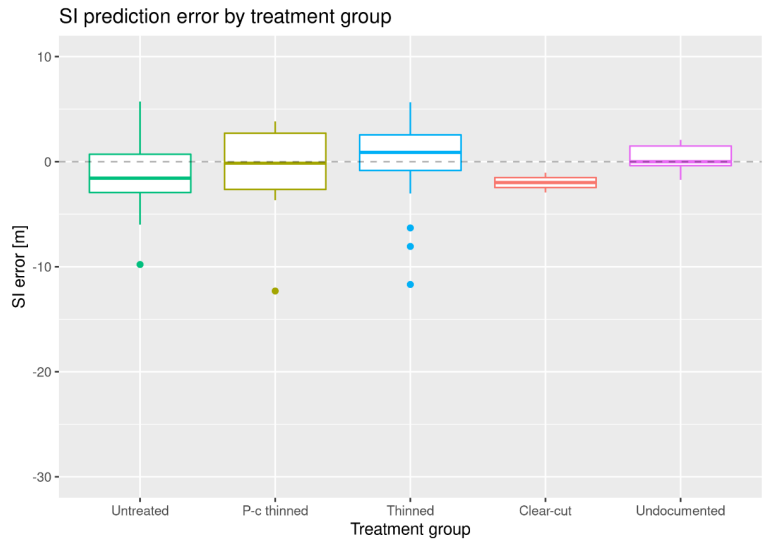
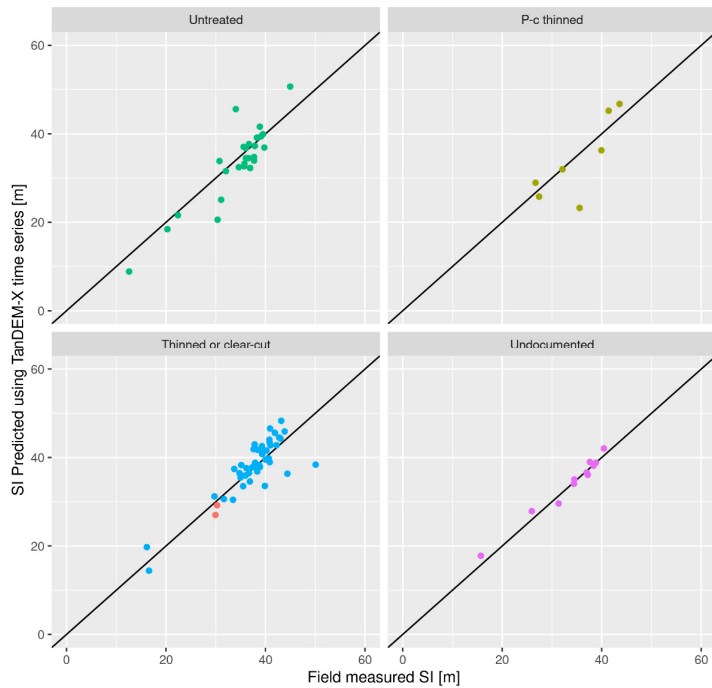


Figure 5. Box plot of age prediction errors by group, obtained when simultaneously predicting SI.



**Figure 6.** Box plot of SI prediction errors by group, obtained when simultaneously predicting age.



**Figure 7.** Predicted vs. field measured SI, using field measured ages in the fitting. Colored by treatment. In the bottom left panel, thinned plots are shown in blue, while clear-cut plots are shown in red.

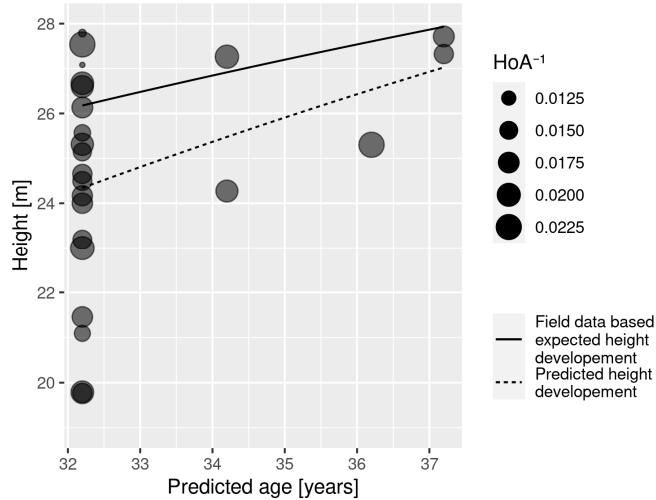


**Figure 8.** Time series untreated pine dominated plot 169. TanDEM-X top heights superimposed with predicted HDC and reference HDC. Predicted SI: 39.2, field SI: 36.1 predicted age: 32.2 field age: 43.

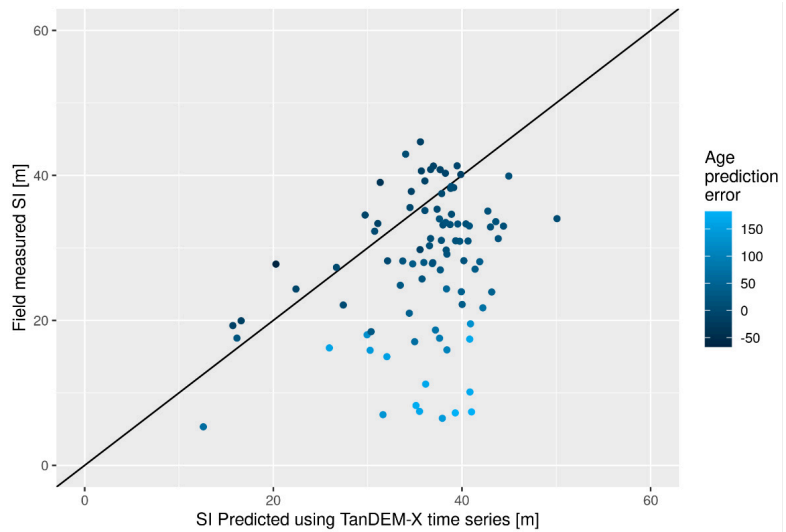


**Figure 9.** Predicted vs. field measured SI, colored by predicted age.

**4. Discussion**

The TanDEM-X top height, i.e., the 90th height percentile of bias-corrected phase heights, captured the canopy top height reasonably well. This was evidenced by (1) the relatively small and statistically insignificant prediction biases on untreated plots in case (a), when predicting both SI and age, and (2) the very low RMSE and bias of the predictions of SI in case (b), when age was provided from field data.

The RMSE of 4.0 m for prediction case (b) is significantly lower than the RMSE of 6–7 m in [10], which used ALS-calibrated TanDEM-X heights and similarly predicted only

SI on 10 m radius plots. In [10], the prediction of both SI and age using TanDEM-X data (corresponding to case (a) in this paper) was unsuccessful due to divergent solutions.

The RMSE for untreated plots in prediction case (a), 6.9 m, is larger than some previous studies [5,7–9,11], but they cannot be directly compared, as they differ in SI reference ages and/or the area of evaluation units. For example, this study used 10 m radius plots, while in [11], reporting 4.4 m and 17.8-year RMSEs, the plots were 16 times larger. In other studies, such as [5] (2.4 m RMSE) and [7] (about 2.8 m RMSE), the reported SI predictions differed in species and the reference age (50 years in [5], 40 years in [7]) at which the SI height is defined, due to local functions and practices.

Silvicultural treatments, from pre-commercial thinning to clear-cutting, lead to underestimation of the slope of the HDC, which in turn leads to underestimation of SI and overestimation of age. This tendency increased with the intensity of treatment.

We did not observe systematically larger prediction errors for mature stands, as observed in, for example, [5], where predictions based on measurement periods capturing later stand development stages with lower height growth rates produced more uncertain estimates of both SI and age. As the growth rate decreases with age, the importance of absolute height estimates increases (Figure 2). The absence of increased prediction uncertainty for older untreated plots further indicates that the absolute top height is estimated well by the TanDEM-X top height.

Some of the uncertainty in predictions is explained by edge effects. From inspection of orthophotos, we found that plots with large deviations between predictions and reference values were often located close to, or even across, stand boundaries or roads since the plot locations in the field surveys were distributed in a systematic grid. During the analyses, it was found that for such plots, the measured phase heights could be drastically different depending on look direction, which caused us to use only acquisitions from a descending orbit. This maximized the duration and resolution of the time series. Removal of such edge plots would likely have led to lower RMSEs in the predictions, but they were nevertheless kept in order to better reflect realistic results with a minimum amount of manual intervention. Because of this, it is also reasonable to expect higher precision for larger prediction units, where boundary effects have a smaller impact on the prediction or can be dealt with, for example, by using buffer zones.

Given the small prediction biases observed for untreated plots in case (a) and the apparent overall precision of top height estimates, we expect even longer time series to increase the quality of predictions of both SI and age significantly from the results for prediction case (a) in untreated plots. Longer time series may also mitigate the underestimation of slope resulting from treatments if the influence of such treatments on the TanDEM-X top height is transient in nature. Future studies should investigate the inclusion of multiple polarizations as a way to further increase usable observations.

Further, the prediction of SI and age via weighted non-linear regression readily accommodates the inclusion of other height data sources since top heights based on any source could simply be added to the time series and weighted according to the uncertainty of the source. Alternatively, since the SI prediction quality was shown to be much better assuming known age, the method could also be combined with other data sources by supplying age from field data or predictions from photogrammetric time series, as in [37]. In this study, the dominant species was assumed to be known, but in a practical application, the dominant species could also be predicted based on other data sources.

It should be noted that although the method proposed does not use any ancillary field data or remote sensing data such as ALS for calibration of the TanDEM-X data, it does require an accurate DTM in order to obtain reliable canopy heights from phase heights. This requirement is fulfilled in a rapidly increasing part of the world. Additionally, the HDCs used are developed using data from even-aged stands, and their applicability in other types of forest should be further investigated.

As the method presented does not rely on local calibration and easily accommodates and benefits from additional TanDEM-X scenes that extend or increase the temporal resolu-

tion of the prediction period, it is suited for producing wall-to-wall estimates over large areas of forest.

## 5. Conclusions

SI, the expected top height at some reference age, and stand age are important variables in forest management and forecasting. This study presented and evaluated a method of predicting SI and age using only time series of TanDEM-X data and a DTM.

The method consists of fitting established HDC to the time series, using the 90th height percentile of canopy penetration corrected phase heights as a surrogate for forest top heights. Predicted SI and age were retrieved as parameter values minimizing the squared top height residuals.

SI and age could be unbiasedly predicted for untreated plots, and the RMSE of predictions is likely to decrease with the length and temporal resolution of the time series available. When the stand age was known, the SI was predicted with an RMSE comparable to that of field-based measurements.

The results for treated plots indicate that the RMSE and bias of predictions increase with the intensity of silvicultural treatments, with a larger relative decrease in stem volume on average leading to a larger underestimation of SI and an overestimation of stand age and a higher RMSE for both variables.

In general, the results demonstrate viability for large-scale wall-to-wall mapping of SI using time series of TanDEM-X data without the need for ancillary data for height calibration. Further studies should investigate the use of multiple polarizations and both orbit directions to increase the length and temporal density of useful time series in an effort to further increase the obtained prediction quality.

**Author Contributions:** Conceptualization, J.E.S.F., I.H. and H.J.P.; methodology, I.H. and H.J.P.; software, I.H.; validation, I.H. and H.J.P.; formal analysis, I.H.; investigation, I.H.; resources, J.E.S.F. and H.J.P.; data curation, I.H., J.W. and H.J.P.; writing—original draft preparation, I.H.; writing—review and editing, I.H., J.W., H.J.P. and J.E.S.F.; visualization, I.H.; supervision, J.E.S.F., H.J.P. and J.W.; project administration, J.E.S.F. and H.J.P.; funding acquisition, J.E.S.F. and H.J.P. All authors have read and agreed to the published version of the manuscript.

**Funding:** This research was funded by the foundation Skogssällskapet, grant numbers 2021-923 and 2022-1023, the Bo Rydin Foundation for Scientific Research, grant number F 12/22, and Stiftelsen Seydlitz MP bolagen, grant number 143. The TanDEM-X images were acquired through the German Aerospace Center (DLR) “3D forest parameter retrieval from TANDEM-X interferometry” project [XTL\_VEGE0376]. The field data collection was funded by the Hildur and Sven Wingquist’s foundation.

**Data Availability Statement:** The data used in this study are available upon reasonable request.

**Conflicts of Interest:** The authors declare no conflict of interest.

## References

1. Roach, W.J.; Simard, S.W.; Defrenne, C.E.; Pickles, B.J.; Lavkulich, L.M.; Ryan, T.L. Tree Diversity, Site Index, and Carbon Storage Decrease With Aridity in Douglas-Fir Forests in Western Canada. *Front. For. Glob. Change* **2021**, *4*, 682076. [[CrossRef](#)]
2. Skovsgaard, J.P.; Vanclay, J.K. Forest Site Productivity: A Review of the Evolution of Dendrometric Concepts for Even-Aged Stands. *For. Int. J. For. Res.* **2008**, *81*, 13–31. [[CrossRef](#)]
3. Kugler, F.; Schulze, D.; Hajnsek, I.; Pretzsch, H.; Papatianassiou, K.P. TanDEM-X Pol-InSAR Performance for Forest Height Estimation. *IEEE Trans. Geosci. Remote Sens.* **2014**, *52*, 6404–6422. [[CrossRef](#)]
4. Stepper, C.; Straub, C.; Pretzsch, H. Assessing Height Changes in a Highly Structured Forest Using Regularly Acquired Aerial Image Data. *For. Int. J. For. Res.* **2015**, *88*, 304–316. [[CrossRef](#)]
5. Vêga, C.; St-Onge, B. Mapping Site Index and Age by Linking a Time Series of Canopy Height Models with Growth Curves. *For. Ecol. Manag.* **2009**, *257*, 951–959. [[CrossRef](#)]
6. Kandare, K.; Ørka, H.O.; Dalponte, M.; Næsset, E.; Gobakken, T. Individual Tree Crown Approach for Predicting Site Index in Boreal Forests Using Airborne Laser Scanning and Hyperspectral Data. *Int. J. Appl. Earth Obs. Geoinf.* **2017**, *60*, 72–82. [[CrossRef](#)]
7. Solberg, S.; Kvaalen, H.; Puliti, S. Age-Independent Site Index Mapping with Repeated Single-Tree Airborne Laser Scanning. *Scand. J. For. Res.* **2019**, *34*, 763–770. [[CrossRef](#)]

8. Penner, M.; Woods, M.; Bilyk, A. Assessing Site Productivity via Remote Sensing—Age-Independent Site Index Estimation in Even-Aged Forests. *Forests* **2023**, *14*, 1541. [[CrossRef](#)]
9. Persson, H.J.; Fransson, J.E.S. Analysis of Tree Height Growth with TanDEM-X Data. In Proceedings of the 35th EARSeL Symposium, Stockholm, Sweden, 15–19 June 2015; Volume 1, pp. 1–6.
10. Wallerman, J.; Nyström, K.; Bohlin, J.; Persson, H.J.; Soja, M.J.; Fransson, J.E.S. Estimating Forest Age and Site Productivity Using Time Series of 3D Remote Sensing Data. In Proceedings of the 2015 IEEE International Geoscience and Remote Sensing Symposium (IGARSS), Milan, Italy, 26–31 July 2015; pp. 3321–3324.
11. Persson, H.J.; Fransson, J.E.S. Estimating Site Index From Short-Term TanDEM-X Canopy Height Models. *IEEE J. Sel. Top. Appl. Earth Obs. Remote Sens.* **2016**, *9*, 3598–3606. [[CrossRef](#)]
12. Fiedler, H.; Krieger, G.; Zink, M.; Younis, M.; Bachmann, M.; Huber, S.; Hajnsek, I.; Moreira, A. The TanDEM-X Mission: An Overview. In Proceedings of the 2008 International Conference on Radar, Adelaide, Australia, 2–5 September 2008; pp. 60–64.
13. Krieger, G.; Zink, M.; Bachmann, M.; Bräutigam, B.; Schulze, D.; Martone, M.; Rizzoli, P.; Steinbrecher, U.; Walter Antony, J.; De Zan, F.; et al. TanDEM-X: A Radar Interferometer with Two Formation-Flying Satellites. *Acta Astronaut.* **2013**, *89*, 83–98. [[CrossRef](#)]
14. Karila, K.; Vastaranta, M.; Karjalainen, M.; Kaasalainen, S. Tandem-X Interferometry in the Prediction of Forest Inventory Attributes in Managed Boreal Forests. *Remote Sens. Environ.* **2015**, *159*, 259–268. [[CrossRef](#)]
15. Persson, H.J.; Olsson, H.; Soja, M.J.; Ulander, L.M.H.; Fransson, J.E.S. Experiences from Large-Scale Forest Mapping of Sweden Using TanDEM-X Data. *Remote Sens.* **2017**, *9*, 1253. [[CrossRef](#)]
16. Persson, H.J.; Fransson, J.E.S. Comparison between TanDEM-X- and ALS-Based Estimation of Aboveground Biomass and Tree Height in Boreal Forests. *Scand. J. For. Res.* **2017**, *32*, 306–319. [[CrossRef](#)]
17. Chen, H.; Cloude, S.R.; Goodenough, D.G. Forest Canopy Height Estimation Using Tandem-X Coherence Data. *IEEE J. Sel. Top. Appl. Earth Obs. Remote Sens.* **2016**, *9*, 3177–3188. [[CrossRef](#)]
18. Kugler, F.; Hajnsek, I. Forest Characterisation by Means of TerraSAR-X and TanDEM-X (Polarimetric and) Interferometric Data. In Proceedings of the 2011 IEEE International Geoscience and Remote Sensing Symposium, Vancouver, BC, Canada, 24–29 July 2011; pp. 2578–2581.
19. Olesk, A.; Praks, J.; Antropov, O.; Zalite, K.; Arumäe, T.; Voormansk, K. Interferometric SAR Coherence Models for Characterization of Hemiboreal Forests Using TanDEM-X Data. *Remote Sens.* **2016**, *8*, 700. [[CrossRef](#)]
20. Praks, J.; Antropov, O.; Hallikainen, M.T. LIDAR-Aided SAR Interferometry Studies in Boreal Forest: Scattering Phase Center and Extinction Coefficient at X- and L-Band. *IEEE Trans. Geosci. Remote Sens.* **2012**, *50*, 3831–3843. [[CrossRef](#)]
21. Schlund, M.; Magdon, P.; Eaton, B.; Aumann, C.; Erasmi, S. Canopy Height Estimation with TanDEM-X in Temperate and Boreal Forests. *Int. J. Appl. Earth Obs. Geoinf.* **2019**, *82*, 101904. [[CrossRef](#)]
22. Soja, M.J.; Persson, H.J.; Ulander, L.M.H. Modeling and Detection of Deforestation and Forest Growth in Multitemporal TanDEM-X Data. *IEEE J. Sel. Top. Appl. Earth Obs. Remote Sens.* **2018**, *11*, 3548–3563. [[CrossRef](#)]
23. Schlund, M.; Kukunda, C.B.; Baumann, S.; Wessel, B.; Kiefl, N.; von Poncet, F. Potential of Forest Monitoring with Multi-Temporal TANDEM-X Height Models. In Proceedings of the IGARSS 2020–2020 IEEE International Geoscience and Remote Sensing Symposium, Waikoloa, HI, USA, 26 September–2 October 2020; pp. 308–311.
24. Huuva, I.; Persson, H.J.; Wallerman, J.; Fransson, J.E.S. Detectability of Silvicultural Treatments in Time Series of Penetration Depth Corrected Tandem-X Phase Heights. In Proceedings of the IGARSS 2022–2022 IEEE International Geoscience and Remote Sensing Symposium, Kuala Lumpur, Malaysia, 17–22 July 2022; pp. 5909–5912.
25. Solberg, S.; May, J.; Bogren, W.; Breidenbach, J.; Torp, T.; Gizachew, B. Interferometric SAR DEMs for Forest Change in Uganda 2000–2012. *Remote Sens.* **2018**, *10*, 228. [[CrossRef](#)]
26. Solberg, S.; Næsset, E.; Gobakken, T.; Bollandsås, O.-M. Forest Biomass Change Estimated from Height Change in Interferometric SAR Height Models. *Carbon Balance Manag.* **2014**, *9*, 5. [[CrossRef](#)]
27. Askne, J.I.H.; Persson, H.J.; Ulander, L.M.H. Biomass Growth from Multi-Temporal TanDEM-X Interferometric Synthetic Aperture Radar Observations of a Boreal Forest Site. *Remote Sens.* **2018**, *10*, 603. [[CrossRef](#)]
28. Goldstein, R.M.; Werner, C.L. Radar Interferogram Filtering for Geophysical Applications. *Geophys. Res. Lett.* **1998**, *25*, 4035–4038. [[CrossRef](#)]
29. Dall, J. InSAR Elevation Bias Caused by Penetration Into Uniform Volumes. *IEEE Trans. Geosci. Remote Sens.* **2007**, *45*, 2319–2324. [[CrossRef](#)]
30. Schlund, M.; Baron, D.; Magdon, P.; Erasmi, S. Canopy Penetration Depth Estimation with TanDEM-X and Its Compensation in Temperate Forests. *ISPRS J. Photogramm. Remote Sens.* **2019**, *147*, 232–241. [[CrossRef](#)]
31. Elfving, B.; Kiviste, A. Construction of Site Index Equations for Pinus Sylvestris L. Using Permanent Plot Data in Sweden. *For. Ecol. Manag.* **1997**, *98*, 125–134. [[CrossRef](#)]
32. Eriksson, H.; Johansson, U.; Kiviste, A. A Site-index Model for Pure and Mixed Stands of Betula Pendula and Betula Pubescens in Sweden. *Scand. J. For. Res.* **1997**, *12*, 149–156. [[CrossRef](#)]
33. Johansson, U.; Ekö, P.M.; Elfving, B.; Johansson, T.; Nilsson, U. *Rön Från Sveriges Lantbruksuniversitet*; Swedish University of Agricultural Sciences: Uppsala, Sweden, 2014.
34. R Core Team. *R: A Language and Environment for Statistical Computing*; R Core Team: Vienna, Austria, 2013.



35. Dennis, J.E.; Gay, D.M.; Welsch, R.E. Algorithm 573: NL2SOL—An Adaptive Nonlinear Least-Squares Algorithm [E4]. *ACM Trans. Math. Softw.* **1981**, *7*, 369–383. [[CrossRef](#)]
36. Li, F.K.; Goldstein, R.M. Studies of Multibaseline Spaceborne Interferometric Synthetic Aperture Radars. *IEEE Trans. Geosci. Remote Sens.* **1990**, *28*, 88–97. [[CrossRef](#)]
37. Vastaranta, M.; Niemi, M.; Wulder, M.A.; White, J.C.; Nurminen, K.; Litkey, P.; Honkavaara, E.; Holopainen, M.; Hyypä, J. Forest Stand Age Classification Using Time Series of Photogrammetrically Derived Digital Surface Models. *Scand. J. For. Res.* **2016**, *31*, 194–205. [[CrossRef](#)]

**Disclaimer/Publisher’s Note:** The statements, opinions and data contained in all publications are solely those of the individual author(s) and contributor(s) and not of MDPI and/or the editor(s). MDPI and/or the editor(s) disclaim responsibility for any injury to people or property resulting from any ideas, methods, instructions or products referred to in the content.

ACTA UNIVERSITATIS AGRICULTURAE SUECIAE

DOCTORAL THESIS No. 2023:98

Synthetic Aperture Radar (SAR) is capable of observing forests independently of sunlight and weather conditions, thereby offering frequent and reliable coverage of forests. The thesis comprises five studies conducted at the Remningstorp test site in southern Sweden, showcasing the use of polarimetric SAR and interferometric SAR for predicting above-ground biomass (AGB) change, detecting silvicultural treatments, and estimating site index and stand age. Overall, the research underscores SAR's potential for generalizable forest variable change estimation methods.

**Ivan Huuva** received his doctoral education at the Department of Forest Resource Management, SLU, Umeå, and holds a MSc in engineering physics from Umeå University.

Acta Universitatis Agriculturae Sueciae presents doctoral theses from the Swedish University of Agricultural Sciences (SLU).

SLU generates knowledge for the sustainable use of biological natural resources. Research, education, extension, as well as environmental monitoring and assessment are used to achieve this goal.

ISSN 1652-6880

ISBN (print version) 978-91-8046-248-8

ISBN (electronic version) 978-91-8046-249-5